Delta dynamics: a numerical investigation of the inhibiting effects of tidal range and significant wave height on delta development

Thesis submitted to the University of Nottingham for the degree of

Doctor of Philosophy

Ewan Sloan

Student ID: 20311311

January 13, 2025

Abstract

In this thesis, the process-based numerical model Delft3D 4 (Deltares, 2021a,b) is used to investigate how tidal range and significant wave height affect, and potentially prevent, the development of river deltas within a range of idealised simulations. In order to reduce the parameter space and hence simplify analysis, focus is restricted to just the effects of wave height and tidal range, following the assumption that the effects of discharge are relatively linear and predictable—i.e. lower river sediment flux equates to reduced likelihood of delta formation. The primary objective of the work, therefore, is to determine if there exist limits of significant wave height and / or tidal range beyond which delta formation is prevented, and to elucidate the relevant processes where (if) this is found to be the case.

To this end, we investigate how delta development is affected under increasing values of wave height and tidal range, both independently and in combination, leading to the identification of four distinct regimes of delta formation. We then discuss the mechanisms by which delta formation is prevented in our simulations with the largest tidal ranges and wave heights, hence also identifying a fifth regime of delta-suppression. Each of these five regimes is qualitatively compared to representative real world examples of (non-)deltas, and the work is positioned against existing literature regarding the limits of delta formation and classification of deltas by process-dominance.

Finally, based upon the observation that waves and tides in combination act to functionally 'diffuse' sediments away from the mouths of rivers in the simulations, it is hypothesised that deltas do not form when such diffusion is of sufficient magnitude to prevent the formation of persistent deposits (and hence deltas) within the vicinity of river mouths. This hypothesis is tested via comparison to a 1D alongshore sediment diffusion formula with a source term representing river sediment discharge. This formula is found to match sediment distributions of the process-based simulations with increasing accuracy under the larger significant wave heights and tidal ranges modelled.

Acknowledgements

I would first and foremost like to thank my supervisors, Nicholas Dodd and Riccardo Briganti, for their advice, insight, and encouragement throughout the course of studying for my PhD. I am, I hope it is fair to say, both a better critical thinker and a better writer as a result of their help. The feedback, criticism, and encouragement of my internal examiner, David Hargreaves, has also helped to greatly improve the standard of this work. Thanks are also extended to Nicoletta Leonardi of the University of Liverpool for agreeing to be my external examiner, and for the engaging and insightful discussion of this work during my viva. Funding for my studies from the Envision Doctoral Training Partnership (grant reference NE/S007423/1) is also gratefully acknowledged. The opportunity to spend these past few years engaged in novel research has been a great privilege and a process of both personal and professional development; it is one which would have been impossible without this funding and support. The scale and number of simulations presented in this thesis would have been unachievable without access to the University of Nottingham's High Performance Computing (HPC) cluster, and the technical support of Colin Bannister in particular. My thanks are also extended to Anurak Sriariyawat of Chulalongkorn University Department of Water Resource Engineering for his contributions towards the earlier stages and considerations of this project. Finally, I would like to thank my partner, Ellen Woodhouse, for her support, particularly during the most difficult periods of the last four years. I probably could have done it without you, but I'm glad I didn't have to.

Contents

List of Figures

List of Tables

Nomenclature

α	Spectral energy density slope [-]
α_b	Wave breaking angle (shoreline diffusion equation) [rad]
$\bar{c}$	Depth-averaged sediment concentration [$\mathsf{L}^3\,\mathsf{L}^{-3}$]
$\bar{c}_{in}$	Suspended sediment concentration at inlet boundary [$\mathsf{L}^3\,\mathsf{T}^{-1}$]
$\bar{u}$	Depth-averaged Eulerian velocity in x-direction [$\mathsf{L}\,\mathsf{T}^{-1}$]
$\bar{v}$	Depth-averaged Eulerian velocity in y-direction [$\mathsf{L}\,\mathsf{T}^{-1}$]
$\bar{w}$	Cell centre velocity vector [$\mathsf{L}\,\mathsf{T}^{-1}$]
$\bar{W}_\ell$	Non-dimensionalised velocity in ℓth directional bin [-]
$\bar{w}_\ell$	Velocity in ℓth directional bin [$\mathsf{L}\,\mathsf{T}^{-1}$]
β_1	Shoreline slope (cross-shore beach and bar profile) [$\mathsf{L}\,\mathsf{L}^{-1}$]
β_2	Offshore slope (cross-shore beach and bar profile) [$\mathsf{L}\,\mathsf{L}^{-1}$]
χ	Non-dimensionalised excess mobility number [-]
χ_{inner}	Non-dimensionalised excess mobility number within low tide area [-]
Δt	Numerical time step [T]
Δx	Discrete grid spacing in x-direction [L]
Δx_r	Discrete grid spacing of river domain in x-direction [L]

Δy	Discrete grid spacing in y-direction [L]
Δy_r	Discrete grid spacing of river domain in y-direction [L]
Δz_b	Bed elevation change [L]
ϵ_H	Horizontal diffusion of sediment [L^{2} T^{-1}]
ϵ_H^{back}	Ambient background horizontal diffusion of sediment [L^{2} T^{-1}]
ϵ_H^{sgs}	Horizontal diffusion of sediment due to SGS turbulence [L^{2} T^{-1}]
γ	Factor relating to spectral energy density (SGS turbulence model) [-]
γ_0	JONSWAP peak enhancement factor [-]
γ_b	Depth induced wave breaking ratio [-]
κ	Von Kárman's constant [-]
κ_d	Coefficient of diffusion [L T^{-1}]
κ_{sde}	Diffusion coefficient (shoreline diffusion equation) [L^{2} T^{-1}]
ν	Kinematic viscosity of water [L^{2} T^{-1}]
ν_H	Horizontal eddy viscosity [L^{2} T^{-1}]
ν_H^{3D}	Horizontal component of turbulence resulting from shear dispersion (SGS turbulence model) [L^{2} T^{-1}]
ν_H^{back}	Background horizontal eddy viscosity [L^{2} T^{-1}]
ν_H^{sgs}	Horizontal eddy viscosity determined by SGS turbulence model [L^{2} T^{-1}]
ω	Wave radial frequency [rad T^{-1}]
ϕ	Opening angle [°]
ϕ_c	Critical opening angle [°]
π_Δ	Probability of delta formation [-]
ρ_0	Water density [M L^{-3}]

ρ_s	Sediment grain density [M L^{-3}]
ρ_{bulk}	Bulk density of bed sediments [M L^{-3}]
σ	Relative frequency of waves [T^{-1}]
σ_T	Turbulent Schmidt number [-]
σ_x	Standard deviation of alongshore sediment distribution [L]
τ	Relaxation time (SGS turbulence model) [T]
τ_e	Time-scale of largest eddies in simulation [T]
Θ	Dry cell erosion factor [-]
θ	Directional coordinate [deg]
Θ_{SD}	Maximum dry cell erosion factor [-]
ξ	Fraction of solids in sediment bed [-]
ζ	Mean free-surface elevation [L]
A	Area of delta plain [L^2]
a	Variable controlling relaxation rate of temporally filtered velocities (SGS turbulence model) [-]
a_1	Calibration constant (cross-shore beach and bar profile) [-]
A_b	"Amplitude" of offshore bar (cross-shore beach and bar profile) [L]
A_{wet}	Area of wet cells within delta plain [L^2]
B	River width [L]
B_d	Variable representing bed friction (SGS turbulence model) [-]
C	Chézy bed friction coefficient [L$^{1/2}$ T^{-1}]
c	Celerity of a surface disturbance [L T^{-1}]
c_σ	Wave action propagation velocity in frequency space [T^{-2}]

c_θ	Wave action propagation velocity in directional space [rad T^{-1}]
c_b	Bottom-friction drag coefficient (JONSWAP) [$\mathsf{L}^2\,\mathsf{T}^{-3}$]
C_D	Current-induced drag coefficient [-]
C_f	Courant-Friedrichs-Lewy stability number [-]
c_g	Wave group celerity [$\mathsf{L}\,\mathsf{T}^{-1}$]
c_x	Wave action propagation velocity in x-direction [$\mathsf{L}\,\mathsf{T}^{-1}$]
c_y	Wave action propagation velocity in y-direction [$\mathsf{L}\,\mathsf{T}^{-1}$]
c_{eq}	Equilibrium sediment concentration [$\mathsf{L}^3\,\mathsf{L}^{-3}$]
c_{mob}	Channel mobility [-]
c_{split}	Number of channel splits [-]
D	Deposition rate per unit area [$\mathsf{L}\,\mathsf{T}^{-1}$]
d_c	Depth of closure [L]
d_d	Beach dune height [L]
d_p	Profile depth [L]
$D_{*,\ell}$	Dimensionless grain diameter of ℓth sediment fraction [-]
$D_{50,\ell}$	Median grain diameter of ℓth sediment fraction [L]
E	Erosion rate per unit area [$\mathsf{L}\,\mathsf{T}^{-1}$]
f_m	Morphological acceleration factor [-]
f_z	A normalisation factor relating to bed level change [L]
f_{lp}	Spatial low-pass filter coefficient [-]
g	Gravitational acceleration [$\mathsf{L}\,\mathsf{T}^{-2}$]
h	Mean water depth [L]

H_s	Significant wave height [L]
H_t	Tidal range [L]
$H_{max,\Theta}$	Threshold depth below which DCEF Θ is reduced [L]
H_{sb}	Significant breaking wave height [L]
H_{sed}	Minimum depth for sediment transport calculations [L]
k	Wave number [L^{-1}]
k_s	Cut-off turbulent wave number (SGS turbulence model) [L^{-1}]
L_x	Alongshore width of domain [L]
L_y	Cross-shore width of domain [L]
m_b	Slope in wave breaking region [L L^{-1}]
M_x	Wave energy dissipation terms in x-direction [L T^{-2}]
M_y	Wave energy dissipation terms in y-direction [L T^{-2}]
N	Spectral action density [L^2 T^2 rad^{-1}]
n	Fraction of void-space in sediment bed [-]
n_D	Factor representing the number of spatial dimensions modelled [-]
P	Energy sinks (sources) related to dissipative (additive) processes [L^2 rad^{-1}]
p	Degree of flow-grid alignment [-]
Q_0	River discharge rate [L^3 T^{-1}]
Q_k	Alongshore sediment flux (shoreline diffusion equation) [L^3 T^{-1}]
q_s	Volumetric suspended sediment flux [L^3 T^{-1} L^{-1}]
Q_x	Total alongshore sediment flux [L^3 T^{-1}]
q_x	Sediment flux per metre width in x-direction (diffusion model) [L^3 T^{-1} L^{-1}]

q_y	Sediment flux per metre width in y-direction (diffusion model) [L^3 T^{-1} L^{-1}]
$q_{b,x}$	Bedload transport rate in x-direction [L^3 T^{-1} L^{-1}]
$q_{b,y}$	Bedload transport rate in y-direction [L^3 T^{-1} L^{-1}]
q_{bc}	Bedload flux due to current only [L^3 T^{-1} L^{-1}]
q_{bw}	Bedload flux due to waves only [L^3 T^{-1} L^{-1}]
Q_{sed}	River volumetric sediment discharge [L^3 T-1]
$q_{sw,x}$	Suspended sediment flux in x-direction due to wave asymmetry [L^3 T^{-1} L^{-1}]
$q_{sw,y}$	Suspended sediment flux in y-direction due to wave asymmetry [L^3 T^{-1} L^{-1}]
R^{+}_{D3D}	Riemann boundary condition value [L T^{-1}]
Re_B	River mouth Reynolds number [-]
S	Rate of change of suspended sediment concentration due to entrainment / deposition [L^3 L^{-3} T^{-1}]
s	Relative grain density [-]
S^*	Strain rate tensor [T^{-1}]
S_0	Stability number [-]
$S_{c,l}$	Critical stability number, lower [-]
$S_{c,u}$	Critical stability number, upper [-]
$S_{t,0}$	Strouhal number of the vortex-shedding jet [-]
T	Duration of simulation [T]
t	Time [T]
T_E	Time for one half-rotation of an eddy in a vortex-shedding jet [T]
T_p	Peak wave period [T]
T_s	Relaxation timescale by which $\bar{c}$ converges toward c_{eq} [T]

T_t	Tidal period [T]
U	Generalised Lagrangian mean (GLM) velocity in x-direction [L T^{-1}]
u^*	Fluctuating part of Eulerian velocity in x-direction (SGS turbulence model) [L T^{-1}]
u_*	Bed shear velocity [L T^{-1}]
u_0	Cross-section-averaged velocity at river mouth [L T^{-1}]
u_s	Stokes-drift velocity in x-direction [L T^{-1}]
u_{cr}	Critical bed shear velocity [L T^{-1}]
u_{rms}	Root mean square orbital wave velocity [L T^{-1}]
V	Generalised Lagrangian mean (GLM) velocity in y-direction [L T^{-1}]
v^*	Fluctuating part of Eulerian velocity in y-direction (SGS turbulence model) [L T^{-1}]
V_s	Volume of river-delivered sediment per metre alongshore [L]
v_s	Stokes-drift velocity in y-direction [L T^{-1}]
W	Width over which incoming sediment flux is distributed (diffusion model) [L]
W_b	Width of offshore bar (cross-shore beach and bar profile) [L]
x	(Alongshore) Cartesian coordinate [L]
X_b	Offshore location of bar crest (cross-shore beach and bar profile) [L]
y	(Cross-shore) Cartesian coordinate [L]
z	(Vertical) Cartesian coordinate [L]
z_b	Bed elevation [L]

Chapter 1

Introduction

1.1 Background and motivation

River deltas are fertile, low-lying coastal areas, which have long been settled and exploited by the human population. By one recent estimate, 339 million people live directly on deltas globally, often in large cities (Edmonds et al., 2020). It is unsurprising that deltas are so widely settled; they provide abundant freshwater, plentiful food resources from the sea, extensive regions of fertile soil for agriculture, and have acted as important transport hubs between river and sea throughout human history (Syvitski and Saito, 2007). However, due to their typically low overall elevations, deltas are subject to flooding due to both high rainfall upstream, and from storm surge in the basins in which they form (Edmonds et al., 2020). An estimated 89% of the total population living on deltas reside within latitudes subject to tropical cyclones. Furthermore, such regions are overwhelmingly located in developing countries, where resources required to mitigate flooding hazards may be lacking.

While deltas have clear importance, it is also notable that only an estimated 40% of global rivers in fact form deltas (Caldwell et al., 2019). This clearly implies that formation of a delta is not a certainty for any given river, even when that river delivers sediment to the coast. By extension, we might expect that any future changes to the conditions for existing river and coast systems might result in the loss or gain of deltaic land, highlighting a clear need for understanding of the conditions which inhibit or facilitate delta development.

Most rivers have been subjected to human interference through both river management (e.g. dam construction) and land use change (e.g. deforestation for agriculture), leading to changes in patterns of sediment transport and river discharge with repercussions for delta formation (Syvitski et al., 2005; Saito et al., 2007; Nienhuis et al., 2020; Syvitski et al., 2022b). Such interference can either increase or decrease sediment discharges. Water management—typically the impounding of water (and sediment) within dams, but also the diversion of water for agriculture—tends to reduce sediment fluxes, leading to "sediment starvation" within downstream depositional regions. An estimated 970 deltas globally have seen their sediment discharges reduced by $> 50\%$ relative to their discharges prior to human interference (Nienhuis et al., 2020). Such reductions are partially due to the noted impoundment of sediments behind dams. However, they are also a consequence of the attenuation of water discharge due to controlled release of water from dams; as sediment fluxes are typically exponentially proportional to water discharges, the attenuation of peaks in water discharge due to water management can greatly reduce net sediment transport in a river (see e.g. case studies on the Mekong Duy Vinh et al., 2016; Thanh et al., 2017). By contrast, deforestation for (typically) agriculture leads to increased soil erosion and hence increased sediment fluxes in rivers. Syvitski et al. (2022b) estimate that global net sediment discharge in rivers reduced from 15.7 $\mathrm{Gt\,yr^{-1}}$ in 1950, down to 8.5 $\mathrm{Gt\,yr^{-1}}$ by 2010—a net reduction of around 46%. However, the net reduction figure alone does not capture the magnitude of *increases* to sediment flux; Syvitski et al. (2022b) further note that during the same period, while impoundment of sediment behind dams has increased from 2.8 $\mathrm{Gt\,yr^{-1}}$ to 65 $\mathrm{Gt\,yr^{-1}}$, sediment flux due to soil erosion in fact rose from 25 $\mathrm{Gt\,yr^{-1}}$ to 75 $\mathrm{Gt\,yr^{-1}}$. Further changes of similar magnitude are noted in a wide range of areas including, for example, dredging and construction. This highlights that while sources of sediment starvation are substantial, increases to sediment flux—while comparatively smaller—are also significant.

One further aspect of human activity affecting deltas is worth noting; that of land subsidence—sometimes referred to as relative sea level rise (RSLR)—which primarily results from the extraction of groundwater or other sequestered resources such as petroleum deposits (e.g. in the Yellow river delta – see Liu et al., 2015). The Chao Phraya is a salient example of the impacts of groundwater extraction; in areas surrounding the Chao Phraya, such extraction has led to subsidence causing ground levels to fall by up to 2 m, with some regions of Bangkok now residing more than 1 m below mean sea level (Phien-wej et al., 2006). Subsidence is also estimated to be the cause of approximately 60% of coastal retreat to either side of the mouth of the Chao Phraya (Bidorn, 2016, see also Saito et al. 2007).

In addition to the ‘upstream’ impacts relating to river discharges described above, delta formation is also strongly dependent on ‘downstream’ processes in the depositional environments into which rivers discharge. Such processes can be categorised as relating to either waves or tides in the short term, as well as the (related) longer term effects of climate change, the latter primarily comprising sea level rise and changes to weather patterns (Fox-Kemper et al., 2021; Seneviratne et al., 2021). Given the noted predominance of human settlement in deltas within latitudes subject to tropical cyclones, as well as the projected increases in cyclone frequency (Seneviratne et al., 2021), it is likely that many deltas will be subject to higher energy wave climates in future (although it is worth noting that the complexity of climate change is such that wave energy may also be reduced in some areas – see e.g. Reeve et al., 2011). Climate change also has potential repercussions for intensity of rainfall events, which may affect upstream fluxes of water and sediment.

1.2 Problem statement

A river delta is a complex sediment formation, subject to a broad range of processes controlling its form and development. Of particular importance amongst these are waves, tides, and river discharge (Galloway, 1975; Bird, 2008). A substantial body of work exists in which numerical models have been used to investigate the ways in which these processes affect the development of deltas (see Chapter 2). Such studies have modelled delta formation as affected by: waves without tides (e.g. Geleynse et al., 2011; Lageweg and Slangen, 2017; Gao et al., 2018, 2019, 2020; Liu et al., 2020); tides without waves (e.g. Geleynse et al., 2011; Guo et al., 2015;

Rossi et al., 2016; Lageweg and Slangen, 2017; Zhou et al., 2020); or combinations of small waves and tidal ranges (e.g. Broaddus et al., 2022). However, little attention has been paid to the conditions under which delta formation may be inhibited or prevented, nor to identifying the thresholds of such conditions that separate delta-forming rivers from non-delta-forming rivers. The interaction between waves and tides in particular has not been well explored (Edmonds et al., 2021) (while Broaddus et al. 2022 investigated delta development under combined waves and tides, their work focuses on describing the characteristic features of the resultant morphologies, without investigating the specific *processes* that lead to such morphologies). Given the discussed vulnerability of deltas, in combination with the sediment-starving effects of river management and changes to weather due to climate change (Fox-Kemper et al., 2021; Seneviratne et al., 2021), developing our understanding of the processes which control delta development—and the potential of these processes to inhibit or prevent formation—will help us to protect and perhaps restore these vulnerable environments.

1.3 Objectives of this thesis

The primary objective of the present work is to use a well-established and validated model (Delft3D 4) to test the hypothesis that delta formation may be prevented—or strongly inhibited—under the combination of significant wave heights and tidal ranges of sufficient magnitude, where all other conditions remain unchanged. A secondary objective is to describe and classify the range of processes by which potentially delta-forming river and coast systems develop under differing combinations of these two parameters, and to position any observations made within the context of existing literature concerning the formational limits and classification of deltas (e.g. Nienhuis et al., 2015, 2018, 2020; Caldwell et al., 2019).

1.4 Thesis outline

This thesis comprises nine chapters, plus four appendices.

Chapter 1 (this chapter) gives an overview of the threats to river deltas, perceived knowledge gap, and objectives of the research presented herein. Chapter 2 provides a review of existing literature regarding delta formation, classification, and formational limits. Chapter 3 presents a brief description of the Delft3D model. Chapter 4 covers a range of sensitivity and calibration tests informing the model setup. Chapter 5 describes the setup of the simulations used to investigate the process-related limits of delta formation, as well as the methods used to analyse simulation results. Chapter 6 presents the simulation results. Chapter 7 presents the formational regime framework applied to the simulation results, and describes the formational processes observed. Chapter 8 compares Delft3D simulation results to the estimation of alongshore sediment diffusion by waves and tides using a simple diffusion formula. Chapter 9 gives the conclusions and recommendations of this thesis.

Chapter 2

Review of the formational processes, classification, and limits of river delta formation

Here, we review the existing body of work concerning the processes by which river deltas develop. Such processes can be broadly split into two categories: the *formational* processes by which the development of deltas is often described (primarily avulsion and mouth bar induced bifurcation), and the *influencing* processes by which the formational processes are affected (primarily waves, tides, and river discharge). It should be noted that the literature regarding the effects of waves or tides generally investigates these processes independently—i.e. the interaction of waves and tides is rarely considered. The classification of deltas—both in terms of which coastal morphologies are or are not considered deltaic, as well as work regarding the classification of different types of deltaic morphology—is also reviewed. Finally, we review work which considers the thresholds—in terms of the influencing processes—which divide delta formation / growth from delta prevention / shrinking.

2.1 River deltas and the processes that shape them

As noted, there are three dominant influencing processes which affect delta formation: river discharge, waves, and tides (Bird, 2008). Rivers deliver the majority of sediment required for a delta to form, while waves and tides induce changes to patterns of sediment transport and deposition, hence exerting control on the resulting morphology (see e.g. Galloway, 1975; Orton and Reading, 1993; Leonardi et al., 2013; Anthony, 2015; Nienhuis et al., 2018; Broaddus et al., 2022). Based on their observed morphology, deltas have long been qualitatively categorised as wave-, tide-, or river-dominated (Galloway, 1975; Orton and Reading, 1993). Elongated-channel or "birds-foot" type deltas are associated with river-dominance (and sediment cohesiveness – see Orton and Reading, 1993); cuspate type deltas with wave-dominance (Komar, 1973; Dominguez, 1996; Ashton and Giosan, 2011); and deltas forming within funnel-shaped embayments featuring numerous downstream-widening channels and elongated islands with tidal-dominance (Orton and Reading, 1993; Hoitink et al., 2017). Despite the ubiquity of these classifications in recent literature, they remain broadly qualitative. However, some recent studies have taken steps towards formalising and quantifying them (Nienhuis et al., 2015, 2018, 2020, see §2.2).

The formational processes predominantly described within existing literature are mouth-bar induced channel bifurcation (splitting), and avulsion (see e.g. Edmonds and Slingerland, 2010). Bifurcation occurs where sediment carried within the discharging jet at the end of a channel is deposited to form a central bar around which flow divides, leading to channel branching (Edmonds and Slingerland, 2007). Avulsion occurs where an existing channel overtops its banks at some location along its length, leading to the full or partial abandonment of that channel in favour of one or more alternative flow paths (Hoyal and Sheets, 2009; Edmonds et al., 2009). The mechanisms of avulsion are complex but predominantly follow on from downstream channel lengthening and mouth bar growth, which may in some circumstances lead to upstream-propagating water level increases and associated bed level increases related to in-channel sediment deposition. Such increases may in turn result in a channel overtopping its banks, initiating the avulsion process (Hoyal and Sheets, 2009; Edmonds et al., 2009). Delta formation under strong wave influence is typically characterised by the offshore expansion of the shoreline to either side of the discharging river mouth (Komar, 1973; Dominguez, 1996; Ashton and Giosan, 2011).

2.1.1 The effects of waves on river deltas

The effects of waves on delta development may be approximately divided into their interaction with mouth bars, and their interactions with existing deltaic features more broadly.

Waves affect mouth bar formation through two mechanisms: firstly, by deflecting or spreading the discharging jet at a channel mouth (Geleynse et al., 2011); and secondly, by mobilizing sediments directly in shallow water and hence locally increasing sediment transport rates (Nardin and Fagherazzi, 2012; Liu et al., 2020). In general, these effects lead to a slowing of mouth bar formation as more sediment bypasses the river mouth to be deposited further into the basin (Jerolmack and Swenson, 2007; Geleynse et al., 2011). Where this occurs, channels increase in length more slowly and sediment—much of which is no longer deposited to form a mouth bar—is now distributed more broadly throughout the submerged margins of the delta, leading to smoother shoreline (Ratliff et al., 2018). The slowing of mouth bar growth also clearly implies a reduction in overall channel numbers, which is observed in previous modelling studies (Geleynse et al., 2011; Liu et al., 2020). Relatedly, the slowing of channel extension and mouth bar growth also result in a reduction in avulsion frequency, as the upstream-propagating patterns of deposition and water level increases described in §2.1 are less likely to occur (Anthony, 2015). In some circumstances, where waves are small (significant wave heights ≤ 0.8 m) and travel opposite to the mean direction of the discharging jet, mouth bar formation has been shown to occur up to 35% closer to the river mouth and 40% faster in comparison to the equivalent situation without waves (Nardin et al., 2013). Under very large waves, mouth bar formation may not occur at all, potentially leading to the formation of cuspate deltas (Komar, 1973; Anthony, 2015).

Waves also induce ongoing morphological development of deltas through further transport of sediments within shallow regions at the delta periphery, whether by continual transport or remobilisation of settled sediment. Waves within these regions will in general move sediment both on and alongshore, depending on their mean angle of approach. This means that sediments delivered to the depositional basin are reworked by waves. This leads to the formation of morphological features including spits and barrier islands under low to moderate wave energy, and "strand-plains" (see Figure 2.1) under higher wave energy (Komar, 1973; Dominguez, 1996; Anthony, 2015; Broaddus et al., 2022). Such features typify moderate wave influence on deltas. Waves are also noted to cause discharging channels to preferentially orient either directly opposite the dominant wave direction, or to be deflected away from the dominant wave direction, depending somewhat on the strength of waves and instantaneous relative orientations of the channel and waves (Nardin and Fagherazzi, 2012). Where mean wave angles of approach are generally oblique to the shoreline, a net alongshore transport in one direction may also be expected to develop. However, alongshore transport can be blocked at the discharging ends of channels; a result of the "hydraulic groyne" effect. This effect denotes a tendency for sediment—when transported alongshore towards a discharging channel mouth—to become trapped in the up-wave direction, as the discharging jet of the channel prevents sediment from bypassing the channel mouth (Ashton and Giosan, 2011; Anthony, 2015). This can lead to asymmetric deltas with broad sediment deposits on the up-wave side, and development of, for example, long spits on the down-wave side (Nardin and Fagherazzi, 2012). An example of this type of morphology can be seen in Figure 2.2, which shows the mouth of the Saint George distributary of the Danube river.

Figure 2.1: The Caravelas strandplain in Brazil. A strandplain can be thought of as a sequential outward ‘layering’ of beaches over time (NASA Earth Observatory, 2006). Visual evidence of this beach layering can be seen throughout the satellite image shown, wherein the visual demarcation is typically a result of vegetated dune formation.

Figure 2.2: The Saint George distributary of the Danube and surrounding land. This stretch of coast is subject to moderately strong waves (annual mean significant wave height of ∼1.4 m – Caldwell et al., 2019) and very low tidal variation (maximum tidal range of ∼0.12 m – Vespremeanu-Stroe et al., 2017) (Google Earth 10.55.0.1, 2019).

2.1.2 The effects of tides on river deltas

Observed changes to delta development under the imposition of tides occur primarily as a result of local variation in water level and discharge rate within delta channels. Within the vicinity of discharging rivers / channels, during flood tides water levels rise and volumetric discharges are reduced, and during ebb tides water levels fall and volumetric discharges are increased. This leads to a slowing of delta area growth during flood tides with increased in-channel deposition, followed by the concentration of flow into delta channels with an associated increase in velocities during ebb tides. This latter effect leads to an increase in distributary length—as in-channel sediment is transported to the ends of channels during ebb—as well as both net-deepening and widening of channels (Geleynse et al., 2011; Guo et al., 2015; Lageweg and Slangen, 2017; Nienhuis et al., 2018). Increasing tidal range has also been linked to an increase in shoreline roughness and channel sinuosity (Geleynse et al., 2011). Furthermore, increasing tidal range leads to the formation of wider mouth bars which, under sufficiently large tidal ranges, may themselves be split in half during ebb tides, resulting in a "trifurcation" of flow (Leonardi et al., 2013). Tides are also associated with increased stability of channel splits—i.e. both downstream arms of a channel split are maintained under tidal forcing rather than one becoming inactive (Hoitink et al., 2017; Iwantoro et al., 2020).

2.2 Classification of deltas

Efforts to classify different types of delta go back at least as far as Galloway (1975), wherein deltas are classified according to the relative influence of each of waves, tides, and rivers. Galloway's "tripartite" classification system is shown in Figure

2.3a, alongside salient examples of deltas classified by influencing processes (Figures 2.3b to g), as determined by the author. Later work by Orton and Reading (1993) expanded upon this classification, additionally emphasising the importance of sediment size (and hence cohesion) in influencing delta morphology. In their work, the elongate form of the Mississippi delta in particular is highlighted as relating more to the presence of cohesive sediments than to the relative importance of river discharge. More recently, approaches to quantifying classification by process influence have been developed (Nienhuis et al., 2015, 2018, 2020). These involve the determination of characteristic sediment fluxes resulting from each process (in which sediment size and cohesion is implicitly accounted for). The relative dominance of each process is then considered to be proportional to the relative magnitude of the respective characteristic flux. Further discussion of the methods of Nienhuis et al. (2015, 2018, 2020), as applied to the simulations presented in this thesis, can be seen in Chapter 7. Later work by Broaddus et al. (2022) emphasised the presence (or absence) of particular morphological features in classifying process-influence on delta formation; specifically, they highlight the number of channel mouths intersecting the shoreline, 'roughness' of the shoreline, and the presence of spits as morphological indicators of the balance of process influence.

In addition to the classification of deltas by dominant formational processes, the precise classification of which morphologies should or should not be considered to be deltas at all remains poorly defined. This is to some extent a semantic distinction, but if we accept that the typical markers of deltaic morphologies involve the accumulation of sediment close to river mouths, and that the lack of such signi-

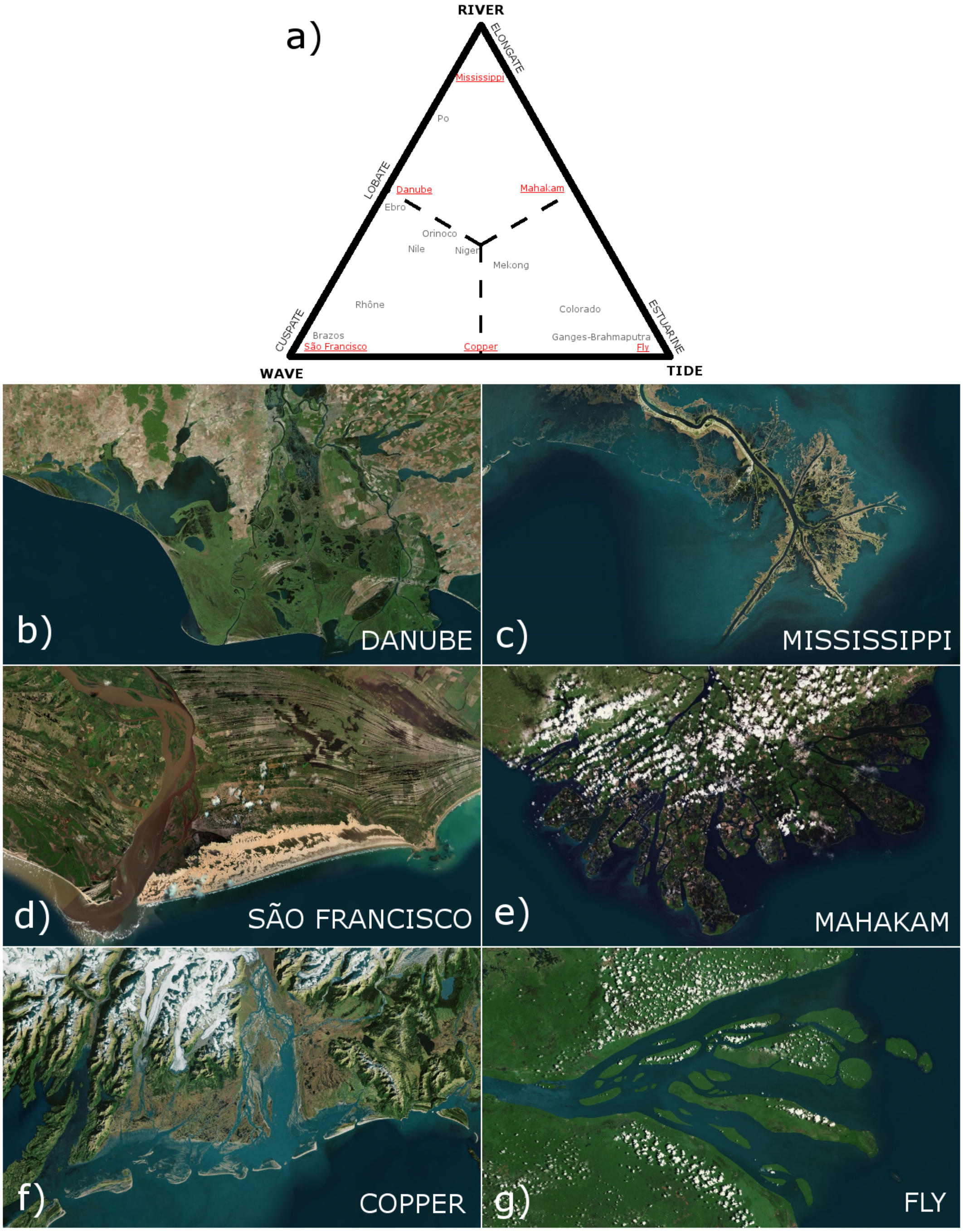

Figure 2.3: Examples of deltas categorised by process influence, as defined by Galloway (1975): a) the "tripartite" classification of Galloway (1975), wherein proximity of delta to a particular corner of the triangle indicates the relative morphological importance of each influencing process; and b to g) deltas associated with rivers highlighted in red in (a). (Figure adapted from Galloway 1975.)

fies a non-deltaic morphology, then the distinction becomes significant. The first recorded usage of the term "delta" to describe an accumulation of sediment around the mouth(s) of a river was by Herodotus around 450 BCE (Coleman, 1981); this was in reference to the Nile delta, due to its approximate similarity in shape to the Greek letter Δ. (While many of the world's deltas are not in fact triangular in shape, the notion that a delta should be triangular is a persistent etymological fallacy—see e.g. Collins Dictionaries 2024.) As an example of a common definition that can be shown to produce false negatives, several authors state that a delta is a "discrete shoreline protuberance" of deposited sediment (or similar statement to that effect – see e.g. Orton and Reading, 1993; Overeem et al., 2005; Bird, 2008). However, this definition omits several salient example of major deltas—such as those of the Amazon and Orinoco rivers—which do not form shoreline protuberances. Syvitski et al. (2022a) reviewed the historic use of the term "delta", and offered the novel definition that deltas are "subaerial landforms that cap underlying deposits with subaqueous extensions that result from a river feeding sediment directly into a standing body of water at a rate that overwhelms any effective dispersal processes derived from the ambient basin." (The term "subaerial" refers to land which emerges above water at low tide, and "subaqueous" to land which is always submerged.) Even this exhaustive definition is arguably not sufficiently accurate as it encompasses, for example, open estuarine regions of water with relatively small bars that become partially emergent only during low tides. In this way, the definition of Syvitski et al. (2022a) contrasts with several earlier definitions that they themselves discuss, wherein the presence of a distributary network of channels is often cited as a criterion for classification as a delta (see Syvitski et al., 2022a, supplementary material). A broader set of criteria is offered by Caldwell et al. (2019), who identify deltas following analysis of aerial or satellite imagery. They suggest that a delta exists where "the river-mouth area contains an active or relict distributary network, ... ends in a subaerial depositional protrusion from the lateral shoreline, ... or does both". While this definition improves upon those discussed above by including deltaic morphologies that the prior definitions would erroneously omit, Caldwell et al. (2019) themselves note that their approach may still result in false negatives where morphology comprises only a single channel with no coastal extension; a configuration which they acknowledge might also be argued to be deltaic.

The above discussion concerns the classification of deltas by their shoreward extents and morphologies, but the landward limits of deltas are also subject to a degree of ambiguity in their precise location (Edmonds et al., 2020). For example, much of the Lower Central Plain of Thailand comprises sediments delivered by the Chao Phraya and its tributaries / distributaries over the past ∼7000 yr, as the delta(s) advanced and merged to fill in what was once the Gulf of Ayutthaya (Tanabe et al., 2003). As such, we might consider a significant proportion of the Lower Central Plain to be deltaic; an area of approximately 10000 km^2. This does, however, make it difficult to discern the landward limits of the delta, particularly as much of this land is built-up by human settlement. An aerial view of the Lower Central Plain and estimated location of the shoreline at its furthest-inland position during the Mid-Holocene can be seen in Figure 2.4. Other substantial deltaic regions which have formed over similar timescales to this region include those of the Mississippi (Roberts, 1997), Mekong (Ta et al., 2002), and Ganges-Brahmaputra (Bandyopadhyay, 2007). A complete discussion of this topic is not offered here, as its impact on the interpretation of the numerical simulations presented herein is relatively minor. This observation is made primarily to further highlight that the precise definition of a delta remains a topic of ongoing debate. For example, efforts to estimate deltaic land areas globally by Nienhuis et al. (2020) have been questioned by Zăinescu et al. (2023). Here we define our own criteria for delta identification (see §5.2), but acknowledge that we may in some circumstances classify (or reject) certain morphologies as deltaic, which might be classified differently under alternative definitions.

2.3 Thresholds of delta development

The threshold between a delta forming or not is often presented as a balance of (riverine) import and (marine / lacustrine) export of sediment (see e.g. Galloway, 1975; Orton and Reading, 1993; Caldwell et al., 2019; Syvitski et al., 2022a). This simple model implies that where import rates exceed export rates, a delta forms; where they are the same, a delta stagnates, and where export rates exceed import rates, a delta recedes. In their analysis of rivers globally, Caldwell et al. (2019) quantified this notion by deriving a simple formula estimating probability of delta presence for a given river and coast system (see §5.1). Implicit in this formula is that larger river discharges (of both water and sediment) increase delta likelihood, whereas larger significant wave heights and tidal ranges reduce delta likelihood. While useful, this simple model of delta likelihood does not elucidate the complexity inherent to the interaction between—and variation within—processes.

Figure 2.4: Aerial view of Lower Central Plain of Thailand and Upper Gulf of Thailand. The red dashed line indicates the estimated location of the shoreline as of approximately 7000 years ago, according to Tanabe et al. (2003). Four rivers—the Bang Pakong, Chao Phraya, Tha Chin (which is a distributary of the Chao Phraya), and Mae Klong—feed into the Upper Gulf of Thailand and have provided, to varying degrees, the sediment comprising much of the present Lower Central Plain (Park et al., 2021). The northern shoreline of the Upper Gulf of Thailand has been retreating since around 1950, due to a combination of land subsidence, sediment starvation, and coastal deforestation / mismanagement (Phien-wej et al., 2006; Saito et al., 2007; Uehara et al., 2010; Bidorn, 2016; Park et al., 2021).

Where existing literature addresses the destruction of deltaic features, it has typically focused on wave-driven redistribution of sediments forming deltaic lobes which have been partially or fully abandoned—i.e. where river discharge has substantially reduced over time or stopped altogether as a result of upstream abstraction or diversion (Hillen, 2009; Nienhuis et al., 2013; Anthony, 2015). In general, where abandoned delta lobes are subjected to waves, this tends to have a smoothing effect on the local shoreline (Hillen, 2009; Nienhuis et al., 2013). The combination of onshore and alongshore oriented wave-driven flux leads to delta lobes becoming wider and having reduced offshore extent. Where wave climates are asymmetrical, waves also induce a net alongshore transport in the predominant wave direction, typically such that more sediment is removed from the abandoned lobe than is delivered to it (see e.g. discussion of the nascent Moulaya river delta in Anthony, 2015). Notably, none of these studies consider tidal interaction with waves. The importance of such interaction is emphasised by Orton and Reading (1993), who note that the degree of influence that tides impart on a delta is related to wave energy, as tides act to "distribute wave energy over a larger portion of the beach". The ways in which these processes interact, and the resulting effects on delta development or prevention, represents a significant knowledge gap (Edmonds et al., 2021) which this thesis aims to address.

Chapter 3

Delft3D 4 – model description

All simulations presented in this thesis use the open source modelling software suite Delft3D 4 (Deltares, 2021a,b) (for brevity, subsequent references to Delft3D omit the '4'). In this chapter, the governing equations of Delft3D are briefly presented (§3.1). Only the fundamental equations—describing hydrodynamics (§3.1.1), morphodynamics (§3.1.2), sub grid scale turbulence (§3.1.3), and waves (§3.1.4)—are included here. References are given throughout for further details and equations where these are not included in the descriptions provided here.

3.1 Governing equations

The section presents an overview of the fundamental Delft3D equations. The equations are somewhat simplified as compared to how they appear in the Delft3D literature, as terms and factors that do not apply to our simulations are omitted.

3.1.1 FLOW – Hydrodynamics

3.1.1.1 The shallow water equations (SWEs)

Hydrodynamics are calculated using the (depth-averaged[1]) shallow water equations:

$$\frac{\partial U}{\partial t}+U\frac{\partial U}{\partial x}+V\frac{\partial U}{\partial y}=-g\frac{\partial \zeta}{\partial x}-\frac{gU\sqrt{U^2+V^2}}{C^2h}+\nu_H\left(\frac{\partial^2 U}{\partial x^2}+\frac{\partial^2 U}{\partial y^2}\right)+M_x \quad (3.1)$$

$$\frac{\partial V}{\partial t}+U\frac{\partial V}{\partial x}+V\frac{\partial V}{\partial y}=-g\frac{\partial \zeta}{\partial y}-\frac{gV\sqrt{U^2+V^2}}{C^2h}+\nu_H\left(\frac{\partial^2 V}{\partial x^2}+\frac{\partial^2 V}{\partial y^2}\right)+M_y \quad (3.2)$$

$$\frac{\partial \zeta}{\partial t}+\frac{\partial\left[hU\right]}{\partial x}+\frac{\partial\left[hV\right]}{\partial y}=0 \quad (3.3)$$

where $U=U\left(x,y,t\right)=\bar{u}+u_s$; $V=V\left(x,y,t\right)=\bar{v}+v_s$ are generalised Lagrangian mean (GLM) velocities [m s^{-1}], comprising depth-averaged Eulerian velocity components $\bar{u}=\bar{u}\left(x,y,t\right)$, $\bar{v}=\bar{v}\left(x,y,t\right)$ plus Stokes-drift velocity components $u_s=u_s\left(x,y,t\right)$, $v_s=v_s\left(x,y,t\right)$; x,y are alongshore and cross-shore Cartesian coordinates respectively [m]; t is time [s]; g is gravitational acceleration [m s^{-2}]; $\zeta=\zeta\left(x,y,t\right)$ is the mean free-surface elevation [m]; ν_H is the horizontal eddy viscosity [m^2 s^{-1}]; C is the Chézy bed friction coefficient [m$^{1/2}$ s^{-1}]; $h=h\left(x,y,t\right)$

---

[1] The limitations of a 2D depth averaged modelling approach should be acknowledged; in comparison to a fully 3D model, such an approach does not allow for density stratification—whether due to sediment concentrations or salinity—and related effects such as salt wedge intrusion and gravity currents. Such processes can strongly affect patterns of sediment deposition under certain conditions (see e.g. Zhou et al., 2020, for discussion on this point). However, we maintain a 2DH approach for two reasons: firstly, for comparability to previous studies, where such an approach is common; and secondly, as the additional computational expense and storage requirements for fully 3D modelling are significant.

is the mean water depth [m]; and $M_x = M_x\left(x, y, t\right)$, $M_y = M_y\left(x, y, t\right)$ are contributions due to wave energy dissipation determined from WAVE calculations [m s^{-2}] (see §3.1.4).

The horizontal eddy viscosity term ν_H in Eqs. (3.1) and (3.2) represents diffusion of momentum due to sub-grid scale (SGS) turbulence and 3D effects not resolved by the 2DH model. Within this 2DH modelling approach, ν_H is defined as the sum of two parts: $\nu_H = \nu_H^{sgs} + \nu_H^{back}$, where $\nu_H^{sgs} = \nu_H^{sgs}\left(x, y, t\right)$ is a contribution calculated using the (optional) SGS turbulence model (Uittenbogaard and Vossen, 2004; Deltares, 2021a), and ν_H^{back} is a user-defined constant background value. The SGS turbulence model is described in §3.1.3.

Eqs. (3.1) to (3.3) are discretised and solved on a staggered grid. For all simulations presented in this thesis, one or more regularly spaced square grids are used, with discrete grid sizes Δx [m] and Δy [m] in the x- and y-directions respectively (in some simulations, a larger grid size is used within the domain representing the river; river domain grid sizes in these cases are denoted by Δx_r and Δy_r). The set of discretised equations is solved over discrete numerical time steps Δt [s] using an Alternating Direction Implicit (ADI) scheme. Selection of Δt is made following a range of Courant stability criteria as outlined in Deltares (2021a); in most cases it is sufficient to satisfy the standard Courant-Friedrichs-Lewy (CFL) criterion (Courant et al., 1928), wherein the CFL number is:

$$C_f = c\frac{\Delta t}{\min\left(\Delta x, \Delta y\right)} \tag{3.4}$$

where $c = c\left(h\right) = \sqrt{gh}$ is the celerity of a surface disturbance [m s^{-1}]. For an explicit solution method, we typically require $C_f \leq 1$, which implies that any surface disturbance travels no more than one grid interval in a single time step. However, for the ADI solution used by Delft3D, the model is stable for C_f values up to approximately 10.

3.1.2 FLOW – Sediment transport

For most simulations presented in this thesis, sediment transport is calculated using the Soulsby / Van Rijn (SVR) transport formulae of Delft3D FLOW (Soulsby, 1997; Deltares, 2021a). The SVR formulae are relatively simple and well-established, and produced morphologies matching those expected for wave-affected coasts during initial testing (Galloway, 1975; Orton and Reading, 1993; Anthony, 2015, see also §2.1.1 and §4.3). While the SVR formulae are not appropriate in all cases—such as when applied to 1D modelling of beach profile development—their application to circulation of sediments over rippled beds in a 2DH coastal model is here considered to be an appropriate application.

Note that while the Van Rijn (1993) (VR93) and Engelund-Hansen (EH) formulae have been commonly used in prior delta modelling studies (e.g. Edmonds and Slingerland, 2010; Geleynse et al., 2010, 2011; Caldwell and Edmonds, 2014; Burpee et al., 2015; van der Vegt et al., 2016; Gao et al., 2019), we found these formulae to be unable to satisfactorily model morphodynamic development under the influence of waves. The VR93 formulae produced physically unrealistic results—particularly exhibiting excessive scour close to the shoreline (see §4.3)—while EH is unable to incorporate first-order wave-transport effects at all.

3.1.2.1 The Soulsby / Van Rijn sediment transport equations

The SVR equations for bedload transport rates $q_{b,x}$ and $q_{b,y}$ [m^3 s^{-1} m^{-1}] in the x- and y-directions respectively are:

$$q_{b,x} = 0.005h \left[\frac{1}{(s-1)\,gh} \right]^{1.2} \left[\sqrt{\bar{u}^2 + \bar{v}^2 + \frac{0.018}{C_D} u_{rms}^2} - u_{cr} \right]^{2.4} \bar{u} \tag{3.5}$$

$$q_{b,y} = 0.005h \left[\frac{1}{(s-1)\,gh} \right]^{1.2} \left[\sqrt{\bar{u}^2 + \bar{v}^2 + \frac{0.018}{C_D} u_{rms}^2} - u_{cr} \right]^{2.4} \bar{v} \tag{3.6}$$

where s is relative grain density [-], equal to the ratio of grain density ρ_s [kg m^{-3}] to water density ρ_0 [kg m^{-3}]; C_D is a coefficient representing current-induced drag [-]; $u_{rms} = u_{rms}(x, y, t)$ is root mean square orbital velocity of waves [m s^{-1}]; and u_{cr} is critical bed shear velocity [m s^{-1}]. For expressions determining C_D, u_{rms}, and u_{cr}, refer to the FLOW manual (Deltares, 2021a) and Soulsby (1997). Bedload fluxes are further modified to account for the effects of both transverse and longitudinal bed slope following the methodologies of Ikeda (1982) and Bagnold (1966) respectively (Deltares, 2021a). When modelling multiple distinct sediment fractions, calculated bedload fluxes per fraction are also reduced proportionally to the fraction of that sediment available in the uppermost (transport) layer (see §3.1.2.3).

Suspended sediment transport in Delft3D is determined using an advection-diffusion equation (see §3.1.2.2). While a notional suspended sediment flux magnitude is first calculated using the SVR formulae, this value is in fact used by the model to determine the rate of change of suspended sediment concentration in the water column. The steps involved in calculating this notional sediment flux and then converting it to the rate of change of suspended sediment concentration are outlined here. A volumetric suspended sediment flux (per meter width) q_s [m^3 s^{-1} m^{-1}] is first calculated using SVR (Soulsby, 1997; Deltares, 2021a):

$$q_s = 0.012 D_{50,\ell} \left[\frac{D_{*,\ell}^{-0.6}}{\left(\left(s-1 \right) g D_{50,\ell} \right)^{1.2}} \right] \left[\sqrt{\bar{u}^2 + \bar{v}^2 + \frac{0.018}{C_D} u_{rms}^2} - u_{crit} \right]^{2.4} \sqrt{\bar{u}^2 + \bar{v}^2} \tag{3.7}$$

where $D_{50,\ell}$ [m] is median grain diameter of the given sediment fraction ℓ; and $D_{*,\ell}$ [-] is dimensionless grain diameter of the given sediment fraction ℓ (Soulsby, 1997). To convert this transport rate into a rate of entrainment / deposition for use in the model, q_s is first used to determine an equilibrium concentration $c_{eq} = q_s / (h\sqrt{\bar{u}^2 + \bar{v}^2})$ [m^3 m^{-3}] (c_{eq} can be thought of as the expected sediment concentration under stationary flow conditions). c_{eq} is then used to determine a sediment source / sink term S [m^3 m^{-3} s^{-1}], representing the rate of change of concentration due to deposition / entrainment:

$$S = \frac{c_{eq} - \bar{c}}{T_s} \tag{3.8}$$

where $\bar{c}$ is depth-averaged sediment concentration [m^3 m^{-3}]; and T_s is a relaxation time-scale [s] (see Lesser, 2009; Deltares, 2021a). When modelling multiple sediment fractions, equilibrium concentrations c_{eq} are reduced proportionally to the fraction of the given sediment available in the uppermost (transport) layer (see §3.1.2.5).

3.1.2.2 The advection-diffusion equation

The advection-diffusion equation is:

$$\frac{\partial\left[h\bar{c}\right]}{\partial t}+\frac{\partial\left[hU\bar{c}\right]}{\partial x}+\frac{\partial\left[hV\bar{c}\right]}{\partial y}=h\left[\frac{\partial}{\partial x}\left(\epsilon_H\frac{\partial\bar{c}}{\partial x}\right)+\frac{\partial}{\partial y}\left(\epsilon_H\frac{\partial\bar{c}}{\partial y}\right)\right]+hS \tag{3.9}$$

where ϵ_H is horizontal eddy diffusivity [m^2 s^{-1}]. Similarly to ν_H, ϵ_H is defined as: $\epsilon_H=\epsilon_H^{sgs}+\epsilon_H^{back}$, where ϵ_H^{sgs} [m^2 s^{-1}] represents additional sediment diffusion due to SGS turbulence; and ϵ_H^{back} [m^2 s^{-1}] represents additional sediment-diffusing processes which are not resolved in a 2DH simulation (see §3.1.3.2).

As with the hydrodynamic equations, Eq. (3.9) is also solved using an ADI scheme (see Deltares, 2021a).

3.1.2.3 Bed level updating

Generally, changes to bed elevation $z_b=z_b\left(x,y,t\right)$ [m] due to sediment transport can be described by an Exner (1925) equation of form:

$$\xi\frac{\partial z_b}{\partial t}=-\left\{\frac{\partial q_{b,x}}{\partial x}+\frac{\partial q_{b,y}}{\partial y}\right\}+D-E \tag{3.10}$$

where D (E) is deposition (erosion) rate per unit area [m s^{-1}]; and $\xi=1-n$ is a factor allowing for void-space in the bed [-], with n the proportion of voids [-].

Rearranging, discretizing, introducing the morphological acceleration factor f_m (see below) [-], and substituting $D-E=Sh$, Eq. (3.10) becomes:

$$\Delta z_b=\frac{f_m\Delta t}{\xi}\left(\frac{\left[q_{b,x}\left(x\right)-q_{b,x}\left(x+\Delta x\right)\right]}{\Delta x}+\frac{\left[q_{b,y}\left(y\right)-q_{b,y}\left(y+\Delta y\right)\right]}{\Delta y}+Sh\right).$$

Inclusion of the morphological acceleration factor f_m is a model acceleration technique that allows for morphodynamic updating to proceed on a faster timescale than that of the hydrodynamics (Lesser, 2009; Roelvink and Reniers, 2011), and is typically $\mathcal{O}\left(10\right)$ to $\mathcal{O}\left(10^2\right)$ in delta modelling studies (e.g. Geleynse et al., 2010; Edmonds and Slingerland, 2010; Burpee et al., 2015; Zhou et al., 2020). See §4.5 for calibration of the value f_m used in the simulations presented in this thesis.

3.1.2.4 Dry cell erosion

Where bedload transport or entrainment of sediment into suspension occurs in a cell with one or more adjacent dry cells, some or all of that transport may be optionally sourced from the adjacent dry cells rather than the wet cell itself. This is achieved by the application of the dry cell erosion factor $\Theta = \Theta\left(h\right)$ [-]. Possible values of Θ range from 0 to 1, where $\Theta = 0$ implies that no sediment is sourced from adjacent dry cells, and $\Theta = 1$ implies that all sediment is sourced (evenly) from all adjacent dry cells. Θ is calculated as:

$$\Theta\left(h\right) = \min\left\{\left(\frac{h - H_{sed}}{H_{max,\Theta} - H_{sed}}\right)\Theta_{SD}, \Theta_{SD}\right\}, \qquad \text{for } h \geq H_{sed} \tag{3.11}$$

where Θ_{SD} is the user-defined maximum value of Θ, set in the range $(0 \leq \Theta_{SD} \leq 1)$; $H_{sed} = 0.1$ m is a model parameter representing the depth below which sediment transport calculations are disabled; and $H_{max,\Theta}$ is a threshold depth [m], such that $\Theta = \Theta_{SD}$ where $h = H_{max,\Theta}$, reducing linearly to $\Theta = 0$ at $h = H_{sed}$. The relationship between Θ and h is illustrated in Figure 3.1. This approach represents a simple method for behaviour-based modelling of bank and bar erosion (Lesser, 2009), which is otherwise not accounted for by the model.

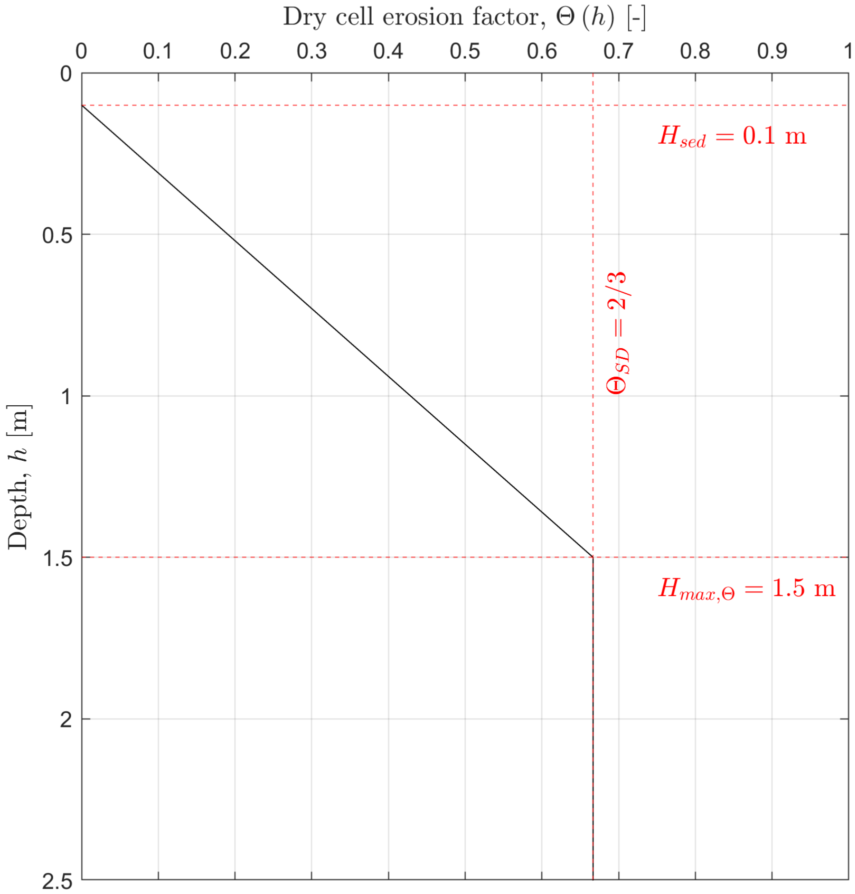

Figure 3.1: Plot of $\Theta(h)$ (Eq. (3.11)), with example values of $H_{sed} = 0.1$ m, $H_{max,\Theta} = 1.5$ m, and $\Theta_{SD} = 2/3$.

3.1.2.5 Sediment bed

When using only a single sediment fraction, a single bed layer is sufficient to track sediment in the bed. For simulations presented in this chapter, only a single sediment fraction, and hence single sediment bed layer, is used. For simulations presented later in this thesis, two sediment fractions are used; this necessitates the implementation of multiple bed layers so as to be able to track the layering of different sediments over time (Deltares, 2021a). Each layer tracks the proportion of each sediment fraction present. When implementing multiple sediment layers, an upper transport layer is defined, to which all calculated bedload fluxes and deposition / erosion are applied. The thickness of this transport layer may be set as either absolute or proportional to either water depth or bed-form height (the latter being applicable only to sediment transport formulae not discussed in this thesis). Below this lies a user-defined number of 'intermediate' subsurface layers, with maximum thicknesses also set by the user. Finally, below these user-defined intermediate layers lies a (typically thicker) bottom layer, which extends down to the inerodible basement level.

As bed elevations change over time, the upper transport layer may move up or down, but will retain the thickness defined in the model setup. If bed levels rise such that the first layer below the transport layer would exceed its defined maximum thickness, a new layer will be created below the transport layer, and the lowest two layers–i.e. the bottom layer and lowest intermediate layer—will be merged. If bed levels fall, then sediments from the first layer below the transport layer will be gradually incorporated into the transport layer. If this process results in that layer being fully incorporated into the transport layer, then a new layer is created below the lowest layer other than the bottom layer, for which sediment composition is proportionally the same as that of the bottom layer.

The sediment bed setup used in later simulations with multiple sediment fractions is described in Chapter 5.1.

3.1.3 Sub-grid scale turbulence model

Numerical hydrodynamic models are inherently unable to simulate turbulent eddies with approximate width less than the grid size and / or duration less than the numerical time step (Pope, 2000; Chung, 2002). In order to account for the momentum- and sediment-diffusing effects of turbulence at such length scales, an SGS turbulence model may be used (Deltares, 2021a). Broadly, the SGS model is based upon the eddy viscosity concept, which relates small-scale turbulence to additional diffusion of momentum (and sediment).

3.1.3.1 Horizontal diffusion of momentum due to SGS turbulence

Horizontal diffusion of momentum due to SGS turbulence ν_H^{sgs} [m^2 s^{-1}] is given by:

$$\nu_H^{sgs} = \frac{1}{k_s^2}\left(\sqrt{\left(\gamma\sigma_T S^*\right)^2 + B_d^2} - B_d\right) + \nu_H^{3D} \tag{3.12}$$

where k_s is the (turbulent) wave number above which the SGS model is intended to be applied [m^{-1}]; γ is a factor allowing for application to either 2D or 3D models and for differing slopes within the turbulent energy density spectrum [-]; σ_T is the turbulent Schmidt number [-]; S^* is the strain rate tensor [s^{-1}]; B_d is a variable allowing for dissipation of turbulent energy due to flow-bed interaction [s^{-1}]; and

ν_H^{3D} is an optional term representing turbulence resulting from shear dispersion [m^2 s^{-1}], defined as

$$\nu_H^{3D} = \frac{1}{6}\kappa u_* h \tag{3.13}$$

where $\kappa = 0.4$ is von Kárman's constant [-]; and u_* is bed-shear velocity [m s^{-1}] (Uittenbogaard and Vossen, 2004).

The cut-off wave number k_s is defined as:

$$k_s^2 = \frac{(\pi f_{lp})^2}{\Delta x \Delta y} \tag{3.14}$$

where f_{lp} is a spatial low-pass filter coefficient [-].

The factor γ is defined as:

$$\gamma = 0.844\sqrt{\frac{1-\alpha^{-2}}{2n_D}} \tag{3.15}$$

where α is the spectral energy density slope, quantifying the rate of transfer of turbulent energy from larger to smaller vortices [-]; and n_D is a factor representing the number of spatial dimensions modelled [-].

The variable B_d is defined as:

$$B_d = \frac{3g\sqrt{\bar{u}^2 + \bar{v}^2}}{4hC^2}. \tag{3.16}$$

The strain-rate tensor S^* is defined as:

$$(S^*)^2 = 2\left(\frac{\partial u^*}{\partial x}\right)^2 + 2\left(\frac{\partial v^*}{\partial y}\right)^2 + \left(\frac{\partial u^*}{\partial y}\right)^2 + \left(\frac{\partial v^*}{\partial x}\right)^2 + 2\frac{\partial u^*}{\partial y}\frac{\partial v^*}{\partial x} \tag{3.17}$$

where u^*, v^*, are the fluctuating parts of the Eulerian velocities [m s^{-1}], defined as:

$$u^* = \bar{u}_n - \langle u\rangle_n, \qquad v^* = \bar{v}_n - \langle v\rangle_n \tag{3.18}$$

where $\bar{u}_n$, $\bar{v}_n$ are Eulerian velocity components at the nth time step [m s^{-1}]; and $\langle u\rangle_n$, $\langle v\rangle_n$ [m s^{-1}] are temporally filtered velocities defined as:

$$\langle u\rangle_n = (1-a)\,\bar{u}_n + a\langle u\rangle_{n-1}, \qquad \langle v\rangle_n = (1-a)\,\bar{v}_n + a\langle v\rangle_{n-1} \tag{3.19}$$

where $a = \exp(-\Delta t/\tau)$ [-]; τ the relaxation time [s]; and $\langle u\rangle_{n-1}$, $\langle v\rangle_{n-1}$ values calculated using Eq. (3.19) at the previous time step (note that $\langle u\rangle_0 = 0$ m s^{-1} is taken as an initial condition at $t = 0$ s).

3.1.3.2 Horizontal diffusion of sediment due to SGS turbulence

Horizontal eddy sediment diffusivity due to SGS turbulence ϵ_H^{sgs} is determined from the turbulent Schmidt number σ_T and ν_H^{sgs}, via the relationship:

$$\sigma_T = \frac{\nu_H^{sgs}}{\epsilon_H^{sgs}}. \tag{3.20}$$

3.1.4 WAVE – Spectral wave action balance equation

The spatial and temporal resolutions used in coastal-scale models are typically too coarse to directly model wind waves. As such, wave conditions are instead represented by spectral action density. Delft3D WAVE models waves using the third-generation SWAN model, for which spectral action density N [$\mathrm{m}^2\,\mathrm{Hz}^{-2}\,\mathrm{rad}^{-1}$]—in (quasi-)stationary mode, i.e. with temporally varying terms omitted—is determined by:

$$\frac{\partial}{\partial x}c_x N + \frac{\partial}{\partial y}c_y N + \frac{\partial}{\partial \sigma}c_\sigma N + \frac{\partial}{\partial \theta}c_\theta N = \frac{P}{\sigma} \tag{3.21}$$

where σ is relative frequency [Hz]; c_x, c_y, c_σ, and c_θ are propagation velocities in, respectively, Cartesian x- and y-space [$\mathrm{m\,s}^{-1}$], frequency-space [$\mathrm{Hz\,s}^{-1}$], and directional-space [$\mathrm{rad\,s}^{-1}$]; and $P = P\left(x, y, \sigma, \theta\right)$ represents energy sinks (sources) related to dissipative (additive) processes [$\mathrm{m}^2\,\mathrm{rad}^{-1}$]. For the simulations presented herein, dissipative processes include whitecapping, wave-breaking, and bottom-friction. The additive process of wind-driven wave generation is omitted. The processes of non-linear wave-interactions (triads and quadruplets) and diffraction are also omitted. Refraction and frequency shift—representing the potential for spectral action density to propagate through directional and frequency bins respectively—are both included. Refer to Deltares (2021b) for equations representing the above processes. Calculated values of P are used to determine the terms M_x and M_y used in Eqs. (3.1) and (3.2).

Note that Eq. (3.21) is shown here in 'stationary' form—i.e. the term representing time-dependence of N is excluded. The stationary application of WAVE assumes that waves as defined at the domain boundaries fully propagate throughout

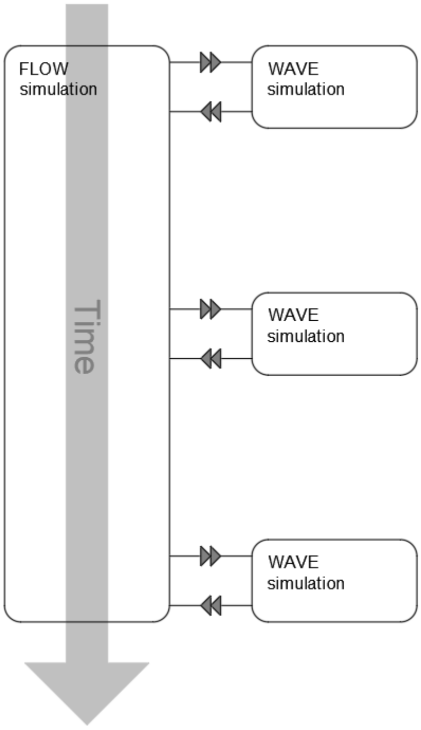

Figure 3.2: Schematic illustrating the coupling of FLOW and WAVE in quasi-stationary mode.

the domain. The modelling approach adopted for FLOW-WAVE coupled models throughout this thesis is in fact 'quasi-stationary'; this approach involves running WAVE (in stationary mode) at discrete intervals during a FLOW calculation, such that the time evolution of the wave-state is represented in any given simulation (see Figure 3.2). The length of temporal interval at which WAVE is run is hereafter referred to as the 'coupling period'.

Chapter 4

Delft3D – sensitivity and calibration testing

In the course of determining an appropriate setup for use in the simulations described and analysed in Chapters 5 through 9, testing was conducted investigating the effects of numerous parameters and other aspects of model setup. The majority of such testing—while essential in terms of correctly calibrating the model—does not usefully inform understanding of the model setup nor model output, and is therefore omitted from this thesis. However, in some cases, these tests elucidate aspects of the model setup which are considered either to be of use in understanding the model, or to provide interesting outcomes in their own right. Such testing is covered in this chapter. §4.1 covers spatial grid convergence testing in FLOW. §4.2 describes sensitivity tests on two different approaches to determining sub grid scale turbulence in Delft3D. §4.3 compares two different options for calculating sediment transport—the Van Rijn (1993) and Soulsby / Van Rijn formulae—when applied to a coupled WAVE-FLOW model. §4.4 investigates the effects of varying the directional distribution of waves at the wave-generating boundary. §4.5 discusses calibration of the morphological acceleration factor for morphodynamic modelling using the Soulsby / Van Rijn transport formulae. And finally, §4.6 compares two different methods—the mathematical morphological method and opening angle method—for defining the shoreline of complex coasts, including those of river deltas. Additionally, some early verification testing of FLOW and WAVE is included as Appendix A.

Some model parameters are common to all simulations presented in this chapter. These are listed in Table 4.1. For the application of parameters relating to the SVR sediment transport model, see Deltares (2021a), and for application of parameters relating to WAVE processes, see Deltares (2021b). The values for WAVE parameters in Table 4.1 are the (recommended) default values given by Deltares (2021b). Note that as numerous sensitivity and calibration tests were conducted over a long period of time, determining the final setup used was an iterative process. As such, many of the simulations presented here have small differences in setup which were typically made in response to previous tests.

4.1 FLOW – Grid convergence testing

This section presents the results of grid convergence testing for Delft3D FLOW. Commonly used performance metrics for analysing grid convergence tests—such as root mean square error (RMSE) analysis, or the Brier skill score (BSS)—have

Table 4.1: Common Simulation Parameters: All Sensitivity and Calibration Tests

Physical Parameters	Symbol	Value	Unit
Gravitational acceleration	g	9.81	$\mathrm{m\,s^{-2}}$
Water density	ρ_0	1000	$\mathrm{kg\,m^{-3}}$
Sediment grain density	ρ_s	2650	$\mathrm{kg\,m^{-3}}$
Sediment dry bulk density	ρ_{bulk}	1600	$\mathrm{kg\,m^{-3}}$
WAVE Parameters			
Depth induced wave breaking ratio	γ_b	0.73	-
Bottom-friction drag coefficient (JONSWAP)	c_b	0.067	$\mathrm{m^2\,s^{-3}}$
Soulsby / Van Rijn Calibration Parameters			
SVR calibration factor	A_{cal}	1.0	-
Characteristic grain size ratio	$D_{90,\ell}/D_{50,\ell}$	1.5	-
Roughness height	z_0	6.0	mm

shortcomings when applied to delta modelling (Bosboom et al., 2014). These primarily result from the tendency for small upstream differences to cause extensive changes downstream. This may cause, for example, an otherwise similar channel to grow in different directions between two simulations with similar setups. It follows that small changes to a simulation's setup, including grid size, may severely alter the resulting bathymetry. Consequently, standard error metrics may produce arbitrarily large errors when comparing one such simulation to another, even when characteristic patterns of delta growth are in fact qualitatively similar.

Given the inappropriateness of common error metrics, model performance over differing grid sizes is instead quantified here in terms of the well-known issue of flow-grid alignment—i.e. the tendency for channels to form following grid-lines in morphodynamic models (Baar et al., 2019). This can result in unnaturally grid-aligned channels with frequent right-angled bends (see e.g. the delta-forming simulations of Liang et al., 2016, Lageweg and Slangen 2017, and Xu et al. 2021). The methodology developed to quantify this alignment—and its results as applied to grid-convergence testing—are presented below.

4.1.1 Model setup

Grid convergence testing in FLOW was carried out using regular, square grids with resolutions of $\Delta x = \Delta y =$ 12.5 m, 25 m, 50 m, 125 m, and 250 m. Common model parameters are given in Table 4.2. The test domain in all cases comprises a 19.75 km alongshore by 9.0 km cross-shore basin, into which a 1.5 km long, 250 m wide river with slope 1:5000 discharges. All simulations are modelled without waves or tides. Lateral basin boundaries are represented by a Neumann-type boundary defining a flat water level gradient in the alongshore direction—i.e. $\partial\zeta/\partial x = 0$ m m^{-1}. The offshore boundary is defined using a constant Riemann type boundary $R^{+}_{D3D} = 0$ m s^{-1} (see Deltares, 2021a). Each simulation represents $T \approx 96$ yr of morphological development. A 500 m wide beach is included adjacent to the onshore boundary. The beach is fully erodible to a depth of 5 m below mean sea level. The basin has a 1:1000 slope, running from a depth of 5 m below mean sea level adjacent to the beach, to a depth of 10.5 m at a distance of 5.5 km from the beach. The basin itself is also erodible, with an initial sediment depth of 0 m adjacent to the beach, increasing linearly to an erodible depth of 20 m at a distance of 1 km from the beach. The initial erodible depth is 20 m at all points further offshore from this line. This configuration is adopted so as to maintain a smooth transition between the inerodible channel and erodible basin. Sediment transport is calculated using the Van Rijn (1993) equations (see Deltares, 2021a).

Table 4.2: Common Simulation Parameters: Grid Convergence Tests

Physical Parameters	Symbol	Value	Unit
Simulated time	T	96	yr
Discharge rate	Q_0	1280	$\mathrm{m^3\,s^{-1}}$
Susp. sed. concentration at inlet boundary	$\bar{c}_{in}$	0.1	$\mathrm{kg\,m^{-3}}$
Median grain size	D_{50}	0.225	mm
Numerical Parameters			
Time-step	Δt	9	s
Chézy friction factor	C	45	$\mathrm{m^{1/2}\,s^{-1}}$
Morphological acceleration factor	f_m	700	-
Max. dry cell erosion factor	Θ_{SD}	$1/3$	-
DCEF threshold depth	$H_{max,\Theta}$	1.5	m

4.1.2 Quantification of flow-grid alignment by analysis of fluid velocity vectors

The relative performance of each grid size is evaluated based upon analysis of velocity vectors throughout each simulation. This involves grouping cell-centre velocities throughout the simulation (i.e. in all cell-centres at all simulation write-times) by direction into 36 discrete bins at 10° intervals, summing the magnitudes of all velocities in each bin, then non-dimensionalising by dividing by a normalising factor. We define non-dimensionalised velocity per directional bin, $\bar{W}_\ell$ [-], as:

$$\bar{W}_\ell = \frac{|\bar{w}_\ell|}{\sum_{\ell=1}^{36} |\bar{w}_\ell|}, \tag{4.1}$$

where

$$\bar{w}_\ell = \sum_{i=1}^{I} \sum_{j=1}^{J} \sum_{k=1}^{K} |\bar{w}_{ij\ell}^{(k)}|$$

is the sum of all velocities at all locations and times in the ℓth directional bin [$\mathrm{m\,s^{-1}}$]; with $\bar{w}_{ij\ell}^{(k)}$ the depth-averaged velocity vector [$\mathrm{m\,s^{-1}}$] at the i by jth cell, at the kth output time, oriented along the ℓth directional bin (defined such that $\ell = 1$ represents velocity vectors with $\theta \leq 5°$ or $\theta > 355°$, $\ell = 2$ represents velocity vectors with $5° > \theta \leq 15°$, $\ell = 3$ represents velocity vectors with $15° > \theta \leq 25°$, and so until $\ell = 36$); I, J the total number of cells in the x- and y-directions respectively; and K the total number of times at which data were recorded. The non-dimensionalising factor (denominator in Eq. (4.1)) is the sum of all velocity magnitudes in all cell-centres at all simulation write times; hence, the sum of all normalised bins for each simulation is 1. Additionally, all normalised velocities in bins aligned with the principal axes—i.e. those at: $0° \pm 5°$; $90° \pm 5°$; $180° \pm 5°$; and $270° \pm 5°$—are summed to give a single number, p, indicative of the overall degree of flow-grid alignment per simulation.

Polar plots of normalised velocities for each simulation are shown in Figure 4.1. Figure 4.2 shows the degree of flow-grid alignment p for each simulation. Figure 4.3 shows the final bathymetries of each simulations at $t \approx 96$ yr. Grid-flow alignment is very pronounced in the 125 m and 250 m test cases, as represented by the large bars aligned with the major axes in Figures 4.1d and e, as well as the clearly grid-aligned channels and levees visible in Figure 4.3d and e. The simulations at $\Delta x = \Delta y = 12.5$ m, 25 m, and 50 m all produced morphologies free, under visual inspection, from the above noted grid-flow alignment (Figures 4.3a, b, and c), instead featuring channels with more 'natural' meanders and relatedly even distribution of flow vector directions in Figures 4.1a, b, and c. Inspection of Figure 4.2 suggests that there is a small increase in flow-grid alignment in the 50 m grid-size simulation as compared to the 25 m and 12.5 m grid-size simulations—$p \approx 0.17$ in the former case, compared to $p \approx 0.15$ in the latter cases—hence a

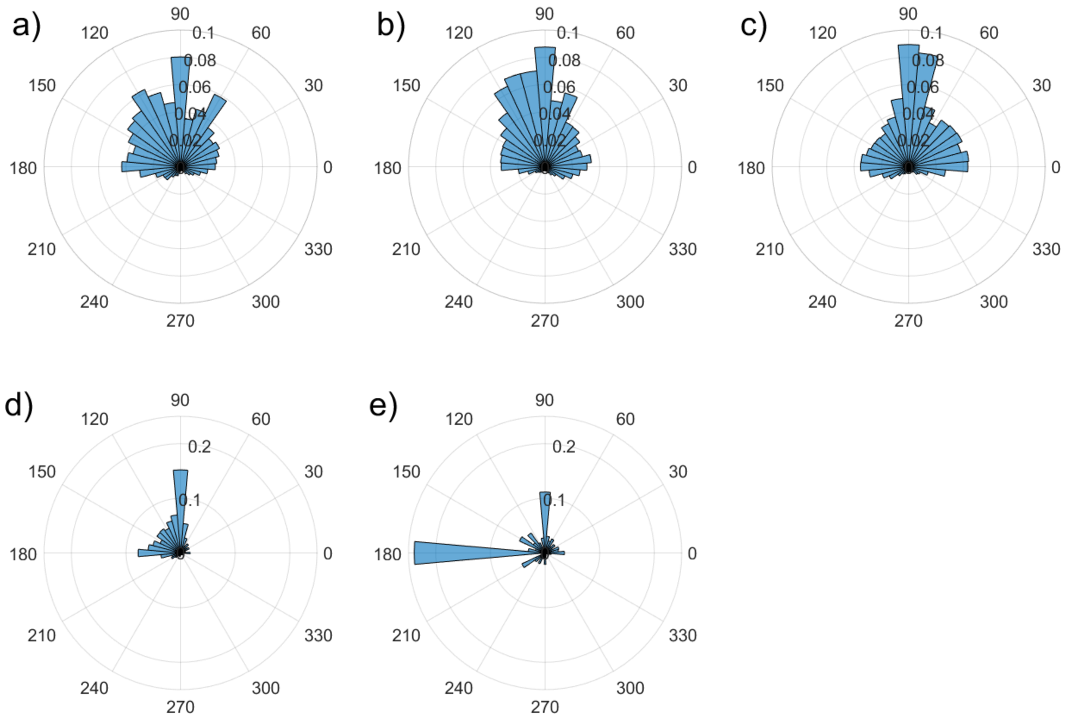

Figure 4.1: Polar plots of normalised net direction of flow in all convergence tests: $\Delta x = \Delta y =$ a) 12.5 m; b) 25 m; c) 50 m; d) 125 m; and e) 250 m. Note the varied radial axes.

grid spacing of $\Delta x = \Delta y = 25$ m is selected conservatively as the most appropriate choice for future simulations.

4.1.3 Concluding remarks

Following grid convergence testing, a value of $\Delta x = \Delta y = 25$ m was determined to be the most appropriate choice for further simulations. This determination was based primarily on the evidence of the degree of flow-grid alignment as quantified by Figure 4.2, and also so as to minimise the required computational expense, which would be significantly larger if choosing $\Delta x = \Delta y = 12.5$ m. Broadly, the tendency for velocity vectors to align with the grid is a result of "natural" channel

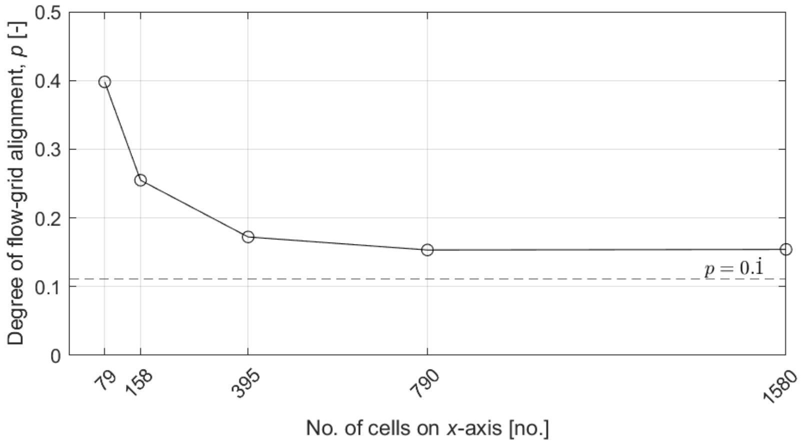

Figure 4.2: Flow-grid alignment number, p, for all grid convergence simulations. The black dashed line at $p = 0.\dot{1}$ is the value p would take if all velocity vectors were equal in magnitude and uniformly (directionally) distributed. Numbers shown on the x-axis are number of cells in the x-direction, corresponding to grid sizes of $\Delta x = \Delta y =$ 250 m, 125 m, 50 m, 25 m, and 12.5 m respectively from left to right.

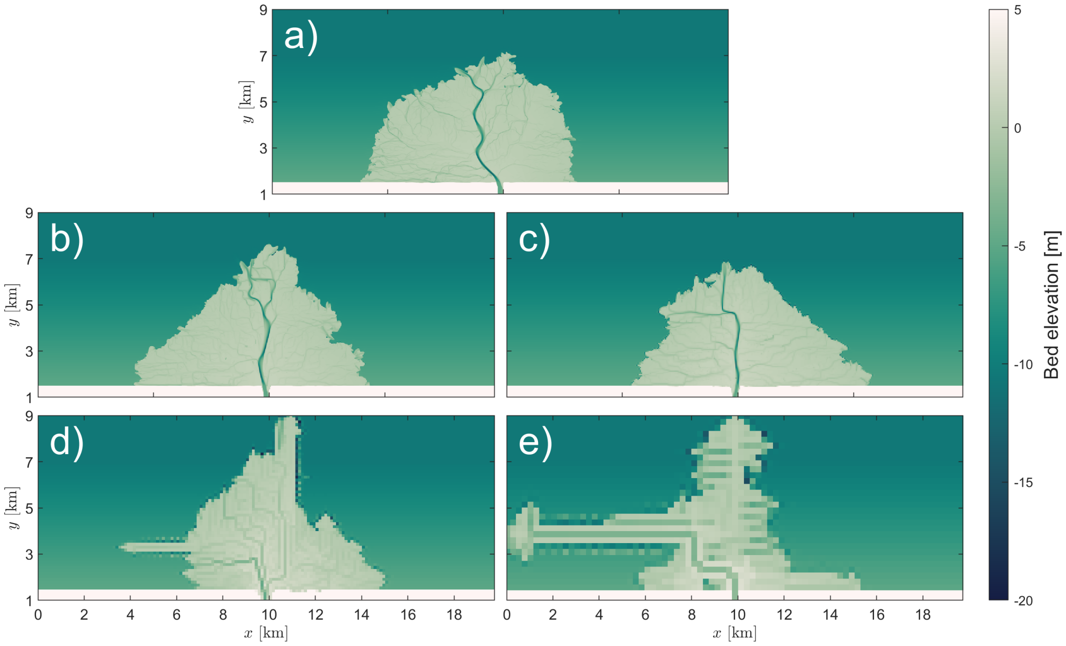

Figure 4.3: Bathymetry at $t \approx 96$ yr for convergence tests with: $\Delta x = \Delta y =$ a) 12.5 m; b) 25 m; c) 50 m; d) 125 m; and e) 250 m.

widths in a simulation falling close to that simulation's grid size, whereupon the grid resolution is no longer sufficient to allow for the simulation of accurate (lateral) development of such channels. This is analogous to the inability of hydrodynamic simulations to directly resolve turbulence at scales below grid size.

4.2 Comparison of direct specification and HLES approaches for determining horizontal eddy viscosity and diffusivity

§3.1 introduced the parameters of horizontal diffusion of momentum, ν_H, and horizontal diffusion of sediment, ϵ_H. These parameters allow for the determination of diffusion of their respective quantities as a result of turbulence occurring at spatial and temporal scales too small to be resolved directly by the discretised model. Delft3D provides two approaches to defining these parameters: either by direct specification (which may be uniform or spatially varied); or by application of the sub-grid scale (SGS) turbulence model described in §3.1.3 (horizontal large eddy simulation (HLES) approach). Several prior studies on delta and mouth bar development using Delft3D have used the SGS turbulence model to determine horizontal eddy viscosity and diffusivity (e.g. Burpee et al., 2015; Caldwell and Edmonds, 2014; Canestrelli et al., 2014; Edmonds and Slingerland, 2010; Gao et al., 2018; Leonardi et al., 2013; Lera et al., 2019; Mariotti et al., 2013; Nardin and Fagherazzi, 2012; Nardin et al., 2013; Nardin and Edmonds, 2014; Nardin et al., 2016; Tejedor et al., 2016), although some have instead implemented direct (and uniform) specification (e.g. Angamuthu et al., 2018; Baar et al., 2019; Iwantoro et al., 2020; Zhou et al., 2020). This section outlines initial sensitivity testing of both approaches, applied to simulations free from waves and tides. §4.2.1 outlines testing of the direct specification approach. §4.2.2 outlines testing of the HLES / SGS approach.

4.2.1 Model setup

All simulations were run with identical setup, other than parameters relating to determination of ν_H and ϵ_H. Common model parameters are given in Table 4.3. The test domain comprises a 10 km alongshore by 10 km cross-shore basin, into which a 150 km long, 250 m wide river with slope 1:10000 discharges. Sediment concentration at the inflow is determined using an 'equilibrium' condition, wherein the concentration at the boundary is set equal to the equilibrium concentration c_{eq} calculated in the first cell adjacent to that boundary (see §3.1.2.1). All simulations are modelled without waves or tides. Lateral basin boundaries are represented by a Neumann-type boundary defining a flat water level gradient in the alongshore direction—i.e. $\partial\zeta/\partial x = 0$ m m^{-1}. The offshore boundary is defined using a constant Riemann type boundary $R^{+}_{D3D} = 0$ m s^{-1}. Each simulation represents approximately 19 yr of morphological development.

A 500 m wide beach with slope 1:25 is included adjacent to the onshore boundary, ranging from 15 m above MSL down to 5 m below MSL. (Note that this early test setup differs from the approach used elsewhere in this thesis. A sloped beach was omitted from later tests to avoid spurious results related to cyclic flooding and drying of beach cells.) The basin has a 1:500 slope, running from a depth of 5 m below MSL adjacent to the beach, to a depth of 24 m at the offshore boundary.

Table 4.3: Common Simulation Parameters: Horizontal Eddy Viscosity and Diffusivity Tests

Physical Parameters	Symbol	Value	Unit
Simulated time	T	19	yr
Discharge rate	Q_0	1280	$\mathrm{m}^3\,\mathrm{s}^{-1}$
Median grain size	D_{50}	0.225	mm
Numerical Parameters			
Time-step	Δt	9	s
Grid spacing	Δx, Δy	25	m
Chézy friction factor	C	45	$\mathrm{m}^{1/2}\,\mathrm{s}^{-1}$
Morphological acceleration factor	f_m	350	-
Dry cell erosion factor	Θ	0	-

Additionally, random bed elevation perturbations with a uniform distribution from 0 m to -0.05 m are applied throughout the basin. The entire domain is erodible, with an initial sediment depth of 20 m throughout. Sediment transport is calculated using the Van Rijn (1993) equations (see Deltares, 2021a).

4.2.1.1 Setup of SGS turbulence model

For the SGS model, a range of parameters need to be defined. Most of these parameters are defined based on aspects of the model setup, as described below, and are summarised in Table 4.4. See §3.1.3 and Eqs. (3.12) to (3.19) for description of the SGS model and equations using these parameters. The spectral energy density slope $\alpha = 5/3$ describes the (negative) gradient of the log-log plot of spectral turbulent energy $E(k)$ [$\mathrm{J\,kg^{-1}\,Hz^{-1}}$] with respect to turbulent wave number k [m^{-1}], and quantifies the transfer of energy from larger to smaller vortices—i.e. $E \propto k^{-5/3}$. The assigned value $-5/3$ follows the foundational work of Richardson (2007) and Kolmogorov (1991), the full explanation of which is beyond the scope

Table 4.4: Common Parameters Used in SGS Turbulence Model

Parameter	Symbol	Value	Unit
Spectral energy density slope	α	$5/3$	-
Dimensional number	n_D	2.0	-
Spatial low-pass filter coefficient	f_{lp}	$1/3$	-
Turbulent Schmidt number	σ_T	0.7	-

of this thesis (for further detail, see e.g. Pope, 2000). Furthermore, we note that α is generally set to either 3 or $5/3$, and that the effect of this choice on calculated values of ν_{sgs} is small (Kernkamp and Uittenbogaard, 2001); hence, we do not test this parameter here. The factor n_D is equal to the number of dimensions modelled (e.g. $n_D = 2$ for a 2DH model). The selected value for the spatial low pass filter coefficient $f_{lp} = 1/3$ follows the observation by Uittenbogaard and Vossen (2004) that values of $f_{lp} \approx 0.3$ are appropriate for square grids. Previous investigations concerning the determination of σ_T have largely found values in the approximate range 0.5–1.0 (which is also the range recommended by Uittenbogaard and Vossen, 2004), with values close to around 0.7 being common in sediment-transporting environmental flows (Gualtieri et al., 2017). A value of $\sigma_T = 0.7$ is therefore adopted for all SGS model simulations. Only the relaxation time τ (see Eq. (3.19) and associated definitions) remains to be defined, where τ is a calibration parameter related to the expected scale of turbulence in a simulation; this parameter is the subject of the sensitivity testing presented in §4.2.3.

4.2.2 Sensitivity testing of direct specification approach

Testing of the direct specification approach was undertaken with the combinations of ν_H and ϵ_H shown in Table 4.5. These values were selected to cover the range

Table 4.5: runIDs and Associated Values of ν_H, ϵ_H, and σ_T used in Direct Specification Sensitivity Tests.

runID	ν_H [m^2 s^{-1}]	ϵ_H [m^2 s^{-1}]	σ_T [-]
V0D0	0.001	0.001	1
V1D1	1	1	1
V1D10	1	10	0.1
V10D1	10	1	10
V10D10	10	10	1
V2.5D25	2.5	25	0.1
V10D100	10	100	0.1

recommended by Deltares (2021a) for grid sizes similar to that chosen for the simulations in this thesis, and to also cover a broad range of σ_T values between 0.1 and 10. Previous studies using the direct specification approach have typically specified either 1 m^2 s^{-1} or 10 m^2 s^{-1} for ν_H and ϵ_H for grid sizes typically of $\mathcal{O}\,(10\text{ m})$ (e.g. Baar et al., 2019; Iwantoro et al., 2020; Zhou et al., 2020). Some of these studies in fact apply the Delft3D default values of $\nu_H = 1.0$ m^2 s^{-1} and $\epsilon_H = 10$ m^2 s^{-1}, giving a turbulent Schmidt number $\sigma_T = 0.1$. This value lies at the lowest extreme of the ranges found in previous numerical and experimental studies on sediment-transporting environmental flows (Gualtieri et al., 2017).

Bed levels after 19 simulated years of morphodynamic development for the simulations outlined in Table 4.5 are shown in Figure 4.4. Different combinations of ν_H and ϵ_H lead to notably varied morphologies, as seen in Figure 4.4. This is most evident in patterns of sediment deposition at the outer edge of each delta; large, even lobes form under higher values of ν_H (Figures 4.4d, e, and g), as compared to those with smaller values of ν_H (e.g. Figures 4.4b and c). Simulations with $\sigma_T = 0.1$ and $\nu_H \leq 1$ m^2 s^{-1} establish elongated levees at the ends of discharging channels (Figures 4.4c and f). This result is expected, as low ν_H leads to slower diffusion of momentum and hence relatively fast and narrow discharging jets, while relatively high ϵ_H causes suspended sediments to diffuse laterally from within these jets into the slower surrounding water, where they are then deposited to form levees. While simulation V10D100 (Figure 4.4g) also has turbulent Schmidt number $\sigma_T = 0.1$, the comparatively greater horizontal eddy viscosity $\nu_H = 10$ m^2 s^{-1} (in comparison to V1D10 and V2.5D25) leads to a significantly wider jet and hence less clear evidence of levee growth. For this simulation, delta margins are smoother than those of V1D10 and V2.5D25, but sediment is not distributed as evenly throughout the margins as in V10D1 or V10D10.

In each simulation with $\nu_H = 10$ m^2 s^{-1} (V10D1, V10D10, and V10D100—Figures 4.4d, e, and g respectively), only one or two deep channels exist at the time shown, and these channels are visibly wider than those in simulations with lower values of ν_H. This suggests that increases to ν_H lead to the formation of fewer, wider channels. This is particularly evident in comparison of these simulations to the baseline simulation V0D0 (Figure 4.4a).

4.2.3 Sensitivity testing of HLES / SGS approach

Sensitivity testing of the HLES / SGS approach focuses on variation of the relaxation time, τ (see §3.1.3). In general, Deltares (2021a) recommends that τ should be greater than the largest expected timescale of eddies, τ_e [s]. While Deltares (2021a) offer no definition of eddy timescale, we interpret it to be as represented in textbooks (e.g. Tennekes and Lumley, 1972; Pope, 2000), as the ratio of a characteristic length scale to a characteristic velocity scale. That is:

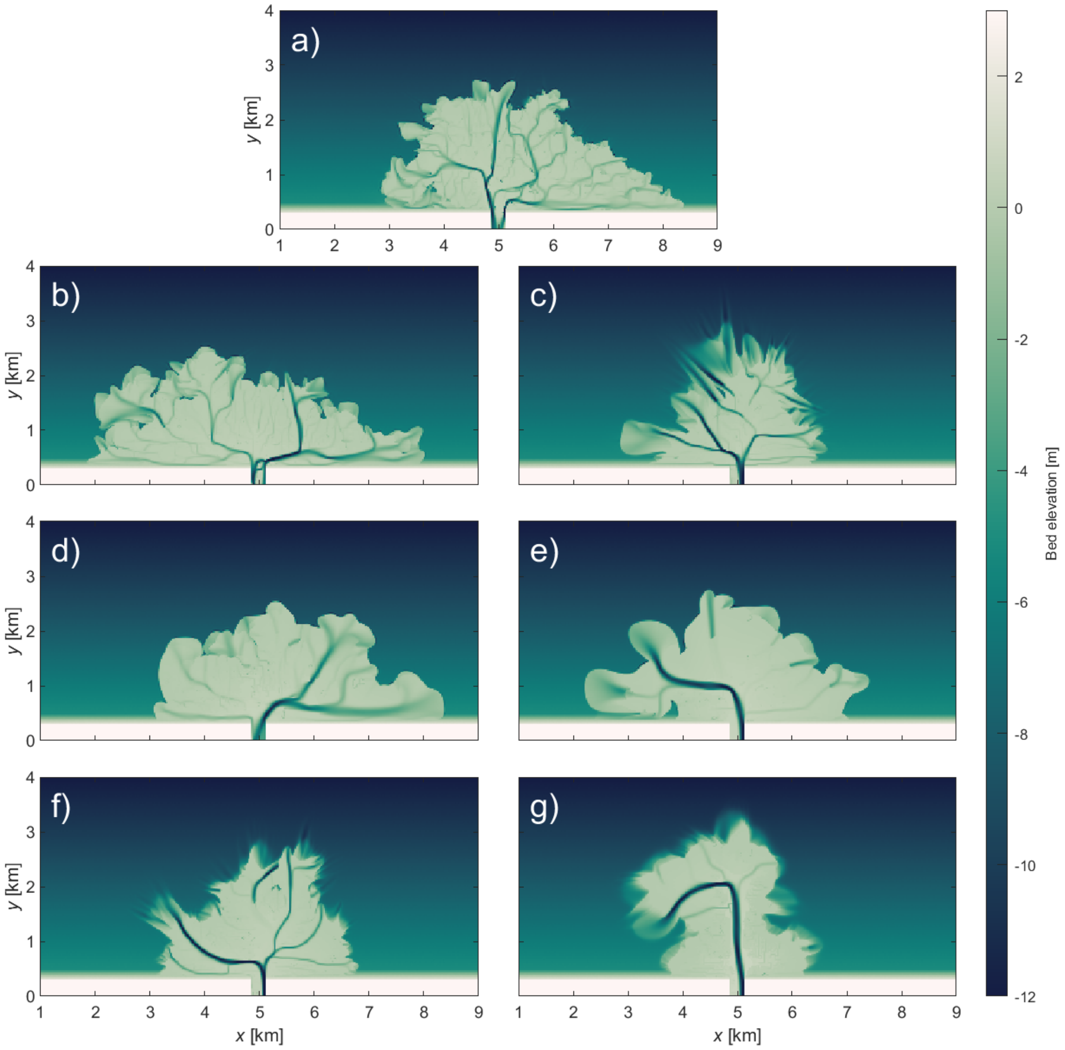

Figure 4.4: Bed elevations after 19 yr for direct specification viscosity and diffusivity sensitivity tests. Sub-figures show: a) V0D0; b) V1D1; c) V1D10; d) V10D1; e) V10D10; f) V2.5D25; and g) V10D100.

$\tau_e = \ell_e/u_e$, where ℓ_e is the characteristic eddy length scale, representing the approximate diameter of the eddy [m]; and u_e is the characteristic velocity scale, representing the approximate speed of fluid rotating around the circumference of the eddy [m s^{-1}]. Estimation of the expected largest value of τ_e is challenging for a dynamic delta model, due to the evolving hydro- and morphodynamic conditions. As an estimation of the possible maximum τ_e, an analysis based upon expected jet stability and associated vortex shedding of the initial river mouth was conducted, based on the methodology of Mariotti et al. (2013) and Canestrelli et al. (2014). An explanation of the methods used in this stability analysis are presented as Appendix B. This analysis suggested a potential largest eddy timescale $\tau_e \approx 39$ min for the bathymetry described in §5.1.2 and largest tidal range $H_t = 6$ m used in later testing. However, it should be noted that this timescale is associated with an unstable vortex-shedding mode that is uncertain to occur for the conditions considered, and that the largest eddies occurring would likely be much smaller if this unstable vortex-shedding mode is indeed not present.

Turning our attention to prior studies, these typically do not state values of τ used, despite the HLES / SGS approach being commonly adopted. Model setup files provided by Edmonds (personal communication) reveal that they set $\tau = 1$ min in the delta-modelling simulations presented in Edmonds and Slingerland (2010). This value of $\tau = 1$ min was also used by Mariotti et al. (2013), albeit for smaller scale modelling of mouth-bar development.

Based on the above analysis and evidence of values used in prior studies, a range of τ values of 0.1, 1, 10, and 100 min was chosen for testing. Bed levels after 19 simulated years of morphodynamic development for these simulations are shown in

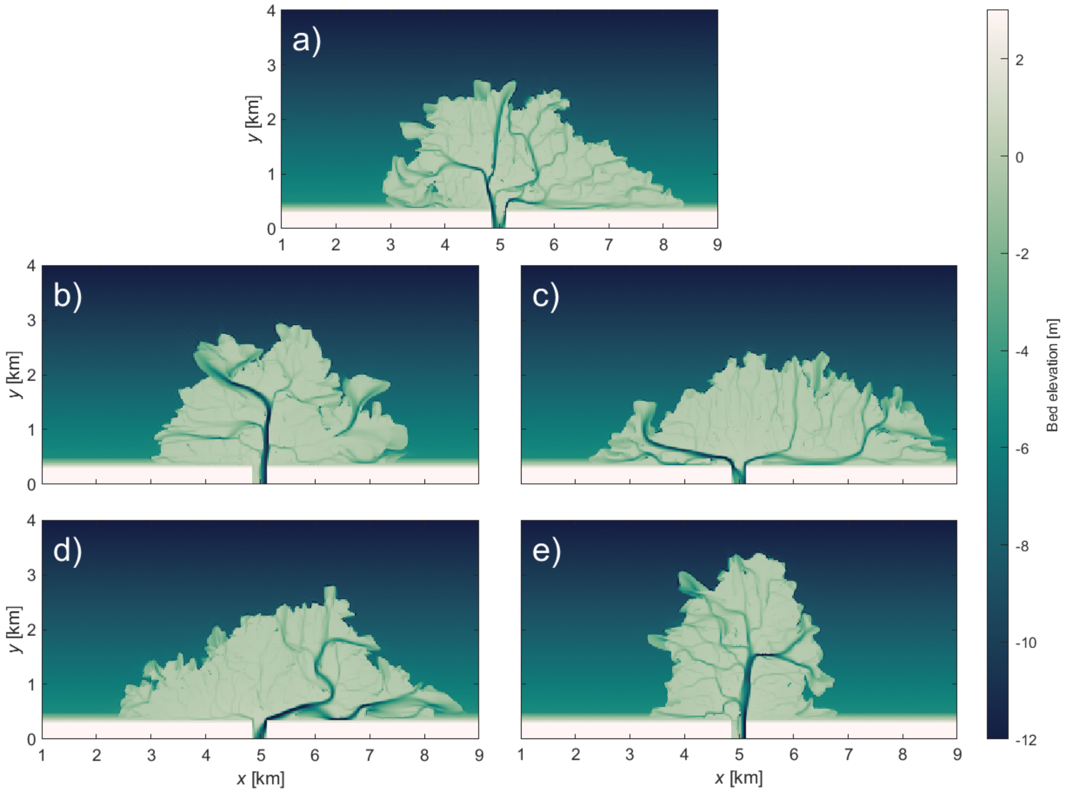

Figure 4.5: Bed elevations after 19 yr for SGS model viscosity and diffusivity tests. Sub-figures show simulations with: a) SGS model disabled (simulation V0D0); b) $\tau = 0.1$ min; c) $\tau = 1$ min; d) $\tau = 10$ min; and e) $\tau = 100$ min.

Figure 4.5, alongside a reference simulation with the SGS model disabled.

The simulations presented in Figure 4.5 produce notably different bathymetries. The is because the mechanics of delta formational processes (here, mouth-bar induced bifurcation and avulsion) are such that even small changes in model parameters are likely to lead to very different realisations of deltas. However, characteristic delta features such as channel width / depth, and shoreline roughness do not exhibit the same degree of variation as seen in Figure 4.4. Slight differences in channel numbers and widths are visible, but it should be noted all simulations shown fluctuate between periods of having lower numbers of wider channels, and a greater number of narrower channels. This is a consequence of frequent avulsions and related periods of overland flow occurring when tidal water level variation is not present (see §7.1 for further discussion of this process). It is unsurprising that sensitivity testing of τ produces deltas exhibiting less variability than seen under sensitivity testing under direct specification of ν_H and ϵ_H; even at the longest relaxation time modelled ($\tau = 100$ min), values of ν_H and ϵ_H determined using the SGS model are generally < 1 m^2 s^{-1} throughout the domain, with peak values of $\mathcal{O}\left(1 \text{ m}^2 \text{ s}^{-1}\right)$ occurring only at river bends or close to discharging jets of the channels. This implies only moderate diffusion of both momentum and sediment within these locations (in comparison to the direct specification tests), with very little diffusion occurring elsewhere.

4.2.4 Concluding remarks

The tests presented in this section illustrate that the morphological development of simulated river deltas is highly sensitive to selection of ν_H and ϵ_H. The effects of varying these parameters on delta morphodynamics are clear from Figure 4.4. While illuminating within the context of sensitivity testing, the pairing of values of ν_H and ϵ_H giving extreme σ_T values of 0.1 and 10 is only included here so as to clearly highlight the comparative effects of these parameters; these simulations should not be considered representative of real flows, given that such values of σ_T are not generally observed in the environment (Gualtieri et al., 2017). By comparison, application of the SGS turbulence model produced values of ν_H and ϵ_H significantly smaller than those tested under the direct specification approach, leading to greater morphological similarity in the SGS model simulations in comparison to the direct specification simulations. It is worth highlighting that several studies have in fact modelled flows with (implicit) values of $\sigma_T = 0.1$, by using (Delft3D default) values of $\nu_H = 1$ m^2 s^{-1} and $\epsilon_H = 10$ m^2 s^{-1} (e.g. Angamuthu et al., 2018; Baar et al., 2019; Zhou et al., 2020). Based on the evidence of both existing literature on the topic, and the results of simulations presented here, it seems plausible that such studies have overlooked the importance of these parameters.

The long-term morphological development of a delta, particularly under tidal variation, would be expected to produce large variation in turbulence both spatially and temporally. Based on this observation—and on the potential greatest eddy timescale predicted by the analysis shown in Figure B.1—application of the SGS model with a relaxation time $\tau = 50$ min is considered here to be better able to represent this variation in comparison to the direct (uniform) specification method; this is due to its ability to represent the dynamically varying turbulence expected at the large spatial and temporal scales modelled.

4.3 Comparison of the Van Rijn (1993) and Soulsby / Van Rijn transport formulae with coupled WAVE and FLOW

Delft3D offers fourteen different sets of formulae for calculating sediment transport (see Deltares, 2021a). By default, the Van Rijn (1993) (VR93) equations are used, and several previous studies on delta modelling have used these formulae (e.g. Edmonds and Slingerland, 2010; Caldwell and Edmonds, 2014; Burpee et al., 2015; Gao et al., 2019; Liu et al., 2020). However, initial testing of the coupling of WAVE and FLOW resulted in physically unrealistic morphological development when using the VR93 formulae with default parameters. Most notably, this was seen in the development of regions of excessive erosion adjacent to the shoreline, when modelling waves with significant wave height $H_s = 1.0$ m.

Of the fourteen sets of formulae available in Delft3D, only some are appropriate for modelling transport of sands in a tidal coastal model featuring (breaking) waves. Among these, the SVR formulae (see §3.1.2.1 and Deltares, 2021a) are well established, relatively simple, and capable of modelling distinct bedload and suspended load fluxes under both currents and waves, applicable to conditions under which sediments form rippled beds. They have been used in at least one recent delta modelling study presenting simulations similar to those in this thesis (Broaddus et al., 2022). Here we compare results for simulations using the commonly used VR93 formulae (see Deltares, 2021a) to ones using SVR. Initial testing involves modelling of a schematised beach profile (based on Calvete et al., 2005), for which calculated wave- and current-driven fluxes are compared for both formulae. A subsequent set of tests investigate morphodynamic development within a (potentially) delta-forming coast and river system. This includes one test using VR93, and one using SVR. Both of these simulations model waves with $H_s = 1.0$ m, alongside tides with range $H_t = 1.0$ m and period $T_t = 12.5$ hr. These tests illustrate the differences in calculated sediment fluxes arising from the differing processes considered and assumptions underpinning these two sets of formulae.

4.3.1 Key differences between VR93 and SVR

The VR93 and SVR formulae have some important differences, most notably related to the magnitudes and directions of wave-driven fluxes. Both sets of formulae calculate a sediment sink / source term S (see Eq. (3.8)), based upon both current and wave variables, which is used to determine rates of erosion / deposition. Both methods also calculate wave-and-current-driven bedload fluxes, but make different assumptions about the direction of bedload flux. SVR calculates $q_{b,x}$ and $q_{b,y}$ along the x and y axes independently—see Eqs. (3.5) and (3.6)—such that bedload fluxes are implicitly oriented in the same direction as the (Eulerian) velocities. By contrast, VR93 first calculates a total magnitude of bedload flux, $|q_b|$, and then subdivides this flux into distinct current-driven and wave-driven components q_{bw} and q_{bc}, which are assumed to act, respectively, in the direction of the (Eulerian) velocity vector and the mean wave direction. Furthermore, VR93 calculates additional (near-bed) suspended sediment fluxes due specifically to wave *asymmetry*, $q_{sw,x}$ and $q_{sw,y}$ (an effect not accounted for by SVR). These fluxes are also assumed to act in the mean wave direction. (Note that these additional wave-asymmetry-driven near-bed suspended fluxes, $q_{sw,x}$ and $q_{sw,y}$, are included within the *bedload* flux components $q_{b,x}$ and $q_{b,y}$ of the Delft3D model output.) A final notable difference is that SVR attenuates calculated wave-driven fluxes in shallow water by limiting calculated root-mean-square orbital velocity u_{rms} (used in Eqs. (3.5) to (3.7)) using a criterion based upon instantaneous water depth h (see Deltares, 2021a). No such limitation is employed by VR93.

4.3.2 Testing of coupled FLOW and WAVE using SVR and VR93 to calculate sediment fluxes on a beach with offshore bar

With the above-noted differences between VR93 and SVR in mind, these tests were designed to investigate how magnitudes and directions of calculated sediment fluxes differ between each set of formulae.

4.3.2.1 Model setup

Three simulations were run, each using the same domain and bathymetry, with calculation of sediment fluxes enabled but changes to bed elevations disabled. The first simulation uses SVR, and the second uses VR93 with default parameters (simulation VR93a). A third simulation (VR93b) also uses VR93, but has calculation of suspended fluxes due to wave asymmetry, $q_{sw,x}$ and $q_{sw,y}$, disabled. This allows a distinction to be made between general bedload flux and wave-asymmetry-driven flux under VR93.

Common model parameters are given in Table 4.6. A domain with dimensions 0.3 km cross-shore (x-direction) × 10.0 km alongshore (y-direction) is used, with grid spacings $\Delta x = 5$ m and $\Delta y = 100$ m. The same spatial grid is used for both FLOW and WAVE. Additionally, two further grids are defined in WAVE: a frequency grid comprising 24 logarithmically spaced bins between 0.05 Hz and 0.5 Hz; and a directional grid comprising 72 bins at 5° intervals. The FLOW domain uses a constant Dirichlet water level boundary offshore with water level $\zeta = 0$ m (MSL), and Neumann boundary conditions describing water level gradients $\partial\zeta/\partial y = 0$ m m^{-1} at the lateral boundaries. Waves are generated at the offshore WAVE boundary using the parameters given in Table 4.6 (see Deltares, 2021b).

Table 4.6: Common Simulation Parameters: Coupled FLOW and WAVE Beach with Barrier Tests

Physical Parameters	Symbol	Value	Unit
Simulated time	T	24	hr
Median grain size	D_{50}	0.2	mm
Significant wave height	H_s	1	m
Mean wave frequency	f	0.166	Hz
Wave frequency standard deviation	σ_f	0.01	Hz
Wave approach angle	θ	3.33	°
Wave angle standard deviation	σ_θ	5	°
Numerical Parameters			
Time-step	Δt	9	s
Grid spacing, x-axis	Δx, Δx_w	5	m
Grid spacing, y-axis	Δy, Δy_w	100	m
FLOW–WAVE coupling period	-	180	min
Chézy friction factor	C	65	$\mathrm{m}^{1/2}\,\mathrm{s}^{-1}$

The cross-shore profile, representing a beach with offshore bar, is as described by Calvete et al. (2005), wherein:

$$z\left(x\right) = a_1 \left(1 - \frac{\beta_2}{\beta_1}\right) \tanh\left(\frac{\beta_1 x}{a_1}\right) + \beta_2 x - A_b \exp\left[-W_b \left(\frac{x - X_b}{X_b}\right)^2\right] \quad (4.2)$$

where a_1 is a calibration constant [m]; β_1 is shoreline slope [m m^{-1}]; β_2 is offshore slope [m m^{-1}]; A_b is the “amplitude” of the offshore bar [m]; W_b is the width of the offshore bar [m]; and X_b is the offshore location of the bar crest [m]. Eq. (4.2) is used to define the cross-shore profile, with: $a_1 = 2.97$ m; $\beta_1 = 0.075$, $\beta_2 = 0.0064$, $X_b = 80$ m; $A_b = 1.5$ m, and $W_b = 5$ m. This profile can be seen in Figure 4.6a. The profile is uniform in the alongshore direction. Each simulation is run from a cold start for $T = 24$ hr of simulated time, allowing for an equilibrium condition to be reached. Data are recorded at the end of each simulation.

4.3.2.2 Results and discussion

Figure 4.6 shows the cross-shore bed elevation profile, as well as cross-shore and alongshore suspended and bedload sediment fluxes through a transect at $y = 50.5$ km for all three simulations. It is clear from Figure 4.6b that inclusion of cross-shore sediment flux due to wave-asymmetry, $q_{sw,x}$, in simulation VR93a (red circles) leads to significantly larger shoreward-oriented transport of sediments, in comparison to simulation VR93b. Also evident in Figure 4.6b is the difference in both magnitude and direction of bedload fluxes $q_{b,x}$ between SVR (red crosses) and VR93b (red triangles), with values calculated in simulations VR93b being roughly an order of magnitude greater than those calculated using SVR, and oriented onshore rather than offshore. These differences have clear implications for the expected development of morphodynamic simulations under each approach.

Differences in alongshore transports (Figure 4.6c) are less pronounced, although suspended fluxes $q_{s,y}$ under SVR are generally somewhat larger than those under both VR93 simulations. This is true throughout, except in regions where depth $h < 1.5$ m, wherein values of $q_{s,y}$ calculated by VR93 are larger (this is also evident in $q_{s,x}$ values in Figure 4.6b). This difference is a consequence of the noted attenuation of calculated transports in shallower regions imposed by SVR. A further notable difference can be seen in the alongshore bedload fluxes $q_{b,y}$ which are larger under SVR than VR93, contrary to the cross-shore bedload fluxes $q_{b,x}$. This is due to the direction of bedload flux under VR93 being predominantly oriented in the mean wave direction, rather than that of the Eulerian velocities as with SVR (where alongshore currents are here a consequence of wave energy dissipation).

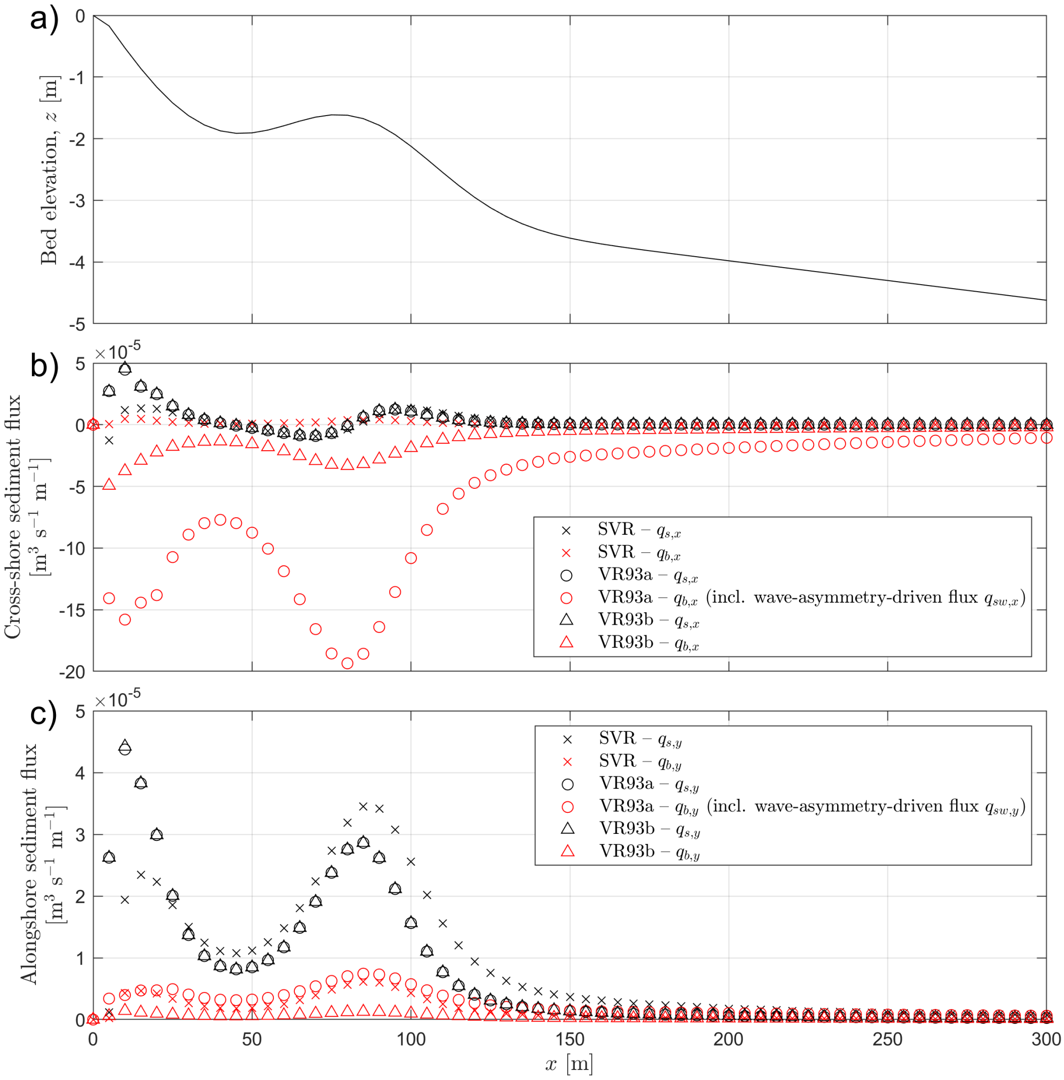

Figure 4.6: a) Cross-shore bed elevation profile, calculated using Eq. (4.2); b) cross-shore sediment fluxes (positive values denote left-to-right fluxes); and c) alongshore sediment fluxes (positive values denote bottom-to-top fluxes).

4.3.3 Testing of SVR and VR93 within coupled WAVE and FLOW for delta-modelling

The tests in this subsection are designed to test the SVR and VR93 formulae when applied to the morphodynamic modelling of delta development using coupled WAVE and FLOW.

4.3.3.1 Model setup

Two simulations are presented: one using the SVR formulae, and one using VR93. Common model parameters are given in Table 4.7. The test domain comprises a 19.75 km alongshore by 9.00 km cross-shore basin, into which a 50.5 km long, 250 m wide river with slope 1:5000 discharges. The basin has a 1:1000 slope, running from a depth of 5 m below mean sea level adjacent to the beach, to a depth of 11.5 m at a distance of 6.5 km from the beach, beyond which this depth is maintained. Additionally, random bed elevation perturbations with a uniform distribution from 0 m to -0.05 m are applied throughout the basin. A 500 m wide beach is included adjacent to the onshore boundary. The beach is fully erodible to a depth of 5 m below mean sea level. The basin is also erodible, with an initial sediment depth of 0 m adjacent to the beach, increasing linearly to an erodible depth of 20 m at a distance of 1 km from the beach. The initial erodible depth is 20 m at all points further offshore from this line. This configuration is adopted so as to maintain a smooth transition between the inerodible channel and erodible basin. The FLOW domain grid is nested inside a larger WAVE grid, which extends an additional 10.0 km to either direction alongshore and an additional 1.0 km offshore, as shown in Figure 4.7. Additionally, two further grids are defined

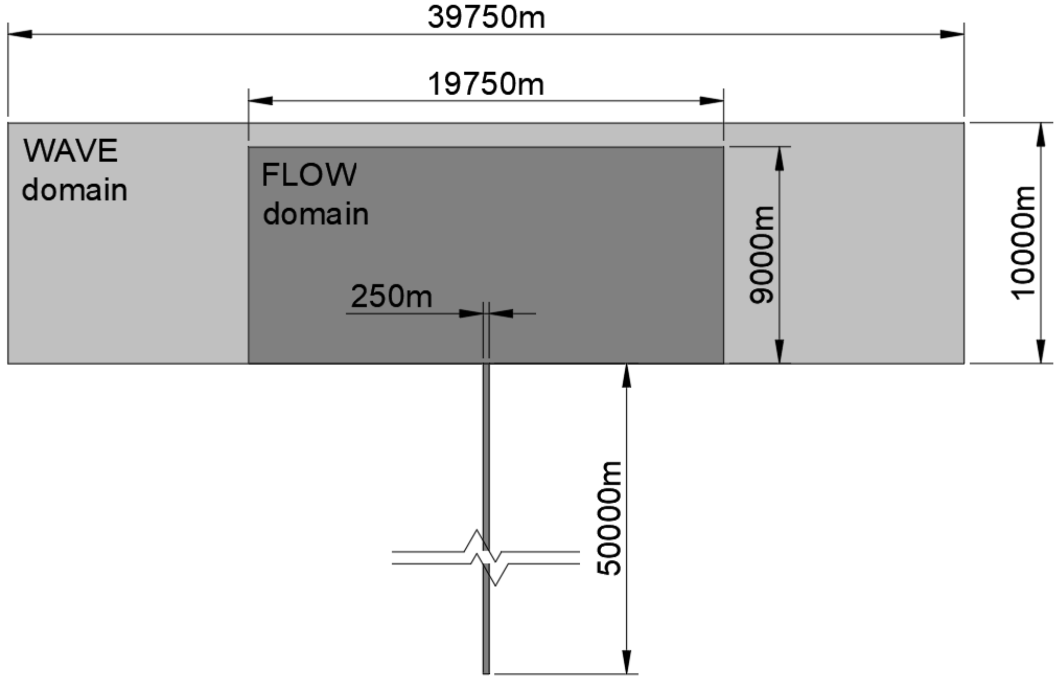

Figure 4.7: Sketch of FLOW and WAVE domains.

in WAVE: a frequency grid comprising 24 logarithmically spaced bins between 0.05 Hz and 1.0 Hz; and a directional grid comprising 72 bins at 5° intervals. Lateral basin boundaries are represented by a Neumann-type boundary defining a flat water level gradient in the alongshore direction—i.e. $\partial\zeta/\partial x = 0$ m m^{-1}. The offshore FLOW boundary is defined as a harmonically varying Riemann type boundary $R^+_{D3D}(t) = -0.4613 \sin(2\pi t/T_t)$ m s^{-1}. Waves are generated at the offshore WAVE boundary using a JONSWAP spectrum with parameters as shown in Table 4.7.

4.3.3.2 Results and discussion

Figure 4.8 shows bathymetry at $t \approx 24$ yr for both simulations. The SVR simulation (Figure 4.8a) produces a morphology featuring multiple lobes and channels

Table 4.7: Common Simulation Parameters: Coupled FLOW and WAVE Delta Morphodynamics Tests

Physical Parameters	Symbol	Value	Unit
Simulated time	T	24	yr
Discharge rate	Q_0	1280	$\mathrm{m^3\,s^{-1}}$
Susp. sed. concentration at inlet boundary	$\bar{c}_{in}$	0.1	$\mathrm{kg\,m^{-3}}$
Median grain size	D_{50}	0.125	mm
Significant wave height	H_s	1	m
Peak wave period	T_p	5	s
JONSWAP peak enhancement factor	γ_0	3.3	-
Wave approach angle	θ	0	°
Wave directional spread	-	$\cos^{50}$	-
Numerical Parameters			
Time-step	Δt	9	s
Grid spacing, FLOW	Δx, Δy	25	m
Grid spacing, WAVE	Δx_w, Δy_w	50	m
FLOW–WAVE coupling period	-	30	min
Chézy friction factor	C	45	$\mathrm{m^{1/2}\,s^{-1}}$
Morphological acceleration factor	f_m	175	-
Max. dry cell erosion factor	Θ_{SD}	1/3	-
DCEF threshold depth	$H_{max,\Theta}$	1.5	m

by which deltas are often characterised. In several locations, the development of nascent spits can be observed; features which are associated with real deltas under the influence of waves (Galloway, 1975; Orton and Reading, 1993; Anthony, 2015). Conversely, the VR93 simulation (Figure 4.8b) is marked by the development of wide levees flanking a central channel which continually grows in the positive y-direction throughout the simulation. This development is a consequence of the large, onshore-oriented wave-driven fluxes under VR93, as discussed in §4.3.2, whereby sediments delivered by the river are rapidly transported shoreward to grow the observed levees. Also visible in the VR93 simulation are regions of excessive erosion adjacent to these levees, where sediment has been eroded down to the inerodible basement layer of the model at depths of up to 20 m. The precise combination of factors leading to this erosion is difficult to discern, but it is likely in part related to the significantly larger wave-driven bedload fluxes calculated by VR93 in comparison to SVR. (Notably, the same phenomenon can be seen in Gao et al., 2019, in which coupled WAVE and FLOW modelling of delta development using VR93 was also conducted – see Figure 3, simulations W3 and B04W3.) Overall, the SVR simulation represents the processes expected for deltaic development under the influence of moderate waves (Galloway, 1975; Orton and Reading, 1993; Anthony, 2015), whereas VR93 exhibits development not representative of real deltas, while also producing physically unrealistic levels of erosion.

4.3.4 Concluding remarks

The tests presented in this section demonstrate the key differences between the SVR and VR93 formulae, which are primarily related to the direction and mag-

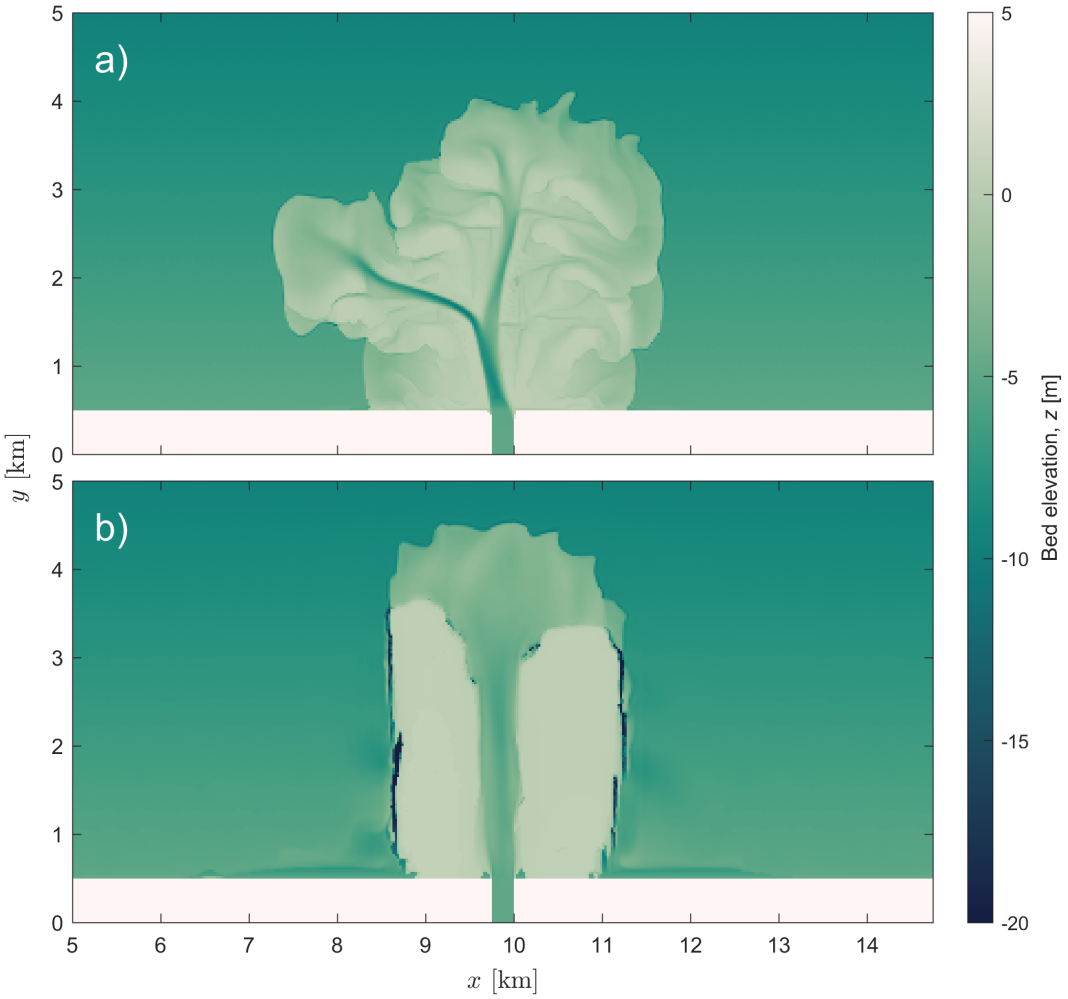

Figure 4.8: Bed elevations at $t \approx 24$ yr for simulations using: a) SVR; and b) VR93.

nitude of wave-driven sediment fluxes. Testing on a morphodynamic river and basin simulation suggest that SVR is better able to produce the expected features of river deltas (i.e. spits, deltaic lobes, and channel networks) under the conditions modelled (Galloway, 1975; Orton and Reading, 1993; Anthony, 2015). As such, SVR is used for all subsequent delta modelling simulations presented in this thesis.

4.4 Calibration of wave directional spread in Delft3D-WAVE

The initial intention for simulations investigating the inhibiting effects of wave and tides on delta development was to model (shore-normal) unidirectional waves. However, Delft3D-WAVE is in fact unable to model unidirectional waves, instead requiring waves to have some degree of directional distribution defined at the boundaries. Here, we present the results of three different simulations designed to test whether narrowing wave spread converges on a wave field such as would be expected for unidirectional waves.

4.4.1 Model setup

Three coupled WAVE and FLOW simulations were run in a river and basin system, with sediment transport calculations disabled. Common model parameters are given in Table 4.8. The test domain comprises a 19.75 km alongshore by 9.00 km cross-shore basin, into which a 50.5 km long, 250 m wide river with slope 1:5000 discharges. The basin has a 1:1000 slope, running from a depth of 5 m below mean sea level adjacent to the beach, to a depth of 11.5 m at a distance of 6.5 km from the beach, beyond which this depth is maintained. Additionally, random bed elevation perturbations with a uniform distribution from 0 m to -0.05 m are applied throughout the basin. A 500 m wide beach is included adjacent to the onshore boundary. The FLOW domain grid is nested inside a larger WAVE grid, which extends an additional 10.0 km to either direction alongshore and an additional 1.0 km offshore. Additionally, two further grids are defined in WAVE: a frequency grid comprising 24 logarithmically spaced bins between 0.05 Hz and 1.0 Hz; and a directional grid. For simulations with $\cos^{16}$ and $\cos^{50}$ wave spread, the directional grid comprises 18 bins at $5°$ intervals, covering a directional range $\pm 45°$ from shore normal. For the simulation with $\cos^{500}$ wave spread, the directional grid comprises 36 bins at $2.5°$ intervals, over the same directional range. This difference in setup is implemented because the narrower wave spread requires a higher directional resolution in order to function. Lateral basin boundaries are represented by a Neumann-type boundary defining a flat water level gradient in the alongshore direction—i.e. $\partial\zeta/\partial x = 0$ m m^{-1}. The offshore FLOW boundary is defined as a constant Riemann type boundary $R^{+}_{D3D}(t) = 0$ m s^{-1}. Waves are generated at the offshore WAVE boundary using a JONSWAP spectrum with parameters as shown in Table 4.8.

4.4.2 Results and discussion

Significant wave heights throughout the basins of each simulation at $t \approx 50$ hr are shown in Figure 4.9. Under the narrowest spread modelled of $\cos^{500}$ (Figure 4.9c), an alternating pattern of peaks and troughs of H_s can be seen. This is particularly evident at the upper region of the domain between $8 \leq y \leq 9$ km. Under a $\cos^{50}$ power spread (Figure 4.9b), a slight ‘diamond’ pattern of peaks and troughs

Table 4.8: Common Simulation Parameters: Coupled FLOW and WAVE Delta Morphodynamics Tests

Physical Parameters	Symbol	Value	Unit
Simulated time	T	50	hr
Discharge rate	Q_0	1280	$\mathrm{m}^3\,\mathrm{s}^{-1}$
Significant wave height	H_s	2	m
Peak wave period	T_p	5	s
JONSWAP peak enhancement factor	γ_0	3.3	-
Wave approach angle	θ	0	°
Numerical Parameters			
Time-step	Δt	9	s
Grid spacing, FLOW	Δx, Δy	25	m
Grid spacing, WAVE	Δx_w, Δy_w	50	m
FLOW–WAVE coupling period	-	60	min
Chézy friction factor	C	45	$\mathrm{m}^{1/2}\,\mathrm{s}^{-1}$

of significant wave height is evident. A similar pattern is also visible under the $\cos^{16}$ power spread, but is less pronounced. One possibility is that the emergence of these patterns is the result of interference between 'rays' of waves oriented along the discrete directions defined by the grid. This is a well-known issue when modelling waves using Lagrangian methods (Roelvink and Reniers, 2011), but it is unclear why the same phenomenon would result from the Eulerian approach used by WAVE. As the same issue does not arise in a WAVE only model, this is perhaps a consequence of the coupling methodology employed by Delft3D. Regardless, it is clear that the modelling of a near-unidirectional wave distribution (Figure 4.9c) does not produce a pattern of H_s values as might be expected for unidirectional waves.

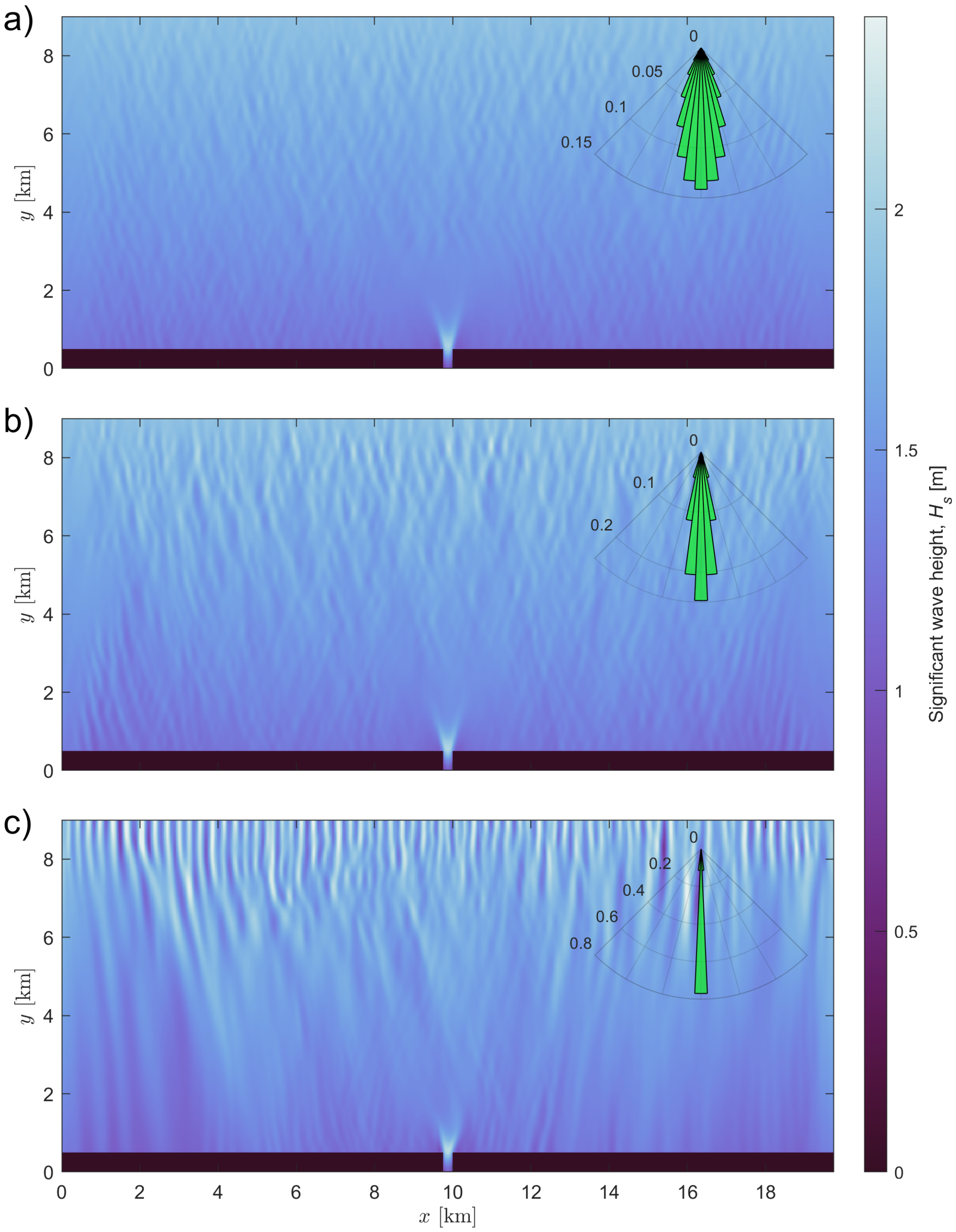

Figure 4.9: Significant wave heights for simulations with wave directional spreading distributions with powers of: a) $\cos^{16}$; b) $\cos^{50}$; and c) $\cos^{500}$. Inset polar plots show directional distribution of wave energy for that simulation. Values on the radial axes are the fraction of wave energy associated with waves oriented along the respective directional bin. All directional bins represent 5° ranges.

4.4.3 Concluding remarks

Here, three simulations were presented with differing directional distributions of waves modelled at the offshore boundary. It was found that increasingly narrow wave distributions introduced unrealistic patterns of H_s throughout the domains modelled, including significant alongshore variation. Given that our objective here is to model shore-normal waves with alongshore-invariant wave heights, we conclude that the best approach is to adopt a $\cos^{16}$ directional distribution for all further simulations.

4.5 Calibration of morphological acceleration factor for SVR formulae

Sensitivity testing of the morphological acceleration factor f_m (see §3.1.2.3) was conducted at a range of values from 1 to 700, and for various combinations of wave and tidal conditions. Here, the results of three morphodynamic models of delta development are presented, using morphological acceleration factors $f_m = 175$, 350, and 700. Preliminary tests in which transport calculations were restricted to either bedload or suspended load transport only (not included here) showed moderate mass balance errors in the former case and negligible mass balance errors in the latter, suggesting that the source of mass imbalance originates in the bedload transport calculations. As such, simulation data are additionally analysed using a Courant-Friedrichs-Lewy (CFL) criterion for bedform propagation (Ranasinghe et al., 2011).

Table 4.9: Common Simulation Parameters: Morphological Acceleration Factor Tests

Physical Parameters	Symbol	Value	Unit
Simulated time	T	48	yr
Discharge rate	Q_0	1280	$\mathrm{m}^3\,\mathrm{s}^{-1}$
Susp. sed. concentration at inlet boundary	$\bar{c}_{in}$	0.1	$\mathrm{kg}\,\mathrm{m}^{-3}$
Median grain size	D_{50}	0.125	mm
Tidal range	H_t	6	m
Tidal period	T_t	12.5	hr
Numerical Parameters			
Time-step	Δt	9	s
Grid spacing, FLOW	Δx, Δy	25	m
Chézy friction factor	C	45	$\mathrm{m}^{1/2}\,\mathrm{s}^{-1}$
Max. dry cell erosion factor	Θ_{SD}	1/3	-
DCEF threshold depth	$H_{max,\Theta}$	1.5	m

4.5.1 Model setup

Three simulations were run with identical setups other than f_m and (unaccelerated) duration. Common model parameters are given in Table 4.9. The test domain comprises a 19.75 km alongshore by 9.00 km cross-shore basin, into which a 0.5 km long, 250 m wide river with slope 1:5000 discharges. Lateral basin boundaries are represented by a Neumann-type boundary defining a flat water level gradient in the alongshore direction—i.e. $\partial\zeta/\partial x = 0$ $\mathrm{m}\,\mathrm{m}^{-1}$. The offshore boundary is defined using a harmonically varying Riemann type boundary $R^{+}_{D3D}(t) = -2.7678\sin(2\pi t/T_t)$ $\mathrm{m}\,\mathrm{s}^{-1}$.

Sediment transport is calculated using the SVR equations (see §3.1.2.1 and Deltares, 2021a). A 500 m wide beach is included adjacent to the onshore boundary. The beach is fully erodible to a depth of 5 m below mean sea level. The basin has a

1:1000 slope, running from a depth of 5 m below mean sea level adjacent to the beach, to a depth of 11.5 m at a distance of 6.5 km from the beach, beyond which this depth is maintained. Additionally, random bed elevation perturbations with a uniform distribution from 0 m to -0.05 m are applied throughout the basin. The basin itself is also erodible, with an initial sediment depth of 0 m adjacent to the beach, increasing linearly to an erodible depth of 20 m at a distance of 1 km from the beach. The initial erodible depth is 20 m at all points further offshore from this line. This configuration is adopted so as to maintain a smooth transition between the inerodible channel and erodible basin.

4.5.2 Determination of mass balance

Sediment mass balance is determined by comparing the measured and expected change in sediment volume over time within the entire domain. Measured total volume change ΔV_{total} [m^3] is calculated as the net volume difference—of both suspended and deposited sediments—between the simulation start and time of measurement, t. That is:

$$\Delta V_{total}\left(t\right) = \sum_{i=1}^{M}\sum_{j=1}^{N}\left(\Delta V_{sus}^{i,j}\left(t\right) + \frac{\Delta V_{bed}^{i,j}\left(t\right)}{f_m}\right) \tag{4.3}$$

where $\Delta V_{sus}^{i,j}$ is the net change in suspended sediment volume at the i by jth cell [m^3]; $\Delta V_{bed}^{i,j}$ is the net change in bedload sediment volume at the i by jth cell [m^3]; and M, N are number of cells in the x- and y-directions respectively.

Expected volume change $\Delta V_{exp} = \Delta V_{exp}(t)$ [m^3] is determined by summing the time integrals of sediment flux through all simulation boundaries. That is:

$$\Delta V_{exp}(t) = \sum_{k=1}^{4} \int_{t=0}^{t} \left(Q_{sus}^{k}(t) + Q_{bed}^{k}(t) \right) dt \tag{4.4}$$

where Q_{sus}^{k} is suspended sediment flux through the kth boundary [m^3 s^{-1}]; and Q_{bed}^{k} is bedload sediment flux at the kth boundary [m^3 s^{-1}]. Note that positive (negative) values of Q_{sus} and Q_{bed} denote sediment flux entering (leaving) the model domain. While bedload boundary fluxes and offshore sediment fluxes are included in these calculations, it should be noted that all sediment fluxes except for suspended load entering via the river are negligible in the simulations presented here. The absolute error in sediment mass balance at time t is $\Delta V_{err}(t) = \Delta V_{total}(t) - \Delta V_{exp}(t)$ and relative error is $\Delta V_{err}(t) / \Delta V_{total}(t)$. Therefore, a positive (negative) absolute error indicates that sediment is being erroneously created (destroyed) by the model.

Figure 4.10 shows absolute and relative mass balance errors for all three simulations over (morphologically accelerated) time t. At $f_m = 175$, mass imbalance errors are negligible. At $f_m = 350$, the relative mass balance error approaches a relatively constant value of 0.15. At $f_m = 700$, the relative error increases to around 0.5. This means that for every 1 m^3 of sediment entering the domain, a further 0.5 m^3 is being erroneously created.

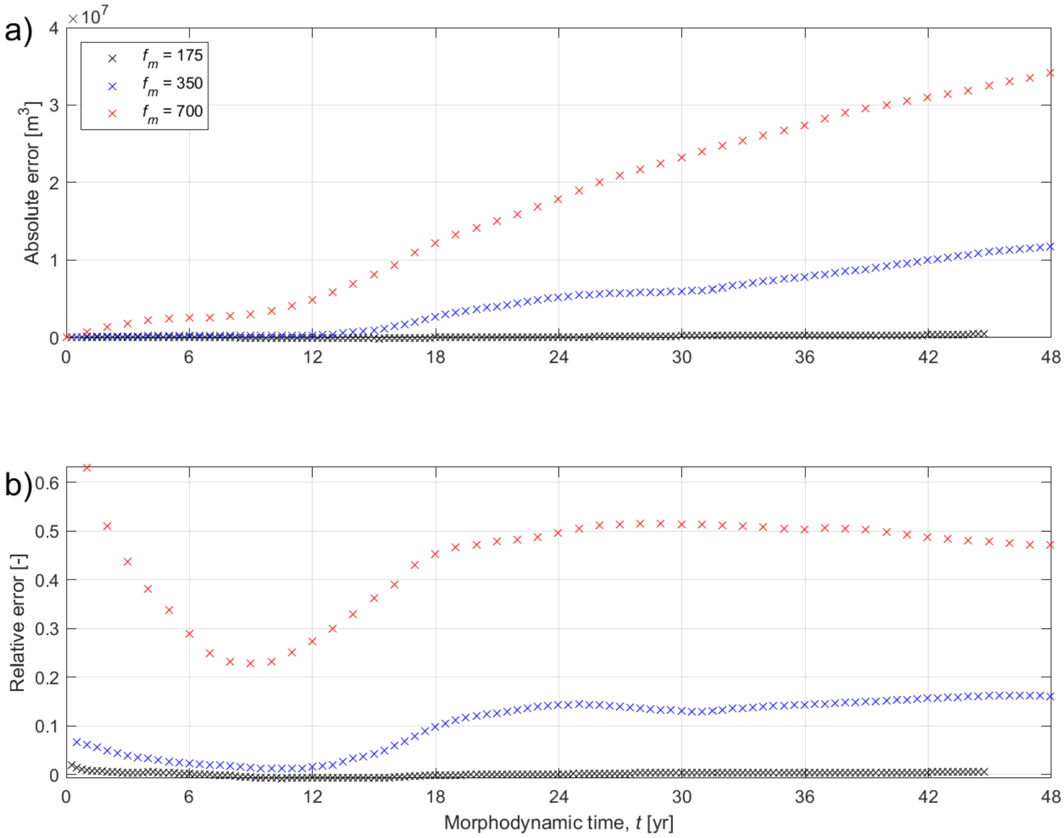

Figure 4.10: a) Absolute error; and b) relative error over time in sediment volume in f_m sensitivity tests.

4.5.3 Courant-Freidrichs-Lewy (CFL) stability criterion for bedform propagation

Ranasinghe et al. (2011) analysed the stability of bedload transport formulae using a CFL-based stability criterion. Their method is comparable to the CFL stability criterion commonly applied to numerical solutions of PDEs such as the shallow water equations. Whereas the Courant number for the shallow water equations relates the celerity of a surface disturbance to time step and grid size, the Courant number for bedform propagation instead relates the (morphologically accelerated) celerity of bedforms to these numerical parameters. The Courant numbers for bedform stability $C_{bed,x}$, $C_{bed,y}$ [-] are:

$$C_{bed,x} = f_m \frac{b|\vec{q}_{b,x}|}{(1-\epsilon)\,h} \frac{dt}{dx}, \tag{4.5}$$

$$C_{bed,y} = f_m \frac{b|\vec{q}_{b,y}|}{(1-\epsilon)\,h} \frac{dt}{dy} \tag{4.6}$$

where b is the power by which flow velocity is related to bedload flux, i.e. $q_b \propto u^b$; and ϵ is sediment bed porosity. The power relationship for bedload transport under the SVR formulae (Eq. (3.7)) is $b = 3.4$, and soil porosity $\epsilon \approx 0.4$. In their initial (1D) tests, Ranasinghe et al. (2011) found a value of $C_{bed} \leq 0.05$ to be unconditionally stable. As such, in order to estimate bedload transport stability, Eqs. (4.5) and (4.6) are applied to all cells at all output times for each simulation, and the proportion of cells with $C_{bed} > 0.05$ calculated in each simulation.

Table 4.10: Proportion of Cells at all Times and Locations Exceeding $C_{bed} = 0.05$.

Simulation f_m-value [-]	Percentage of cells with $C_{bed} > 0.05$ [%]
175	0.0002
350	0.0012
700	0.0031

Table 4.10 shows the percentage of cells (all basin cells at all simulation output times, analysed in both x- and y-directions) with $C_{bed} > 0.05$. While the proportion of cells exceeding the suggested stability criterion of Ranasinghe et al. (2011) is small in all cases, the increase of f_m from 175 to 700 does see this measure increase by a factor of approximately fifteen.

4.5.4 Concluding remarks

Increasing the morphological acceleration factor f_m beyond a value of 175 in these tests resulted in the introduction of large mass balance errors. Clearly, the creation of 10–50% of additional sediment beyond the expected amount renders any simulation results invalid. As such, a value of $f_m = 175$ is used in all subsequent simulations using the SVR formulae. Selection of this value allows for the modelling of much longer durations than would otherwise be feasible, if not employing this morphological acceleration technique, while introducing only negligible errors.

A causal link was not established between instability of bedload transport and mass balance errors. However, the proportion of cells exceeding the recommended minimum stability criteria of Ranasinghe et al. (2011) increased by a factor of approximately fifteen when increasing f_m from 175 to 700. This suggests that unstable bedload transport is a potential source of error, particularly in the higher f_m simulations.

4.6 Comparison of the mathematical morphological method (MMM) and opening angle method (OAM) for defining the shoreline

This section compares two methods for defining shorelines on deltas / complex coasts, investigated for their potential application in analysing delta morphodynamics in later tests. These are the mathematical morphological method (MMM – Geleynse et al., 2012) and opening angle method (OAM – Shaw et al., 2008).

In general, the shoreline may be defined simply as the instantaneous boundary dividing land and water (see e.g. Bird, 2008). It follows that in tidal regions, the shoreline may change position as the tide rises or falls. Defining the precise location of the shoreline can be challenging for a river delta; a complex morphological structure potentially featuring extensive flats with elevations similar to the mean water level, wide estuarine regions, (partially) enclosed bays or lagoons, emergent bars and islands, and complex branching networks of channels. Intuitively, we do not want to define the shoreline as extending upstream along the banks of such channels. As such, the simple definition given above cannot be considered sufficiently precise for identifying the shoreline location for deltas or similarly complex coasts. Both the MMM and OAM are primarily concerned with the 'closing' of channel mouths, such that the defined shorelines do not extend upstream into channels. They are each applied to any 'gridded' form of data; this may be either a pixelated image, as from satellite or aerial photography, or the output of a numerical simulation on a regular square grid, as here. Of the two methods, the OAM has been applied more extensively in delta modelling (e.g. Wolinsky et al., 2010; Caldwell and Edmonds, 2014; Burpee et al., 2015; Tejedor et al., 2016; Liang et al., 2016; Liu et al., 2020; Broaddus et al., 2022), whereas only one delta modelling study to our knowledge has applied the MMM (that of Lageweg and Slangen, 2017). Illustration of the differences between these methods is made by applying them to an example simulation as described in §4.6.4.

A schematic diagram indicating examples of the low and high tide (shore)lines, coastline, and other definitions relevant to deltas, is shown in Figure 4.11. Note that while the terms shoreline and coastline are often used as synonyms, here we adopt the distinct definition of 'coastline' as referring to the boundary between 'solid' land and the shore (see e.g. Bird, 2008). In some cases, such as cliff-coasts, the shoreline and coastline may coincide. While the OAM and MMM were created with identification of the shoreline in mind, here we classify any regions of land not connected to the main body of land to be 'offshore' bars or islands, and the lines circumscribing these features as low and high tide *lines*, rather than low and high tide *shorelines*. Furthermore, both of these methods may (with some adaptation—see §4.6.3) also be used to identify the perimeter of the delta or, generically, the perimeter of a deposited mass of sediment. Notionally, this is the toe of the relatively steep 'front' of sediments which typically forms when sediments are deposited at the mouths of rivers. This is useful as the same issues related to the shoreline tracking upstream along the banks of channels may also occur where channels incise below the initial basin depth. Such consistency of approach is also considered beneficial as the precise locations of the sediment mass front and shorelines will be later used to quantify morphodynamic development by location (see §5.3).

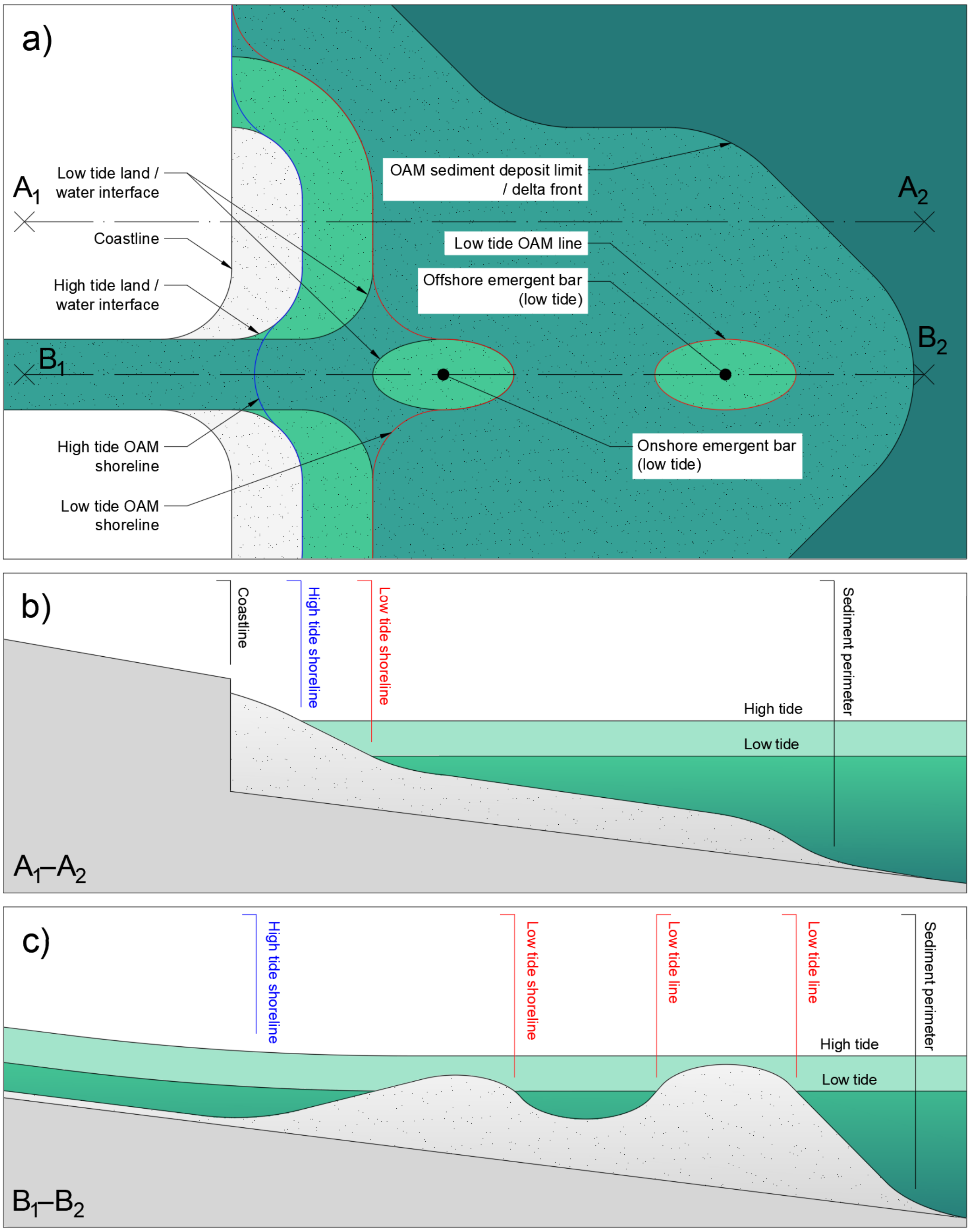

Figure 4.11: Schematic showing example of the coastline, as well as the low and high tide (shore)lines and sediment mass perimeter. Sub-figures show: a) plan view showing example onshore and offshore bars within a sediment deposit, as distinguished by the location of the low tide shoreline; b) transect A$_1$–A$_2$; and c) transect B$_1$–B$_2$.

4.6.1 Overview of the mathematical morphological method

The MMM comprises four steps (for a complete description of the method, see Geleynse et al., 2012):

1. define cells as either wet or dry;
2. define a shape or 'structural element' to be used for steps (3) and (4);
3. mathematically 'dilate' all dry cells using the structural element; and
4. mathematically 'erode' all dilated cells using the structural element.

This process is illustrated in Figure 4.12, wherein sub-figures (a) to (d) correspond to steps (1) to (4) respectively. For every dry cell shown in Figure 4.12a, the structural element is overlaid, with the central origin point corresponding to the cell location. Then, all surrounding cells corresponding to the additional cells described by the structural element shown in Figure 4.12b are defined as part of the dilated matrix. Applying this process for all dry cells leads to the matrix shown in Figure 4.12c. The same structural element is then used to perform the erosive process. The structural element is overlaid on each 'positive' cell of the dilated matrix (white or grey in Figure 4.12c), and that cell is then defined as part of the 'eroded' matrix only if all surrounding cells bounded by the structural element are also 'positive' cells of the dilated matrix. This leads to the eroded matrix shown in Figure 4.12d, from which (shore)lines are then defined as the boundaries between positive and negative cells. The effect of applying the above steps is to 'close' any narrow regions of wet area. Following application of the method, boundary lines are identified as the boundaries between black cells and white / grey cells.

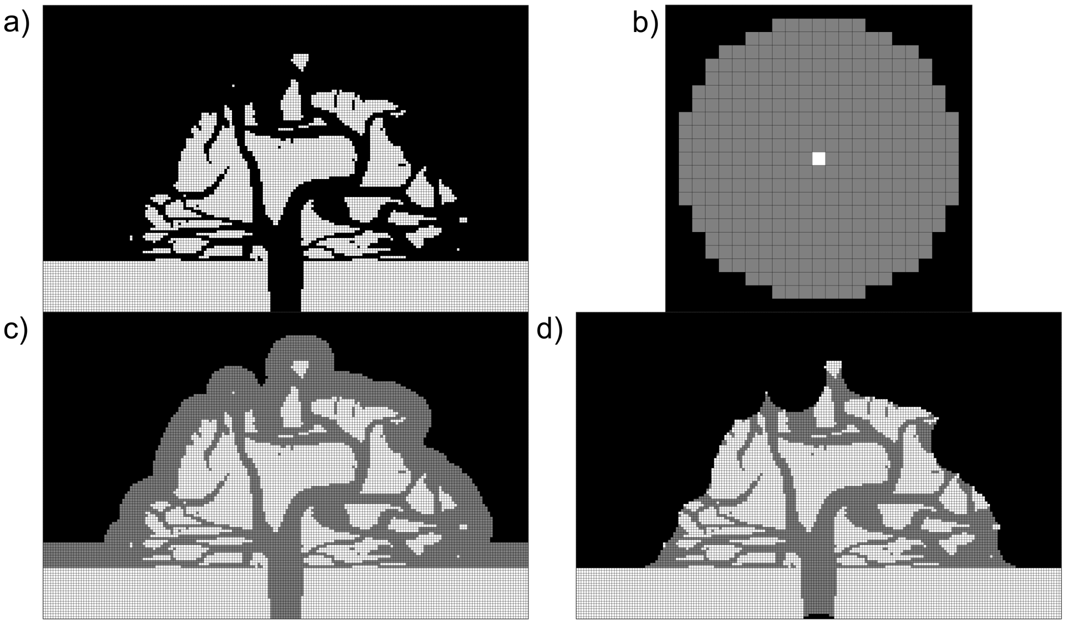

Figure 4.12: Example application of the mathematical morphological method at low tide. Shown are: a) a typical grid of wet (black) and dry (white) cells; b) the defined structural element used for the dilation and erosion processes, where the white cell is the 'origin' of the structural element, and grey cells represent the extent of dilation (the shape and size of this element follow the recommendations of Geleynse et al., 2012); c) the dilated matrix, where white cells are original dry cells, and grey are additional 'positive' cells defined by the dilation process; and d) the eroded matrix, where white cells are original dry cells, and grey are 'positive' cells remaining following both dilation and erosion.

Amongst these boundary lines, the single line circumscribing the majority area of the eroded matrix is identified as the shoreline. Note that this method can result in enclosed internal 'wet' regions for a given pattern of wet and dry cells, depending on the chosen structural element and initial matrix of wet / dry cells. Such regions may be disregarded, as they do not impact the definition of either the shoreline or lines delineating offshore bars and islands.

4.6.2 Overview of the opening angle method

The OAM identifies the shoreline as the locus of points for which the "opening angle" ϕ [°] is equal to a specified critical threshold value ϕ_c [°] (Shaw et al., 2008). The opening angle itself is defined as the sum of angles of all arcs originating from a given (wet) point, traceable through sweeps that do not intersect land. Wet regions where $\phi \geq \phi_c$ are considered to be offshore, open water. Wet regions where $\phi < \phi_c$ are considered to be onshore / inland hydrological features, such as channels or bays. This concept is illustrated in the schematic shown as Figure 4.13. As with the MMM, the single line circumscribing the majority of the initial dry regions is identified as the shoreline. For both the MMM and OAM, we count cells as dry where instantaneous water depth $h < h_c$, where h_c is a wet / dry depth threshold [m]. Here, a depth threshold $h_c = 0.11$ m is applied. This value is selected primarily for reasons related to limitations of the model. Specifically, when water depth $h < 0.1$ m, Delft3D does not calculate bedload transport into or out of a given cell, nor any deposition (entrainment) of sediment from (into) the water column (Deltares, 2021a). This limitation (intended to prevent the calculation of unrealistically high sediment fluxes in very shallow regions) essentially fixes the bathymetry, even when a cell may still be hydrodynamically active. As such, we apply this value $+10\%$ when defining wet and dry cells, so as to safely avoid erroneously counting morphologically inactive (functionally dry) cells as wet. For the OAM, a threshold opening angle $\phi_c = 70°$ is used. For the MMM, a disc-shaped structural element with diameter sufficient to 'close' channels close to the delta periphery is used, following the recommendation of Geleynse et al. (2012). In order to achieve this, we here employ a structural element with radius approximately equal to the initial river width, under the reasoning that this will be sufficient to close any downstream channels, which are likely to be narrower than the river mouth in most instances.

4.6.3 Application of the MMM and OAM to determining the perimeter of the deposited sediment mass

Both the MMM and OAM may also be applied in order to determine the location of the perimeter of the deposited sediment mass / delta. Here, we define the perimeter as the toe of the relatively steep front of deposited sediment (the "delta front" in deltaic morphologies), as this line typically encompasses $> 99\%$ of the river-delivered sediments. This definition excludes the fine layer of river-delivered sediments which may be deposited far beyond this point (the "pro-delta" in deltaic morphologies). In order to identify this perimeter, the first step of each method—i.e. the classification of cells as either wet or dry—is replaced with making a distinction between cells for which the bed level has or has not increased beyond a threshold value at the time measured with respect to the initial bed level. In order to omit the thin layer of sediments beyond the sediment front as described above, a threshold bed level change $\Delta z_c = 0.25$ m is used here. Where bed level has increased beyond this threshold value, these cells compose the positive cells of the initial matrix (equivalent to dry cells when determining shorelines). Where bed level has not increased beyond the threshold value, these cells compose the negative cells of the initial matrix (equivalent to wet cells when determining shorelines). All further steps as described above for both methods are then followed, using this alternative initial matrix. The same threshold opening angle $\phi_c = 70°$ is used,

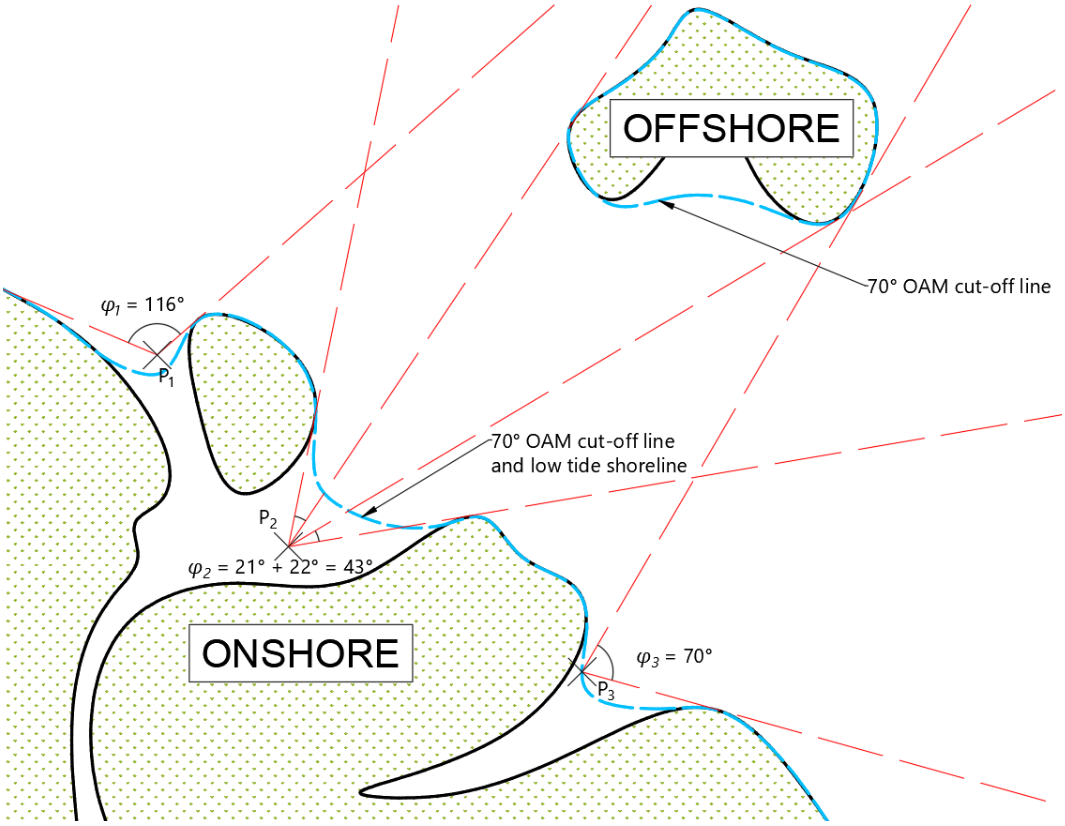

Figure 4.13: Illustration of the opening angle method applied at low tide. Black lines denote land-water interfaces. Green hatched areas denote land. Empty space denotes water. Blue dashed lines denote the locus of points where $\phi = \phi_c = 70°$. Red dashed lines denote angles subtended by land-water interfaces from example wet points. Black crosses are example wet points: P_1 has opening angle $\phi = 116°$ and is therefore counted as open water; P_2 has opening angle $\phi = 43°$ and is therefore counted as an onshore wet region; and P_3 has opening angle $\phi = 70°$, representing a point along the shoreline separating on and offshore regions.

with the contour thus defined denoting the outer extent of the sediment mass. For instances in which a given morphology is identified as a delta, this contour also indicates the location of the delta front.

4.6.4 Model setup

One simulation was run to generate an example delta, and both shoreline definition methods applied at $t \approx 35.75$ yr in order to determine low tide (shore)lines and the sediment mass perimeter. This simulation is identical to simulation W1.2T5.0, as presented in §5.1.

4.6.5 Results and discussion

Application of both methods to the matrix of wet and dry cells at low tide determined at $t \approx 35.75$ yr is illustrated in Figure 4.14. The resulting low tide (shore)lines and sediment mass perimeters are shown alongside simulation bathymetry in Figure 4.15. While both methods produce shorelines in approximately similar locations, the shoreline shape determined using the MMM has a noticeable dependence on the structural element used. The need to use a structural element of sufficient scale to ‘close’ channel mouths means that any features of the shoreline with length scales smaller than the chosen element are not well represented by the MMM (Figure 4.15a). The OAM, by contrast, does not require any calibration based on grid size, and is able to more accurately reflect smaller scale features of the shoreline (Figure 4.15b). This need to calibrate the MMM to channel scale also presents potential issues with consistency when applied between different simulations, or even at different times within a single simulation. The

MMM also notably produces isolated wet areas lying within the region circumscribed by the shoreline, the extent of which are also sensitive to the shape and size of the structural element used—compare Figures 4.14c and d, in which two small 'negative' cells on the right side of the delta in (c) lead to definition of a large wet area in (d). The 'visibility' criterion of the OAM means that such areas do not appear when using this method—this is evident in inspection of Figure 4.14b. In contrast to the low tide shorelines, the sediment mass perimeters produced by each method are similar; this is because the initial matrix based on bed level changes is considerably less complex—i.e. has fewer, narrower areas of 'negative' cells, and fewer, larger distinct blocks of 'positive' cells—than the initial matrix of wet / dry cells used to determine the low tide (shore)lines. This highlights that each approach is sensitive to the complexity of the initial matrices used.

4.6.6 Concluding remarks

Overall, the OAM offers several benefits over the MMM: it is scale-independent and does not need calibration to fit the specifics of a given simulation; it is better able to represent shoreline features at length scales below that of the structural element used for the MMM; and it does not create isolated regions of wet area within the area circumscribed by the shoreline, which would require further consideration and processing. The only notable drawback to use of the OAM in comparison to the MMM is that it is somewhat more computationally expensive to run.

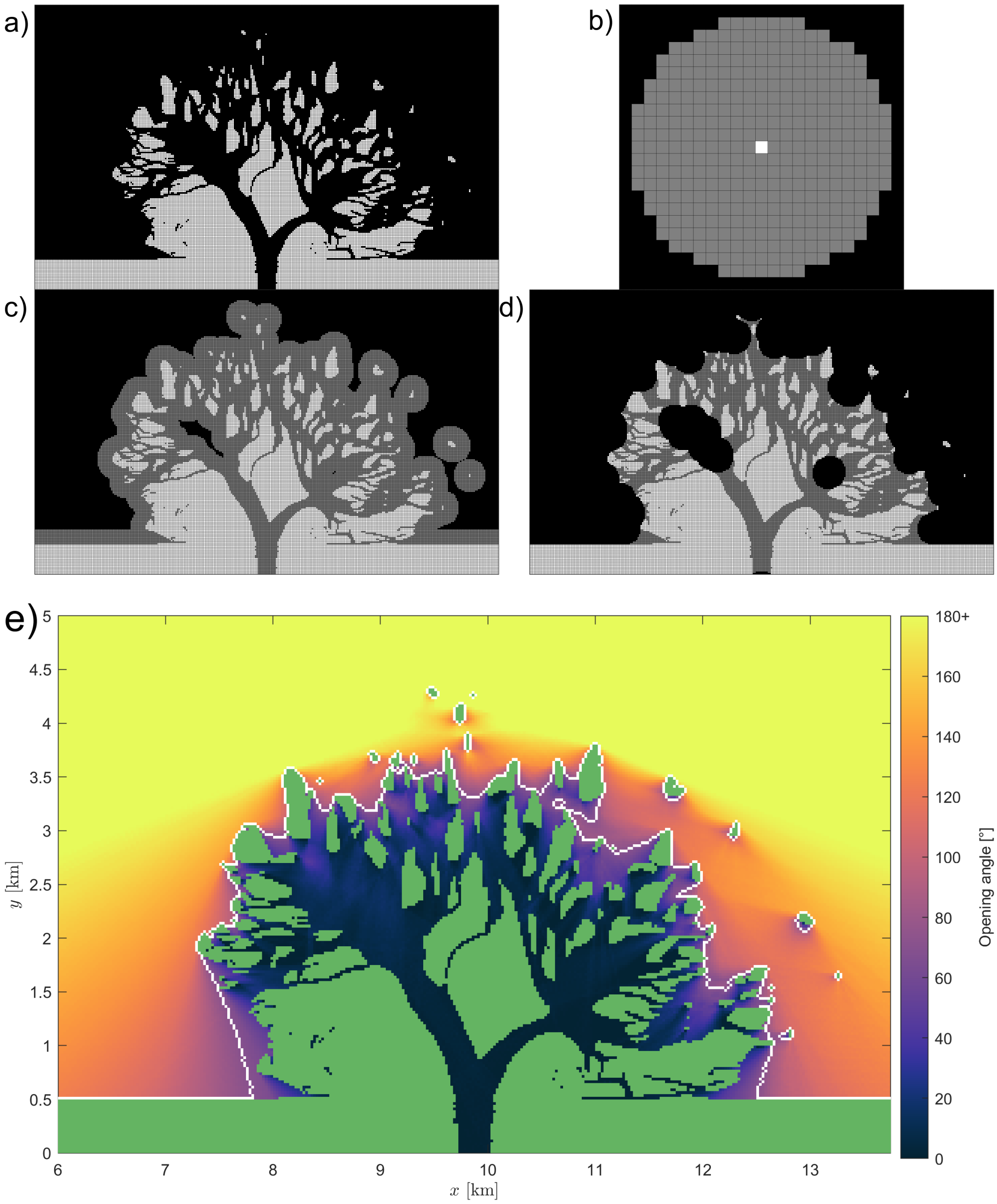

Figure 4.14: Application of the MMM (a to d) and OAM (e) to the test setup. Sub-figures show: a) the initial matrix of wet (black) and dry (white) cells; b) the structural element used; c) the dilated matrix; d) the eroded matrix; and e) opening angles for all wet cells, with the locus of points for which $\phi = \phi_c = 70°$ indicated in white, and land indicated in green. Colours other than green and white in (e) indicate the opening angle determined per cell.

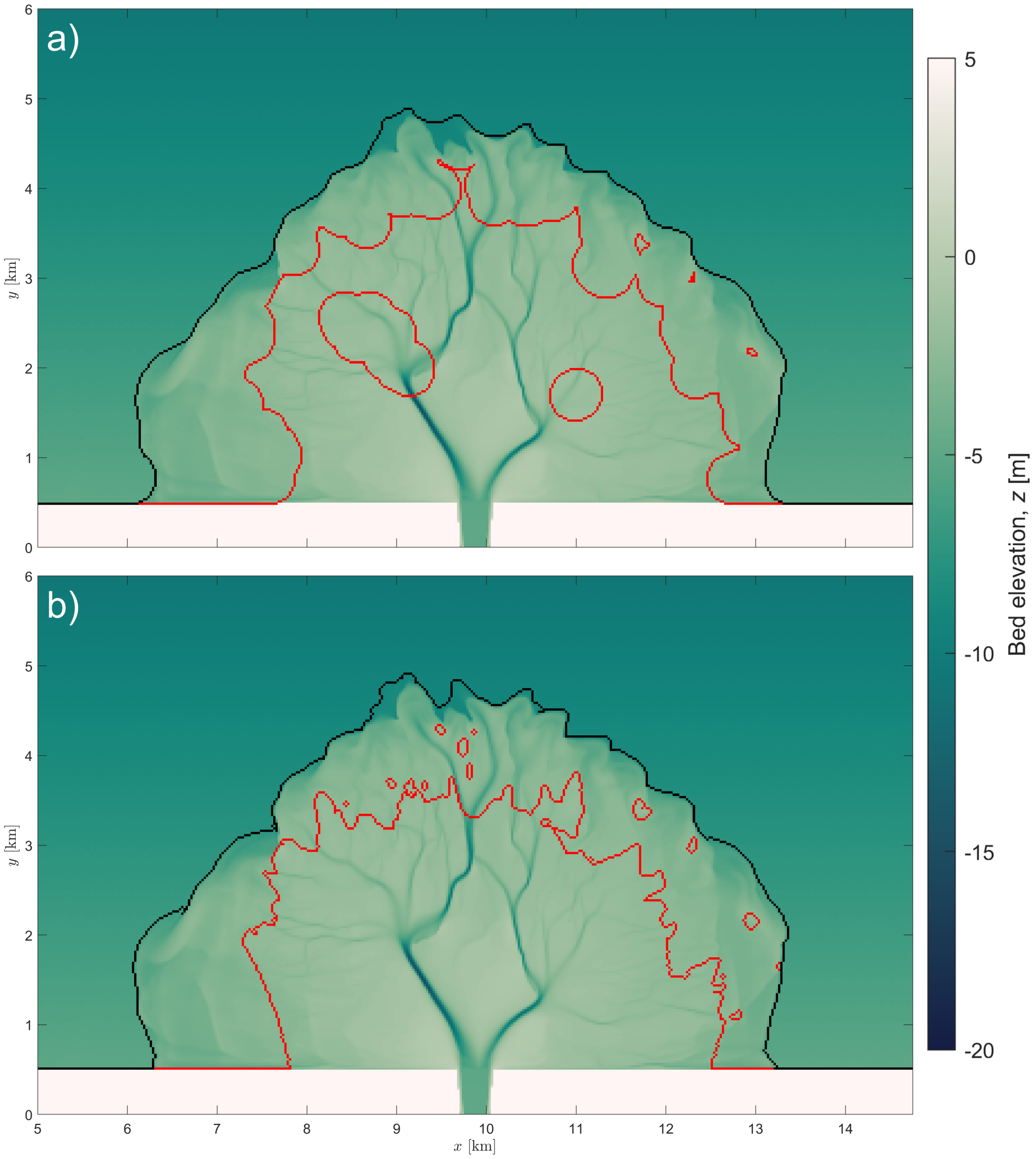

Figure 4.15: Bathymetry with low tide (shore)lines (red lines) and sediment mass perimeters (black lines) at $t \approx 35.75$ yr determined using: a) the mathematical morphological method; and b) the opening angle method.

Chapter 5

Numerical methodology for investigating the inhibiting effects of tidal range and significant wave height on delta development

A range of simulations was designed with the objective of investigating the potential inhibiting effects of tidal range and significant wave height on delta formation. The setup of these simulations is given in §5.1; methodology for systematically classifying the resultant morphologies as deltas (or not) described in §5.2; and description of the methods and metrics used to quantify different aspects of morphological development outlined in §5.3.

5.1 Model setup

Forty-two numerical simulations were run, designed to investigate the effects of different combinations of wave height and tidal range on the processes that form deltas on open coasts. In order to simplify analysis and retain a reasonable scope, the parameter space is restricted in a number of ways. River discharge Q_0 [m^3 s^{-1}] and sediment discharge Q_{sed} [m^3 s^{-1}] are held constant, both within and between simulations. Waves are modelled with a shore-normal mean direction and narrow spread at the offshore boundary, with the only wave-related parameter varied being significant wave height H_s [m]. Tides are modelled with an approximately semidiurnal period ($T_t = 12.5$ hr) and shore-normal direction, such that no net alongshore tidal currents are induced, and with the only tide-related parameter varied being tidal range H_t [m].

The findings of Caldwell et al. (2019) are applied to inform the choice of parameters used in our numerical models, so as to give a range of both positive and negative predictions of delta occurrence, while also covering combinations of H_s and H_t typical of the environments into which most of the world's rivers discharge. Caldwell et al. (2019) related delta presence for 5,399 rivers to (mean annual) Q_0, Q_{sed}, H_s, and H_t. Larger Q_0 and Q_{sed} were found to increase the likelihood of a delta being present, while larger H_s and H_t were found to decrease likelihood of a delta being present. Based on this analysis, they proposed a formula for estimating the probability π_Δ of a given river forming a delta:

$$\pi_\Delta = \frac{\exp\left(1.45 + 0.000589\langle Q_0\rangle + 2.56\langle Q_{sed}\rangle - 0.975\langle H_s\rangle - 0.187\langle H_t\rangle\right)}{1 + \exp\left(1.45 + 0.000589\langle Q_0\rangle + 2.56\langle Q_{sed}\rangle - 0.975\langle H_s\rangle - 0.187\langle H_t\rangle\right)} \tag{5.1}$$

where $\langle Q_0 \rangle$ is mean annual volumetric river water flux [m^3 s^{-1}]; $\langle Q_{sed} \rangle$ is mean annual volumetric river sediment flux [m^3 s^{-1}]; $\langle H_s \rangle$ is the annual mean of hourly significant wave heights [m]; and $\langle H_t \rangle$ is mean annual tidal range [m]. Values of π_Δ range from 0 to 1, with values greater than 0.5 considered to represent conditions for which a delta is likely to form and values less than 0.5 to represent those for which a delta is unlikely to form. We model combinations of H_s up to 2 m, and H_t up to 6 m, giving the range of π_Δ values shown in Figure 5.2, and broadly representing marine conditions typical for such environments globally (Figure 5.1). For the purposes of this study, it is assumed that steady H_s values produce equivalent morphologies to respective unsteady H_s values with identical temporal means, and that fixed-amplitude tides produce equivalent morphologies to real tides in which the lunar semidiurnal (M2) component is dominant.

Various simulation parameters are summarised in Table 5.1. We first note that volumetric discharges vary enormously between real rivers. As the world's highest-discharging rivers almost universally produce deltas (Caldwell et al., 2019), Q_0 is set to a modest rate of 1280 m^3 s^{-1}, for which delta presence is less certain (a value which also leads to a range of π_Δ values greater than or less than 0.5, as well as three simulations giving π_Δ values of approximately 0.5; useful in testing how well Eq. (5.1) agrees with our simulations). This discharge rate is representative of rivers such as the Chao Phraya, Copper, Ebro, Po, and Vistula (Syvitski and Saito, 2007), and the width of the modelled river is typical of rivers with this discharge (Frasson et al., 2019). The depth-averaged fine sand mass concentration $\bar{c}_{mass} = 0.1$ kg m^{-3} (volumetric concentration $\bar{c} = 3.77 \times 10^{-5}$ m^3 m^{-3}) at the inflow is at the lower end of concentrations seen in such rivers (Syvitski and Saito,

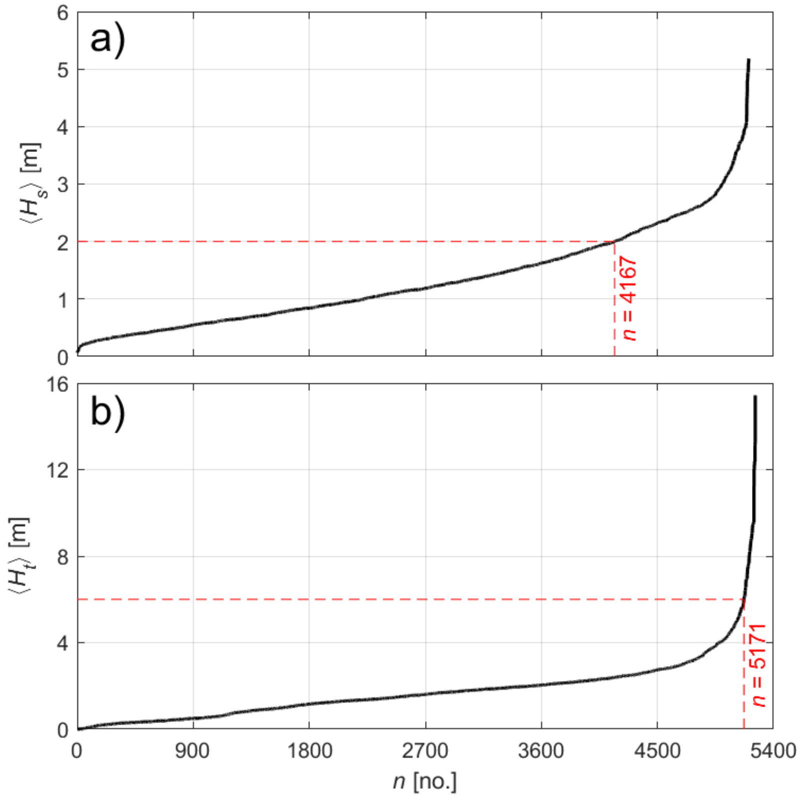

Figure 5.1: Values of: a) $\langle H_s \rangle$; and b) $\langle H_t \rangle$ associated with rivers investigated by Caldwell et al. (2019). Data are arranged in ascending order of magnitude. Red dashed lines indicate the maximum values of $\langle H_s \rangle$ and $\langle H_t \rangle$ used in the present study, as well as the approximate proportion of the dataset covered by the ranges modelled. (Note that there are gaps in the dataset, hence there are fewer than 5,399 values in each subplot.)

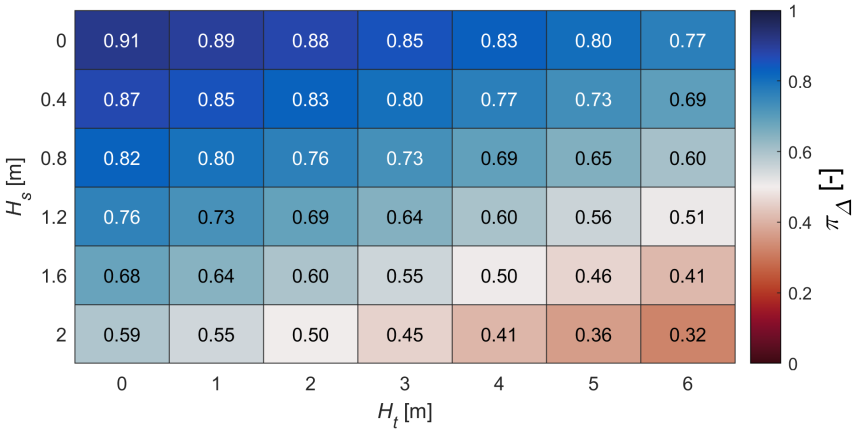

H_s [m] \ H_t [m]	0	1	2	3	4	5	6
0	0.91	0.89	0.88	0.85	0.83	0.80	0.77
0.4	0.87	0.85	0.83	0.80	0.77	0.73	0.69
0.8	0.82	0.80	0.76	0.73	0.69	0.65	0.60
1.2	0.76	0.73	0.69	0.64	0.60	0.56	0.51
1.6	0.68	0.64	0.60	0.55	0.50	0.46	0.41
2	0.59	0.55	0.50	0.45	0.41	0.36	0.32

Figure 5.2: Values of π_Δ calculated using Eq. (5.1) for all simulations.

2007; Milliman and Farnsworth, 2011) (see Figure 5.3). This value is selected in order to ensure that some simulations are predicted not to form deltas according to Eq. (5.1). Additionally, both Q_0 and $\bar{c}$ are also chosen for comparability to prior numerical studies of deltas, for which discharges and concentrations are often close to these values (e.g. Edmonds and Slingerland, 2010; Geleynse et al., 2010, 2011; Caldwell and Edmonds, 2014; Burpee et al., 2015; van der Vegt et al., 2016; Gao et al., 2019). Here it is assumed that the application of these temporally unvarying discharge boundaries produces results that do not differ substantially from equivalent temporally varying conditions with identical means. The fine sand median diameter $D_{50,f} = 0.125$ mm is in the typical range for many rivers, particularly those with discharges close to our selected value of Q_0 (Orton and Reading, 1993; Syvitski and Saito, 2007), and is also comparable to values used in previous numerical modelling studies on deltas (e.g. Edmonds and Slingerland, 2010; Geleynse et al., 2010; van der Vegt et al., 2016; Gao et al., 2019; Broaddus et al., 2022).

Nearshore sediment distributions are generally characterised by onshore coarsening of sediments. Rather than attempt to precisely model this gradation throughout the model domain, we instead choose a single coarse sand of $D_{50,c} = 1.0$ mm (distinct from the fine sediment fraction $D_{50,f}$ modelled as a river input) and set the sediment diameter to this value in all initially erodible regions of sediment in the domain (see §5.1.2). The use of this coarse sediment fraction in the basin allows for some incision of the expected delta channels below the initial bed level, while also minimising reworking of initial bed sediments—a result of the higher mobilization stresses required for the coarser sediment compared to the fine. Setting

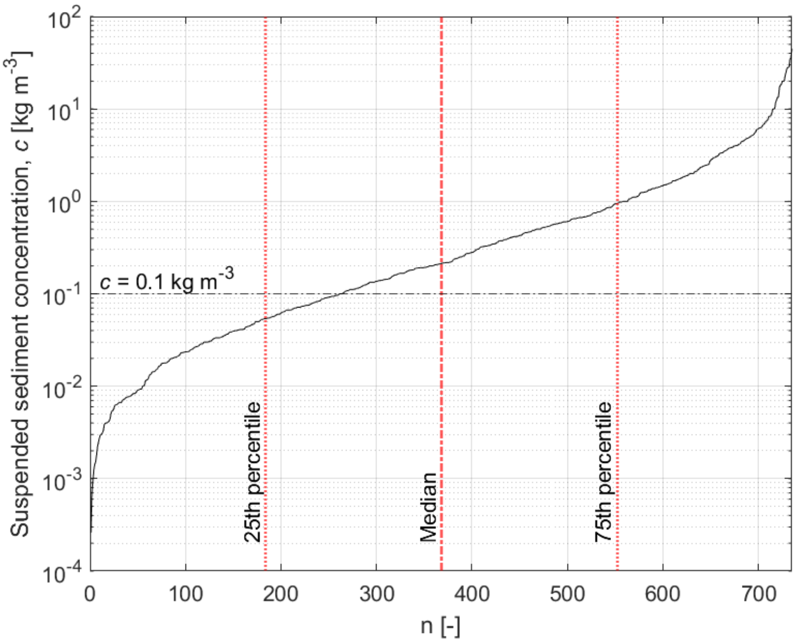

Figure 5.3: Suspended sediment concentrations (SSCs) for 735 global rivers from Milliman and Farnsworth (2011). Data are arranged in ascending order of SSC. The black dashed line highlights that the modelled input concentration from our simulations ($\bar{c}_{in} = 0.1$ kg s^{-1}) is below the median concentration for rivers globally.

Table 5.1: Model Parameters

Physical Parameters	Symbol	Value	Unit
Water density	ρ_0	1000	kg m^{-3}
Upstream discharge	Q_0	1280	m^3 s^{-1}
Tidal period	T_t	12.5	hr
Depth-averaged concentration at inflow	$\bar{c}_{mass}$	0.1	kg m^{-3}
Sediment flux at inflow	Q_{sed}	0.048	m^3 s^{-1}
Grain particle density	ρ_s	2650	kg m^{-3}
Sand dry bulk density	ρ_{bulk}	1600	kg m^{-3}
Fine sand median diameter	$D_{50,f}$	0.125	mm
Coarse sand median diameter	$D_{50,c}$	1.0	mm
Numerical Parameters			
Time-step	Δt	9	s
Morphological acceleration factor	f_m	175	-
Chézy roughness coefficient	C	45	m$^{1/2}$ s^{-1}
FLOW-WAVE coupling period	-	60	min

the simulations up in this way simplifies the analysis of the morphologies produced, particularly under the higher energy marine conditions modelled. Note that sediments in the cohesive range ($D_{50} < 0.064$ mm) are not modelled. The presence of cohesive sediments may be expected to have two significant effects on delta-forming processes: a wider spread of sediments beyond discharging river mouths, as cohesive sediments in general have a slower settling velocity than non-cohesive; and an increase in the critical bed shear stresses required for remobilisation (in Delft3D, based on a constant value specified by the user; in reality, somewhat dependent upon the degree of consolidation over time). These effects lead to slower mouth bar growth, as well as reduced likelihood of avulsions (Orton and Reading, 1993; Edmonds and Slingerland, 2010; Caldwell and Edmonds, 2014; Burpee et al., 2015). As the proportion of cohesive sediments increases, morphologies would therefore be expected to tend towards the development of fewer, longer channels (Geleynse et al., 2011; Guo et al., 2015). As such, given that the presence of cohesive sediments would be expected to produce different morphological outcomes in comparison to simulations in which they are absent, the results presented herein should only be considered valid for rivers in which the cohesive fraction is negligible with respect to the non-cohesive.

The decision not to include cohesive sediments alongside non-cohesive is in many ways a practical consideration, as their presence introduces complexity in terms of sediment interaction, such as the hiding / exposure of finer sediments by coarser ones. As argued earlier, an idealised modelling approach is adopted as this allows for the easier interpretation of the effects of variation in H_s and H_t, which is the principle focus of this study. This extends to the simplified representation of sediment diameter and distribution. Furthermore, it should be noted that comprehensive global data on the size and distribution of sediments transported at river mouths is lacking at present. In general, this makes any argument concerning the precise distribution of sediment adopted difficult to justify, except for specific case studies in which comprehensive data is in fact available.

As salinity variation and related effects such as gravity currents are not accounted for in the 2D depth-averaged model, a constant water density $\rho_0 = 1000$ kg m^{-3} is used throughout. Sands are deposited at a dry bulk density $\rho_{bulk} = 1600$ kg m^{-3} ($\rho_{bulk} = \rho_s(1-n)$ where $n \approx 0.4$ is porosity of deposited sediments), typical for predominantly sandy mixtures (van Rijn, 1993). This value is also commonly used in prior delta modelling studies (e.g. Edmonds and Slingerland, 2010; Geleynse et al., 2010, 2011; Burpee et al., 2015; Baar et al., 2019). The time step $\Delta t = 9$ s is selected to satisfy all Courant stability requirements for the model (see Deltares, 2021a). The choice of $f_m = 175$ follows sensitivity testing which revealed that while values of $f_m \leq 175$ did not significantly alter morphological development, higher values led to large sediment mass-balance errors (see §4.5). A Chézy roughness coefficient $C = 45$ m$^{1/2}$ s^{-1} is used (equivalent to dimensionless friction coefficient $C_d = g/C^2 = 4.8\dot{4} \times 10^{-3}$) for comparability to prior studies, where this is again a frequently used value (e.g. Edmonds and Slingerland, 2010; Caldwell and Edmonds, 2014; Burpee et al., 2015; Lageweg and Slangen, 2017; Gao et al., 2019).

The presence of two distinct sediment fractions ($D_{50,f} = 0.125$ mm and $D_{50,c} = 1.0$ mm) necessitates the implementation of multiple bed layers in order to represent layering of sediments over time (as compared to the default implementation comprising a single, fully mixed, base layer plus a transport layer). Here we implement a setup comprising an upper transport layer of thickness $\max(0.05h, 0.05)$ m, below which are up to five underlayers of maximum thickness 0.35 m each, with all sediment beneath these layers contained within a base layer which extends down to the inerodible basement (see Deltares, 2021a, and §3.1.2.5).

All simulations are run for an initial 36 yr of morphodynamic development. Simulations that do not form a delta within this time are extended to run for an additional 36 yr. In some simulations, a delta does not form within 72 yr. While formation of a delta within 72 yr within the simulation provides a reasonable basis for supposing that delta formation would also occur in a similar real-world system, non-formation of a delta does not so simply support the conclusion that a delta would never form in a similar real-world system. This is especially true when considering the up-to-millennial timescales over which many real world river deltas have in fact formed. However, as will be argued in Chapter 7, under larger H_s and H_t, sediment may be diffused away from the river mouth at a similar rate to that at which it arrives. This approximate equilibrium supports the notion that delta formation may continue to be prevented in such cases. Based on this observation, it is assumed that delta-formation has been entirely prevented under the given conditions in non-delta-forming simulations (although the equilibrium described is somewhat dependent on the constant-boundary approach taken here, and may differ under time-varying conditions). Furthermore, while this assumption may or may not extend to the up-to-millennial timescales of many real deltas, we argue that prevention of delta-formation within multi-decadal timescales—in comparison to the relatively rapid formation seen in lower marine-energy simulations—is in itself a strong enough effect to be classifiable as "prevention". This designation is meaningful insofar as it is of use in guiding human response to the future development of coastal systems into which rivers discharge.

5.1.1 Domain and grids

The model domain is shown in Figure 5.4. The FLOW domain comprises: a 19.75 km alongshore × 9.00 km cross-shore basin with a regular grid size $\Delta x = \Delta y = 25$ m; and a (1D) river of 50.0 km length × 0.25 km width, with regular grid size $\Delta x_r = \Delta y_r = 250$ m. The FLOW basin domain is nested in a larger WAVE domain with alongshore dimension 39.75 km × cross-shore dimension 10.00 km, and with regular grid size $\Delta x_w = \Delta y_w = 50$ m. The wide margins in the WAVE domain are included to prevent shadow regions at the lateral WAVE boundaries from affecting the FLOW domain.

This setup allows sufficient space for the deposited sediment mass to develop in most simulations without reaching the outer boundaries. The 25 m × 25 m FLOW resolution is deemed fine enough to minimise the issue of channel grid-alignment which often occurs with rectilinear grids (Baar et al., 2019), including in our own tests of larger grid sizes (see §4.1).

WAVE additionally requires specification of spectral grids in both the directional and frequency spaces. Here we define 24 logarithmically-spaced bins in frequency space ranging from 0.05 Hz to 1.00 Hz, and 18 directional bins oriented at 5° intervals between $\pm 45^\circ$ from shore-normal. This setup is sufficient to capture the predominantly shore-normal directed wave energy flux (see boundary setup –

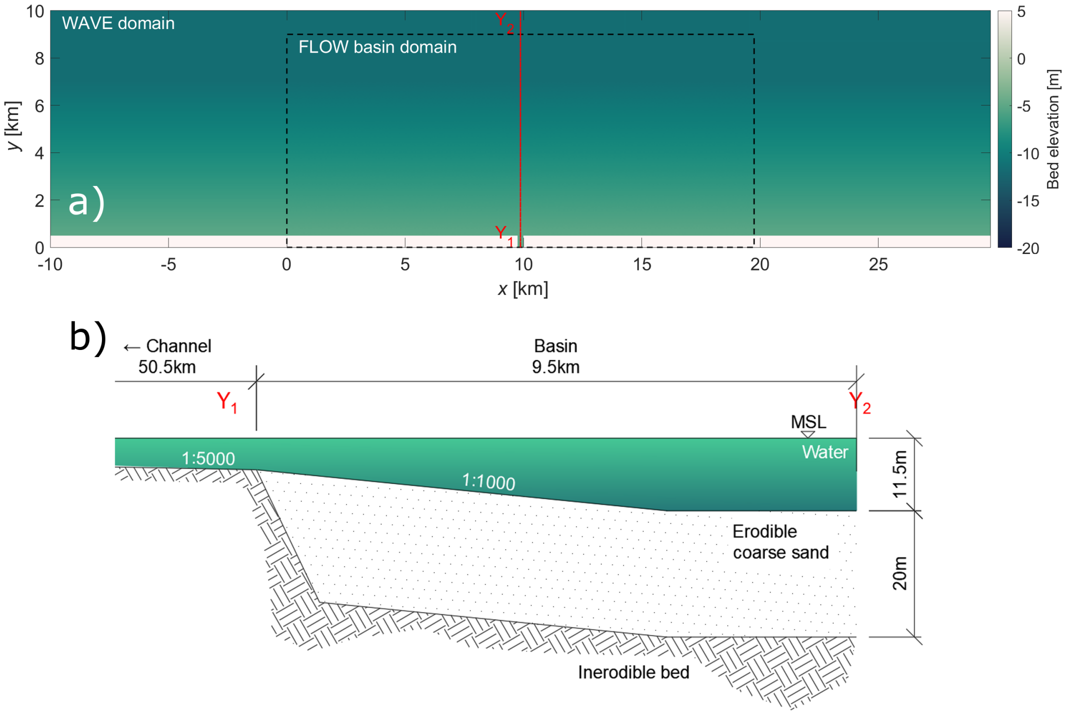

Figure 5.4: Initial basin bathymetry and domains used in all simulations. Full channel not shown. a) Plan-view of initial basin, with FLOW basin domain enclosed by black dashed line. Red dashed line indicates location of transect Y_1–Y_2. b) Transect Y_1–Y_2, showing sketch of channel and basin slope and erodible coarse sand layer. Water level shown at mean sea level (MSL). Note that the vertical axis is exaggerated by a factor of 100.

§5.1.3), but does incur small artificial losses of wave energy where refraction would lead to wave energy flux being transferred from the outermost directional bins toward angles $> 45°$ from shore-normal (which may happen as the bed evolves). However, sensitivity tests showed negligible differences in morphodynamic development between simulations with a directional grid as described above, and a full $360°$ grid with 72 directional bins of $5°$.

5.1.2 Initial bathymetry

All simulations start from the same initial bathymetry (see Figure 5.4). The basin has bed level -5 m at Y$_1$ nearshore (relative to mean sea level) decreasing to -11.5 m at Y$_2$ offshore with a transitional slope of 1:1000. This -11.5 m bed level is maintained in the most offshore 3 km strip of the basin ($y = 7000$ m to 10000 m). Additionally, random perturbations with a uniform distribution from 0 m to -0.05 m are applied throughout the basin. The basin itself is also partially erodible; a layer of up to 20 m thickness of coarse sand ($D_{50,c} = 1$ mm) is available throughout, starting from 0 m layer thickness adjacent to the initial coastline and increasing linearly to a layer thickness of 20 m over a distance of 1 km ($y = 500$ m to $y = 1500$ m, see Figure 5.4b). The 20 m layer thickness is maintained offshore from this point. A 500 m wide, 20 m high strip of the same coarse sand is added along the bottom edge of the basin, delineating the initial coastline.

This schematised bathymetry is considered to represent the inner region of a shelf sea into which rivers commonly discharge. The 1:1000 slope of the initial basin is of relatively low steepness for nearshore slopes globally (Athanasiou et al., 2019), but is steeper than often seen in comparable numerical modelling studies of deltas, where slopes often range between 1:2000 and 1:5000 (e.g. Edmonds and Slingerland, 2010; Burpee et al., 2015; Guo et al., 2015; Zhou et al., 2020). The choice of a relatively gentle 1:1000 slope (with respect to real nearshore slopes) is partially a compromise to allow for faster morphological development, as this reduces the accommodation space within the basin. This allows for sediment to spread over a larger area in a reduced length of time, reducing the computational expense of the simulations.

The feeder channel exists primarily to deliver water and sediment to the basin. The channel has slope 1:5000 and a total initial length of 50.5 km. This length is imposed in order to allow for tidal inundation and related discharge attenuation of the river in tidal simulations. (Were tides able to propagate to the discharging boundary, the constant discharge boundary condition would become unrealistic.) The bed of the channel is inerodible so as to ensure precise control of—and parity between—mean sediment fluxes from the channel into the basin between simulations. The slope and 1D configuration of the channel are chosen so as to prevent sediment deposition within the channel, also helping to ensure parity of sediment fluxes. Additionally, this approach prevents second-order effects of tidally-influenced river-braiding or similar phenomena from affecting depositional morphologies within the basin, allowing for observed morphological differences to be related purely to first-order wave and tidal effects on basin morphodynamics.

5.1.3 Boundary conditions

While a constant boundary approach has generally been adopted throughout the simulations described here (offshore tidal boundaries are somewhat of an exception as these are harmonic and hence quasi-constant), the differences between constant boundaries and equivalent temporally varying ones are potentially large (see e.g. Guo et al., 2015; Gao et al., 2018, 2019, for some discussion of temporal variation of boundaries). While temporally varying boundary conditions may produce morphologies that more closely resemble those of real coasts and deltas, such a setup introduces a significant level of complexity around the interpretation of process interaction, depending on, for example, whether peaks occur concurrently or in alternating patterns. This would make the interpretation of the developmental effects of each process more difficult to discern. As such, the use of a constant boundaries is argued here to be appropriate, as it allows for easier inference of the ways in which individual processes affect morphological development.

5.1.3.1 FLOW – Hydrodynamic boundaries

River discharge $Q_0 = 1280$ m^3 s^{-1} is imposed at the head of the river, using a temporally unvarying Dirichlet discharge boundary. At the lateral edges of the basin, Neumann boundaries are applied with respect to free surface elevation ζ, set to give boundary-normal gradients of $\partial\zeta/\partial x = 0$. Offshore, harmonically varying Riemann invariant boundaries are applied with period $T_t = 12.5$ hr and with amplitudes chosen to give the desired tidal range.

An alongshore propagating tidal wave may be expected to produce slightly different outcomes to the cross-shore propagating one. However, Geleynse et al. (2011) noted that the differences between cross-shore and alongshore propagating tides (with $H_t = 3$ m) with respect to delta development were remarkably small in their simulations. The same is assumed to be true here.

5.1.3.2 FLOW – Sediment transport boundaries

Fluvial sediments enter the model domain at the head of the feeder channel. This is achieved by setting a fine sediment ($D_{50,f} = 0.125$ mm, $\rho_s = 2650$ kg m^{-3}) mass concentration $\bar{c}_{mass} = 0.1$ kg m^{-3}. Suspended sediment concentration at all remaining boundaries is set to $\bar{c}_{mass} = 0.0$ kg m^{-3}. The model setup is such that bedload fluxes into the domain are nil or negligible at all boundaries.

5.1.3.3 WAVE – Wave spectrum boundaries

Where waves are modelled, these are generated at the offshore boundary of the WAVE grid using a JONSWAP spectrum with peak enhancement factor $\gamma_0 = 3.3$, peak period $T_p = 5$ s, shore-normal mean direction of propagation, and $\cos^{16}$ directional spread (Roelvink and Reniers, 2011; Deltares, 2021b). Selection of $T_p = 5$ s is partially for comparability to previous studies, where this value has commonly been used (e.g. Geleynse et al., 2011; Lageweg and Slangen, 2017; Gao et al., 2019; Liu et al., 2020; Broaddus et al., 2022), and partially based on wave data from Mangor et al. (2017). Selection of $\cos^{16}$ wave spreading followed sensitivity testing of a range of exponents, as discussed in §4.5. All other boundaries in the WAVE-domain are closed—i.e. wave spectral density is zero.

5.1.4 Model computation and performance

Each 36 yr simulation is designed to run on a high-performance computing (HPC) cluster. The FLOW domain is subdivided into 19 cross-shore-spanning subdomains in the basin, in addition to one subdomain representing the feeder channel. Each of these 20 domains is run in parallel using one logical processor of the University of Nottingham's HPC cluster. This represents a so-called manual domain decomposition method (see Deltares, 2021a), which is required in order to allow for the differences in grid-size between the channel and basin (see §5.1.1)[1]. The noted 36 yr duration of the simulations represents the simulated length of morphodynamic development, taking the morphodynamic acceleration factor, $f_m = 175$, into account. The unaccelerated duration is in fact 75 days ($(75/365) \times 175 \approx 36$ yr), in addition to a 50 hr "spin-up" period, during which morphodynamic development is disabled. For the selected timestep, $\Delta t = 9$ s, this equates to a total of 740000 time steps per simulation. Additionally, for the given FLOW-WAVE coupling period of 30 min, WAVE is run a total of 3601 times per simulation. Set up in this way, each 36 yr simulation takes between 5 and 7 days to run on the HPC cluster.

5.2 A systematic approach to defining and hence identifying deltas

One possible reason for the lack of investigation of the limits of delta development is the absence of a consistent, precise, and uniformly adopted definition of what a river delta actually is, which can make their identification difficult in ambiguous cases (see §2.2). A common simple definition is that a delta is any mass of sediment deposited where a river discharges that is both contiguous and partially emergent

---

[1] The manual domain decomposition method also notably ran around 40% faster than equivalent simulations using an automatic domain decomposition method during testing. The reasons for this were not clear, but appeared to relate to an inefficient allocation of subdomains using the automatic method, whereby more than double the number of grid connections (typically) existed between subdomains; the increased simulation run time perhaps relates to the need to pass more information between processors during model runs.

at low tide (Galloway, 1975; Wright, 1985; Caldwell et al., 2019; Syvitski et al., 2022a). This definition is appealing for its simplicity, but is here considered too imprecise to make a realistic determination of which morphologies are or are not deltas in ambiguous cases. As such, two additional, systematic criteria are defined here for identifying deltas with respect to regions of emergent sediment: firstly, that such regions should lie inland of the shoreline rather than form isolated bars or islands offshore (a distinction that requires a methodology for identifying said shoreline and hence distinguishing between such areas—see below); and secondly, that such regions should be incised by active channels (where "active" means that water in a given channel has a non-zero residual, i.e. tidally-averaged, current), extending from the initial river.

In order to classify morphologies as deltas following the above criteria, the locations of low tide lines must first be identified. To this end, the opening angle method (OAM) is used (Shaw et al., 2008). The OAM is applied here with a depth threshold $h_c = 0.11$ m to delineate wet vs. dry cells, and threshold opening angle $\phi_c = 70^\circ$ to define the location(s) of low tides lines (see §4.6.2). For consistency, the locations of high tide (shore)lines and perimeter of the deposited sediment mass are also identified using the OAM. For the sediment mass perimeter, a bed level change threshold $\Delta z_c = 0.25$ m is used (see §4.6.3).

Actively channelised cells within the low tide area are identified as those exceeding both a characteristic depth and velocity threshold. Here we adopt a mid-tide depth threshold $h_{c,mid} = (H_t/2) + 0.5$ m, and residual velocity threshold $\bar{u}_c = 0.2$ m s^{-1}. The selected value of $h_{c,mid}$ is guided by the logic employed by van der Vegt et al. (2016), in that the minimum depth of 0.5 m (at low tide) would give a minimum width-to-depth ratio of 50 for our basin grid-size $\Delta x = \Delta y = 25$ m. This seems a reasonable cut-off for distinguishing channel flow from sheet / overland flow. The selected value of $\bar{u}_c$ is chosen to allow for a degree of tidal asymmetry within a given (inactive) channel or network of channels, as well as expected slight differences in flow-routing between ebb and flood within those same channels. Both of these effects may result in small residual velocities occurring in channels through which river discharge is not being routed. We consider an active channel network to be present when the total area of such cells exceeds 0.2 km^2.

In summary, we identify a delta as having formed when:

1. a contiguous mass of sediment is deposited near the river mouth;
2. part of this deposited sediment mass emerges above water at low tide (above local water level for non-tidal cases);
3. at least one area defined by applying the OAM to the emergent deposit(s) adjoins the initial coastline; and
4. active channels, extending from the initial river, are incised into the region defined by (3).

Where all of the above are true, we classify the entire mass of deposited sediment to be a delta, and the region circumscribed by the low tide shoreline and initial coastline as the delta plain.

The above represents one systematic method by which deltas might be identified, but it is acknowledged that we may in some circumstances classify (or reject) certain morphologies as deltaic which might be classified differently under alternative definitions.

5.3 Morphodynamic metrics for quantifying delta development

Various metrics are defined in order to quantify aspects of morphodynamic development in the simulations presented. These relate to: overall morphodynamic activity; the number of channel splits occurring; mobility of channels within deltas; and the distribution of deposited sediments. For comparability of results, we analyse all metrics over intervals equal to tidal period $T_t = 12.5$ hr regardless of whether tides are modelled in a given simulation. Schematics illustrating each morphodynamic metric can be seen in Figure 5.5.

As a measure of overall morphodynamic activity in a simulation, we define non-dimensionalised excess mobility number χ [-] (Figures 5.5a to c), which quantifies the degree of sediment remobilisation per tide throughout the domain. This is defined as:

$$\chi\left(t\right) = \frac{\sum_{i=1}^{M}\sum_{j=1}^{N}|\Delta z_{i,j}^{-}\left(t\right)|}{f_z}$$

where $\sum_{i=1}^{M}\sum_{j=1}^{N}|\Delta z_{i,j}^{-}(t)|$ is the sum of magnitudes of all negative bed level changes per tide at time t [m]; M, N are the number of cells in the x and y directions respectively of the FLOW basin grid; and $f_z = Q_{sed}\rho_s T_t f_m/\rho_{bulk}\Delta x\Delta y$ [m] is a normalisation factor representing the expected net bed level increase per tide, assuming 100% deposition in the basin and no remobilisation of sediment.

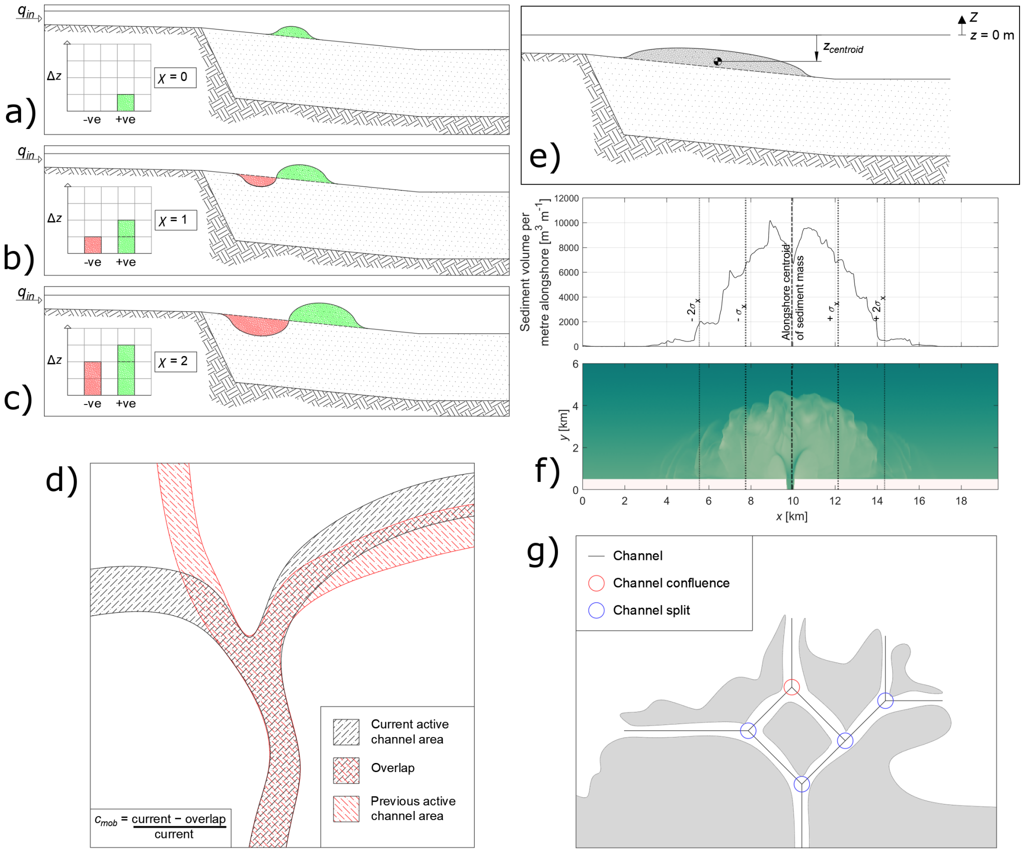

Figure 5.5: Schematics representing each of the morphodynamic metrics outlined in this section. Excess mobility for: a) $\chi = 0$ (no sediment mobilised in model); b) $\chi = 1$ (equal amount of sediment mobilised within model as enters model); and c) $\chi = 2$ (double the amount of sediment mobilised within model as enters model). d) c_{mob}: example showing current channel network against network one tide prior; e) z-centroid elevation: schematic indicating example centroid elevation (note upward positive convention); f) sediment spreading σ_x: example simulation bathymetry and plot of alongshore sediment volume, with dash-dotted lines indicating centre of deposited sediment mass, and dotted lines indicating $\pm$ 1 and 2 σ_x; g) channel split count c_{split}: example channel network with confluences and splits shown – c_{split} is counted as the total number of splits, ignoring confluences.

Where $\chi = 0$, this implies that no sediment has been remobilised within the domain. A χ-value of 1 implies that a volume of sediment has been moved within the domain which is equal to the volume of sediment entering the domain in the period of time considered, i.e. 12.5 hr (one tidal period). Values of $\chi > 1$ imply a proportionally greater degree of remobilisation of sediment within the domain.

Additionally, we define χ_{inner}, the excess mobility number within the low tide shoreline only, in order to further distinguish whether morphodynamic change is occurring within or outside of the low tide area.

The channel network is characterised via two metrics: number of channel splits c_{split} [-] (Figure 5.5g), and channel mobility c_{mob} [-] (Figure 5.5d). Channel splits c_{split} are counted by first determining the active channel network according to the methodology described in §5.2. This channel network is then skeletonised, from which the number of branch-points (intersections of three or more channels) in the active network is counted (Tejedor et al., 2016). As we wish to count channel splits (i.e. bifurcations and avulsions) and not confluences (i.e. instances in which one or more channels recombine into a single channel), we subtract the number of regions wholly enclosed by surrounding channels from this count, under the logic that any such enclosed regions arise only as a result of a channel confluence. Channel mobility c_{mob} is determined from the fractional overlap of the active channel network over successive tides (van der Vegt et al., 2016). It is defined as the total area of currently active channel cells which were not active at the previous time interval, divided by the total area of currently active channel cells. Thus, $c_{mob} = 0$ indicates that the active channel network has not changed over successive tides, and $c_{mob} = 1$ indicates that the active channel network occupies an entirely different region than one tide previously.

Finally, as measures of the distribution of deposited sediments, we determine z-axis centroid elevations (Figure 5.5e) and alongshore standard deviations σ_x [km] (Figure 5.5f) of net volumetric change in the bed with respect to initial bathymetry.

Chapter 6

Results of numerical simulations

Table 6.1 shows times of delta formation following the methodology outlined in §5.2, and Figure 6.1 shows the morphology of most of our simulations after ~ 35.75 yr of development. In six of the 42 simulations, deltas did not form within 72 yr; an outcome which aligns well with the predictions made using Eq. (5.1) (Figure 5.2). Of the six simulations for which deltas were predicted unlikely to occur ($\pi_\Delta < 0.5$), one formed a delta (W1.6T5.0), four did not (W2.0T3.0, W2.0T4.0, W2.0T5.0, and W2.0T6.0), and one experienced a cycle between deltaic and non-deltaic morphology (W1.6T6.0; considered non-deltaic after 72 yr). Of the three simulations for which $\pi_\Delta \approx 0.5$, two produced deltas and one did not. Of the remaining 33 simulations, for which $\pi_\Delta > 0.5$, all produced deltas. Generally, larger waves delayed delta formation more than did larger tides.

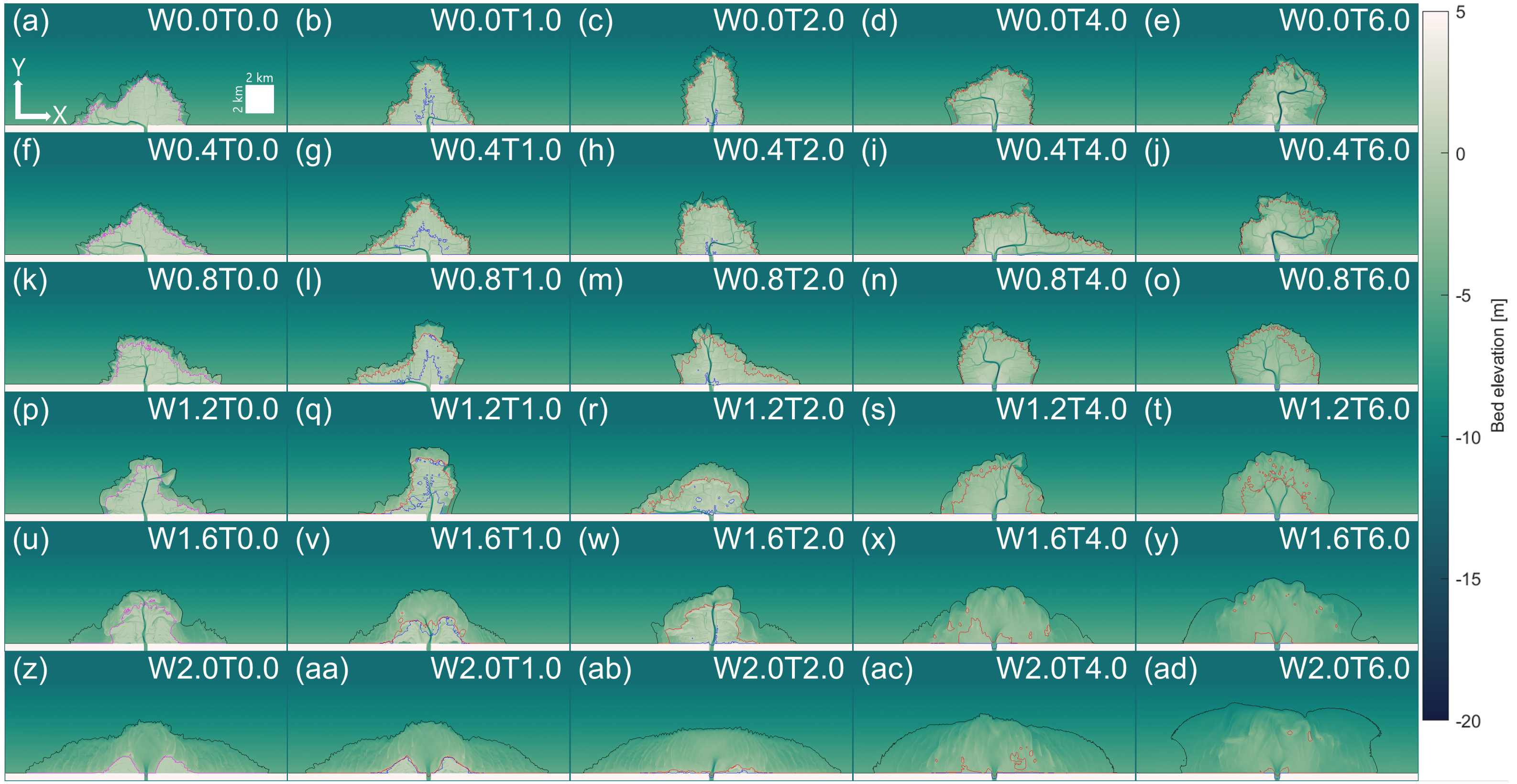

Figure 6.1: Selected bathymetries at $t \approx 35.75$ yr. Left to right: $H_t = 0.0$ m, 1.0 m, 2.0 m, 4.0 m, and 6.0 m. Top to bottom: $H_s = 0.0$ m, 0.4 m, 0.8 m, 1.2 m, 1.6 m, and 2.0 m. Black lines denote outer extent of sediment mass. Blue lines denote high tide shoreline or bar / island edges. Red lines denote low tide shoreline or bar / island edges. Magenta lines denote generic shoreline or bar / island edges in non-tidal simulations. Simulation IDs are shown on each subplot.

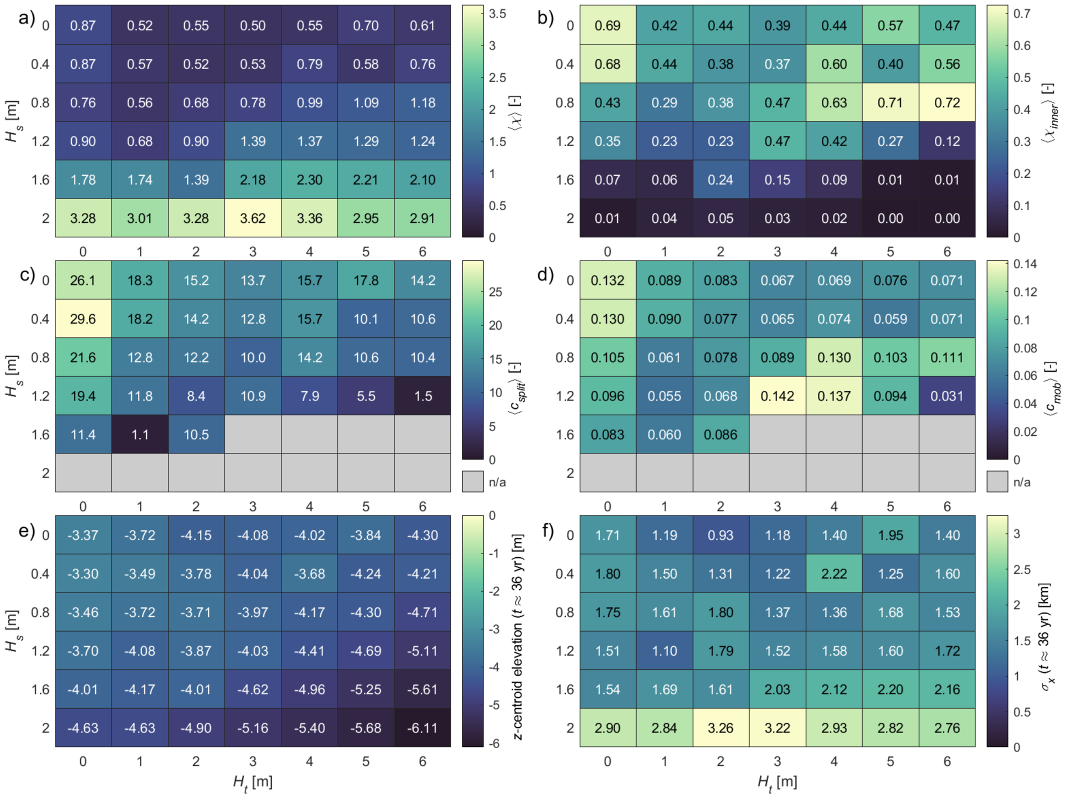

a)

H_s [m] \ H_t [m]	0	1	2	3	4	5	6
0	0.87	0.52	0.55	0.50	0.55	0.70	0.61
0.4	0.87	0.57	0.52	0.53	0.79	0.58	0.76
0.8	0.76	0.56	0.68	0.78	0.99	1.09	1.18
1.2	0.90	0.68	0.90	1.39	1.37	1.29	1.24
1.6	1.78	1.74	1.39	2.18	2.30	2.21	2.10
2	3.28	3.01	3.28	3.62	3.36	2.95	2.91

b)

H_s [m] \ H_t [m]	0	1	2	3	4	5	6
0	0.69	0.42	0.44	0.39	0.44	0.57	0.47
0.4	0.68	0.44	0.38	0.37	0.60	0.40	0.56
0.8	0.43	0.29	0.38	0.47	0.63	0.71	0.72
1.2	0.35	0.23	0.23	0.47	0.42	0.27	0.12
1.6	0.07	0.06	0.24	0.15	0.09	0.01	0.01
2	0.01	0.04	0.05	0.03	0.02	0.00	0.00

c)

H_s [m] \ H_t [m]	0	1	2	3	4	5	6
0	26.1	18.3	15.2	13.7	15.7	17.8	14.2
0.4	29.6	18.2	14.2	12.8	15.7	10.1	10.6
0.8	21.6	12.8	12.2	10.0	14.2	10.6	10.4
1.2	19.4	11.8	8.4	10.9	7.9	5.5	1.5
1.6	11.4	1.1	10.5				
2							

d)

H_s [m] \ H_t [m]	0	1	2	3	4	5	6
0	0.132	0.089	0.083	0.067	0.069	0.076	0.071
0.4	0.130	0.090	0.077	0.065	0.074	0.059	0.071
0.8	0.105	0.061	0.078	0.089	0.130	0.103	0.111
1.2	0.096	0.055	0.068	0.142	0.137	0.094	0.031
1.6	0.083	0.060	0.086				
2							

e)

H_s [m] \ H_t [m]	0	1	2	3	4	5	6
0	-3.37	-3.72	-4.15	-4.08	-4.02	-3.84	-4.30
0.4	-3.30	-3.49	-3.78	-4.04	-3.68	-4.24	-4.21
0.8	-3.46	-3.72	-3.71	-3.97	-4.17	-4.30	-4.71
1.2	-3.70	-4.08	-3.87	-4.03	-4.41	-4.69	-5.11
1.6	-4.01	-4.17	-4.01	-4.62	-4.96	-5.25	-5.61
2	-4.63	-4.63	-4.90	-5.16	-5.40	-5.68	-6.11

f)

H_s [m] \ H_t [m]	0	1	2	3	4	5	6
0	1.71	1.19	0.93	1.18	1.40	1.95	1.40
0.4	1.80	1.50	1.31	1.22	2.22	1.25	1.60
0.8	1.75	1.61	1.80	1.37	1.36	1.68	1.53
1.2	1.51	1.10	1.79	1.52	1.58	1.60	1.72
1.6	1.54	1.69	1.61	2.03	2.12	2.20	2.16
2	2.90	2.84	3.26	3.22	2.93	2.82	2.76

Figure 6.2: Heat-maps of all morphodynamic metrics up to $t \approx 36$ yr for all simulations: a) 0–36 yr temporal means of χ; b) 0–36 yr temporal means of χ_{inner}; c) temporal means of instantaneous c_{split}; d) temporal means of c_{mob}; e) z-centroid elevations with respect to MSL at $t \approx 36$ yr; and f) σ_x values at $t \approx 36$ yr. Note that both channel split counts and channel mobility numbers and means are calculated only from the point of delta formation up to $t \approx 36$ yr. Grey blocks in (c) and (d) are those for which no data exists, as deltas (and hence delta channels) did not form within the ~ 36 yr period covered.

Table 6.1: Time of Delta Formation for all Simulations [yr].

		H_t [m]						
		0.0	1.0	2.0	3.0	4.0	5.0	6.0
H_s [m]	0.0	2.75	1.75	2.00	2.00	1.50	1.50	2.00
	0.4	3.25	3.50	2.25	2.25	2.00	1.50	2.00
	0.8	5.50	6.50	7.50	6.50	11.00	11.50	3.50
	1.2	8.00	9.00	23.50	18.00	19.00	21.50	23.50
	1.6	24.50	33.75	20.00	39.75	62.75	54.75	n/a
	2.0	67.25	51.25	n/a	n/a	n/a	n/a	n/a

Note. In some cases, morphologies fluctuate between meeting and not meeting the criteria for classification as a delta. In these cases, delta formation time is defined as that at which the criteria are satisfied without subsequently returning to a non-deltaic configuration. All times are given to nearest 0.25 yr.

6.1 Delta formation without waves or tides

Without the influence of waves or tidal variation, delta development is controlled only by interaction between river discharge and the growing mass of deposited sediment. Excess mobility $\langle \chi \rangle$ is higher for simulation W0.0T0.0 ($H_s = 0$ m, $H_t = 0$ m) than all tide-only simulations, but lower than most simulations with waves (Figure 6.2a). The morphodynamic metrics $\langle \chi_{inner} \rangle$, $\langle c_{split} \rangle$ and $\langle c_{mob} \rangle$ are all amongst the highest measured for simulation W0.0T0.0 in comparison to all other simulations (Figures 6.2b, c, and d). W0.0T0.0 also gives some of the highest values for $\langle c_{split} \rangle$ and $\langle c_{mob} \rangle$. This comparatively high degree of (internal) morphological reworking and channel network splits / mobility suggests a high frequency of bifurcations and avulsions, an apparent result of the absence of external forcing from marine sources. The mechanisms explaining this (and other delta formation processes) are discussed in Chapter 7.

6.2 The effects of waves alone on delta formation

In wave-only simulations, the principle effect of waves on delta development lies in delaying the initial time of formation (see Table 6.1). This delay results from two effects waves have on sediment transport: a first-order effect of wave-bed interaction, which increases magnitudes of both suspended load and bedload transport; and a second-order effect of transport resulting from currents induced by wave energy dissipation. At the discharging mouths of channels, sediments are transported further past the river mouth into the basin due to the former effect (delaying / preventing mouth bar formation), but are also deflected landward by the latter. This is a complex interaction, with outcomes depending on local depths, currents, wave heights, and the orientations of discharging channels with respect to the direction (and spread) of waves. The strength of these effects depends primarily on the height of the incoming waves; under increasing H_s, the submerged margins of the sediment mass become larger in area, and sediments deposited in this region are distributed more evenly (compare Figures 6.1a, f, k, p, u, and z). Under the largest waves simulated ($H_s = 2.0$ m), alongshore spreading of sediments is also increased (larger σ_x – Figure 6.2f). The strength of this wave-driven sediment reworking effect is also evidenced by the larger $\langle \chi \rangle$ values seen under increasing H_s (Figure 6.2a). As Q_{sed} is identical between all simulations, wider alongshore spreading represented by σ_x also implies a reduction in overall bed elevations, which is evident in the reduced centroid heights in comparison to increased σ_x values for larger H_s seen in Figures 6.2e and f respectively. Simulations W0.0T0.0 to W1.2T0.0 (Figures 6.1a, f, k, and p) all produce quite large values for $\langle \chi_{inner} \rangle$, $\langle c_{split} \rangle$, and $\langle c_{mob} \rangle$. We classify such deltas as "river-controlled" (see §7.1).

At the highest H_s values modelled without tides—simulations W1.6T0.0 (Figure 6.1u) and W2.0T0.0 (Figure 6.1z)—$\langle \chi \rangle$ increases greatly in comparison to the smaller H_s simulations (Figure 6.2a), and a different regime of morphological development is established. This regime involves the initial formation of coastline-adjacent emergent regions to either side of the river mouth with a wide estuarine region forming centrally, which then transitions to a delta as the estuary infills with sediment. We classify deltas forming in this way as "wave-controlled" (see §7.3).

6.3 The effects of tides alone on delta formation

Tides without waves show no inhibiting effect on delta formation. In all such simulations, a delta forms within 3 yr (see Table 6.1). Introduction of tides induces a modest decrease in both $\langle c_{split} \rangle$ and $\langle c_{mob} \rangle$ (Figures 6.2c and d) in comparison to W0.0T0.0. Excess mobility number $\langle \chi \rangle$ also initially reduces as H_t increases, but then rises slightly again under larger tides ($H_t = 5$ m and 6 m – Figure 6.2a). This reflects an initial stabilising effect of increasing H_t followed by a cycle of sediment deposition and remobilisation within the channel network as tidal discharges become larger. Where tides have this stabilising effect on the channel network, we classify delta development as "river / tide-controlled" (see §7.2).

6.4 The effects of combined tides and waves on delta formation

When including waves alongside tidal variation, the cyclical vertical "sweep" of tides combines with the sediment transporting effects of waves (both wave-induced stirring and currents induced by wave energy dissipation), leading to a pattern of deposition and remobilization of sediments throughout the intertidal zone, both within and between channels. This is reflected by the higher $\langle \chi \rangle$ values seen under larger combinations of H_t and H_s in Figure 6.2a. Broadly, this combination of waves and tides causes a wider spread of sediments and related lowering of bed elevations, evident in the lower z-centroids and increased σ_x values seen in Figures 6.2e and f as well as in the morphologies seen in e.g. Figures 6.1e, j, o, t, y, and ad. At combinations of moderate $H_s = 1.2$ or 1.6 m and smaller $H_t = 1$ or 2 m, spits and barrier islands can be seen (Figure 6.1q, r, v, and w). These are not clearly observable in simulations outside this approximate range of H_s and H_t, suggesting that barrier island and spit formation may be more prevalent under this combination of parameters. Notably, such features are also clearly visible in the Copper river delta, which was defined as wave / tide-dominated by Galloway (1975)—see Figure 2.3. At the highest combinations of H_s and H_t—e.g. simulations W1.6T6.0, W2.0T2.0, W2.0T4.0, and W2.0T6.0. (Figures 6.1y, ab, ac, and ad respectively)—this inhibiting effect is sufficient to prevent the formation of persistent deposits above low tide, and hence prevent delta formation from occurring within ~ 72 yr. This critical finding suggests that delta formation may indeed be prevented from occurring under sufficiently energetic marine conditions. We classify regimes in which delta formation is prevented as "wave / tide-suppressed" (see §7.5).

While combinations of the largest H_s and H_t modelled prevented deltas from forming, a further distinct regime of delta formation occurs at intermediate combinations—e.g. W0.8T4.0, W0.8T6.0, and W1.2T4.0 (Figures 6.1n, o, and s). In these simulations, marine conditions are not quite sufficient to prevent delta formation, but they are sufficient to provide the energy needed for morphology to remain highly active throughout the deposited sediment mass. This effect is evident in the quite high $\langle \chi \rangle$ values, very high $\langle \chi_{inner} \rangle$ values, and very high $\langle c_{mob} \rangle$ values (Figures 6.2a, c, and d respectively) seen for simulations W0.8T4.0, W0.8T5.0, W0.8T6.0, W1.2T3.0, and W1.2T4.0. We classify delta development of this type as "wave / tide-controlled" (see §7.4). Note that we also classify simulations W1.2T5.0, W1.2T6.0, W1.6T3.0, W1.6T4.0, and W1.6T5.0 as wave / tide-controlled (see Chapter 7), despite these simulations not having values of morphodynamic metrics in Figure 6.2 as described above. This is due to these latter simulations only forming deltas close to, or in some cases after, 36 yr. As such, the processes described are only briefly observed, if at all, within the 36 yr window covered by the morphodynamic analysis.

Chapter 7

Delta formation regimes and development processes

Several distinct regimes of delta development were identified in Chapter 6. Each simulation is categorised by regime in Figure 7.1a, based on their observed, qualitative development over time, as well as values of morphodynamic metrics in Figure 6.2. Additionally, Figure 7.1b plots the simulations according to the process-dominance framework of Nienhuis et al. (2015, 2018, 2020). Black dotted lines on Figures 7.1a and b show the dividing line between delta formation being likely or unlikely according to Eq. (5.1) (i.e. $\pi_\Delta = 0.5$) (Caldwell et al., 2019). This line proves to be remarkably accurate in identifying the threshold between the delta-forming and non-delta-forming simulations.

While there is a loose correspondence between the regimes defined here and the wave / tide / river-dominated classifications according to Figure 7.1b, some notable

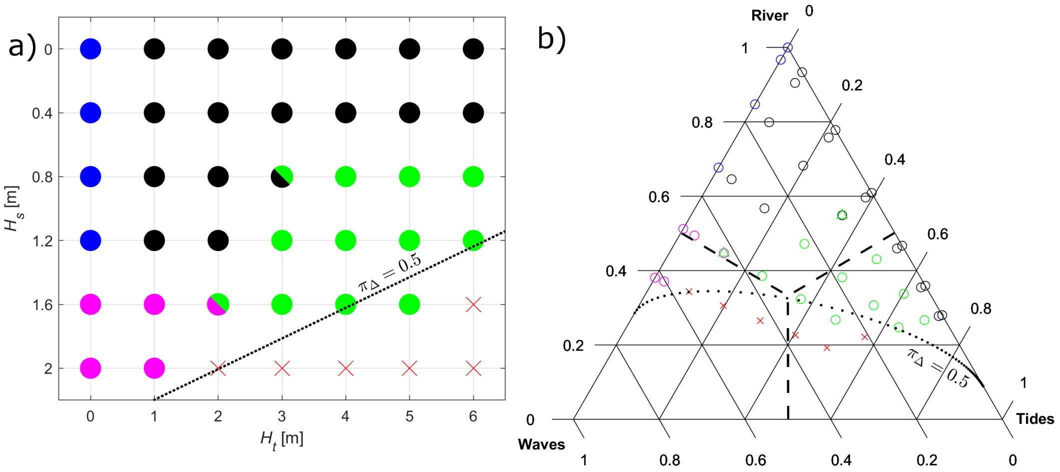

Figure 7.1: Delta regimes: magenta are wave-controlled; blue are river-controlled; black are river / tide-controlled; green are wave / tide-controlled; marks with two colours are unclear cases which lie between other regimes; red crosses are wave / tide-suppressed. Black dotted lines show the delimiting line between delta formation being considered likely or unlikely according to Eq. (5.1) (Caldwell et al., 2019), while maintaining $\langle Q_0 \rangle = 1280$ m^3 s^{-1} and $\langle Q_{sed} \rangle = 0.048$ m^3 s^{-1}. Presented are the classification of regimes by: a) H_s and H_t; and b) the methodology of Nienhuis et al. (2015, 2018, 2020) (this subplot produced in part using MATLAB code by Rik, 2024). Note that the relative influences in (b) are determined following the methodology of Nienhuis et al. (2015, 2018, 2020), using input parameters from the respective simulations rather than fluxes determined from simulation data. By Nienhuis's definitions, points in the lower left section are wave-dominated, lower right section are tide-dominated, and upper section are river-dominated. These sections are delimited by dashed black lines.

differences are apparent. Most significantly, here we classify several simulations as river / tide-controlled, and some simulations as wave / tide-controlled, which fall within the river-dominated classification of Figure 7.1b. By way of explanation, it is first noted that process-dominance according to the methodology of Nienhuis et al. (2015, 2018, 2020) is determined via a characteristic sediment transport associated with river discharge, tidal prism, or alongshore wave transport, each of which are treated independently. By contrast, our own regime classifications follow the semi-quantitative analysis presented in this chapter, for which the interaction between processes also has a significant effect on morphodynamic development—tides in particular have a greater effect on formational processes resulting from the interaction between water level variation and river discharge / wave-driven transport, than directly resulting from the transportive capacity of the tidal prism. This is not a novel observation; Orton and Reading (1993) described tidal variation as a mechanism for 'distributing' the energy of waves over larger portions of the beach and inner surf zone, noting that tides have negligible effect in shaping coastal morphologies where high energy waves are dominant.

Note that none of the simulations presented here are defined as purely tide-controlled, as it was generally found that it is the noted interaction of tides with other processes which determines the mechanisms of delta development. It should also be acknowledged, however, that the local geological setting might also affect the relative importance of tidal effects. Here, we have modelled delta formation in an open coastal setting; however, deltas forming within a laterally constrained, "drowned river valley" environment, might exhibit developmental processes with a more explicit tidal morphological signature (such as described by, e.g. Galloway, 1975; Orton and Reading, 1993). While the effort to define quantitative, deterministic measures of the influence of these primary processes on delta formation (or inhibition) is a reasonable one, such quantification might be improved by deriving characteristic transport equations which take process interaction into account.

Based on developmental laws outlined by Wolinsky et al. (2010), we expect that deltas in the river-controlled and river / tide-controlled regimes would exhibit similar ongoing development were their durations to be extended beyond 36 yr. At larger wave heights—particularly in the wave / tide-controlled regime—delta development matches these laws less clearly, hence the nature of continuing development beyond the durations modelled is less clear for these regimes (see Appendix C).

7.1 River-controlled delta formation

In river-controlled simulations, a mouth bar first forms within the discharging jet of the initial river mouth, leading to channel bifurcation and formation of a delta within 3 to 8 yr. Continuing delta growth is characterised by a combination of mouth-bar induced bifurcation at channel tips, as well as frequent avulsions where channels overtop their banks. The high $\langle \chi \rangle$ and $\langle c_{split} \rangle$ are indicative of how the avulsion process interacts with the overall very flat elevations of delta plains for these cases; where avulsions occur, they lead to an initial period of shallow overland flow over the flat delta plain. This flow subsequently resolves into multiple small channels, many of which quickly become inactive (Hoyal and Sheets, 2009).

The slight reduction in $\langle c_{split} \rangle$ and $\langle c_{mob} \rangle$ from simulation W0.0T0.0 to W1.2T0.0 (Figures 6.2c and d) is a consequence of both slower channel growth due to broader distribution of sediment by waves at channel ends (Ratliff et al., 2018), and also of the inhibiting effects of waves on mouth bar formation; this results in fewer channel splits as a result of mouth-bar induced bifurcation (Jerolmack and Swenson, 2007; Gao et al., 2018). Avulsion frequency is also reduced by slowing of mouth bar formation, as avulsion occurs primarily as a consequence of upstream-propagating effects of mouth bar formation on both hydro- and morphodynamics (Hoyal and Sheets, 2009; Edmonds et al., 2009).

7.2 River / tide-controlled delta formation

In contrast to purely river-controlled deltas, river / tide-controlled deltas have comparatively low $\langle \chi \rangle$, $\langle c_{split} \rangle$, and $\langle c_{mob} \rangle$ values (Figure 6.2a, c, and d). Simulations with $H_s \leq 0.8$ m have surface elevations ranging from around high tide water level close to the delta apex (here defined as the midpoint of the initial river mouth), down to (by definition) the low tide water level. This leads to steeper overall delta plain gradients under increasing values of H_t (compare Figures 6.1a to e and f to j). Tidal water level variation also affects the process of overland flow resolving into multiple channels as described by Hoyal and Sheets (2009), with avulsions appearing less frequent as H_t increases, resulting in the formation of fewer channels.

Compared to non-tidal simulations, tides also form deeper and wider deltaic channels, and also maintain (rather than infill) both active and inactive channels (Rossi et al., 2016; Zhou et al., 2020; Iwantoro et al., 2020; Broaddus et al., 2022), which in part explains the reduction in $\langle \chi \rangle$ and $\langle c_{mob} \rangle$. We observe no quantifiable change in mouth-bar induced bifurcation frequency for these simulations, with the majority of reduction in both $\langle c_{mob} \rangle$ and $\langle c_{split} \rangle$ (see top two rows in Figures 6.2c and d) apparently due primarily to the discussed reduction in avulsion frequency.

7.3 Wave-controlled delta formation

Wave-controlled delta formation in our simulations does not result from the processes of mouth-bar induced bifurcation and avulsion by which delta formation is typically explained. Instead, wave-controlled delta formation is characterised by development of an estuarine region which narrows to form a delta. This is a complex process which occurs as follows: mouth bar formation close to the river mouth is prevented by the higher-energy waves, with sediments transporting further past the river mouth to initially form a broad submerged fan. Within this fan, we see the formation of transverse (approximately shore-normal) bars with peak elevations at, or just below, the local water surface. Figure 7.2 shows an example of the development over time of one of these bars in simulation W2.0T0.0. Note the reduction in H_s from the offshore end of the bar to the nearshore end; this reduction indicates the dissipation of wave energy occurring along the bar, which translates into the observed shoreward-deflection of currents and related sediment fluxes. This shoreward sediment flux leads to sediment accumulation at the initial coastline, resulting in the formation and subsequent growth of the emergent deposits (strandplains) on either side of the river mouth, with a wide estuarine region forming centrally.

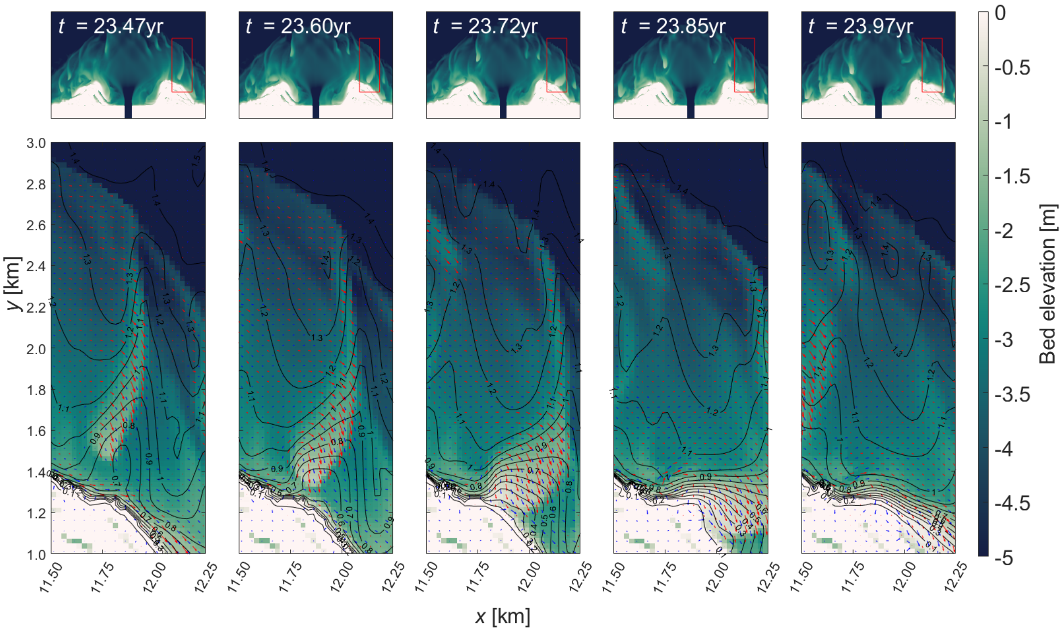

Figure 7.2: Time-series showing shore-normal bar migration and beaching for simulation W2.0T0.0. Bathymetry shown with: depth-averaged current vectors (blue arrows, shown at intersections of odd-numbered cells only); sediment transport vectors for total load (red arrows, shown at intersections of odd-numbered cells only); and labelled contours of H_s. Vector lengths are indicative of relative magnitude of their respective quantities only.

As the estuarine region grows over time, some of the bars beginning to form near the midline of the discharging jet are transported back into the estuary, rather than along the outer edges of the flanking deposits. An example of this process is represented in Figure 7.3. Here we see the shoreward end of a nascent bar spreading laterally to form a ridge normal to the mean incident wave direction. As the crest of the bar rises closer to the local water level, water currents and related sediment fluxes are diverted around the sides of the crest rather than over it. The resultant circulation around either side of the crest (Figure 7.3 panels 2 and 3) is enhanced by wave dissipation-induced currents on the up-wave side of the crest. The combined effect is that the forces driving this bar inward now exceed forces driving it outward, and the bar travels into the estuary, where it eventually stagnates (panel 5 of Figure 7.3). Repeated instances of this process lead to narrowing of the wide estuary towards a narrow channelised configuration, marking a transition from an open estuarine morphology towards a deltaic one.

While the idealised, steady boundary nature of the simulations may mean that the above-described process is not necessarily observable in reality, this development process does represent a potential novel mechanism of delta and estuary formation. This may have repercussions with respect to, for example, interpretation of the stratigraphic rock record where conducting field investigations into the development of deltaic and estuarine systems in historically micro-tidal, high wave energy regions.

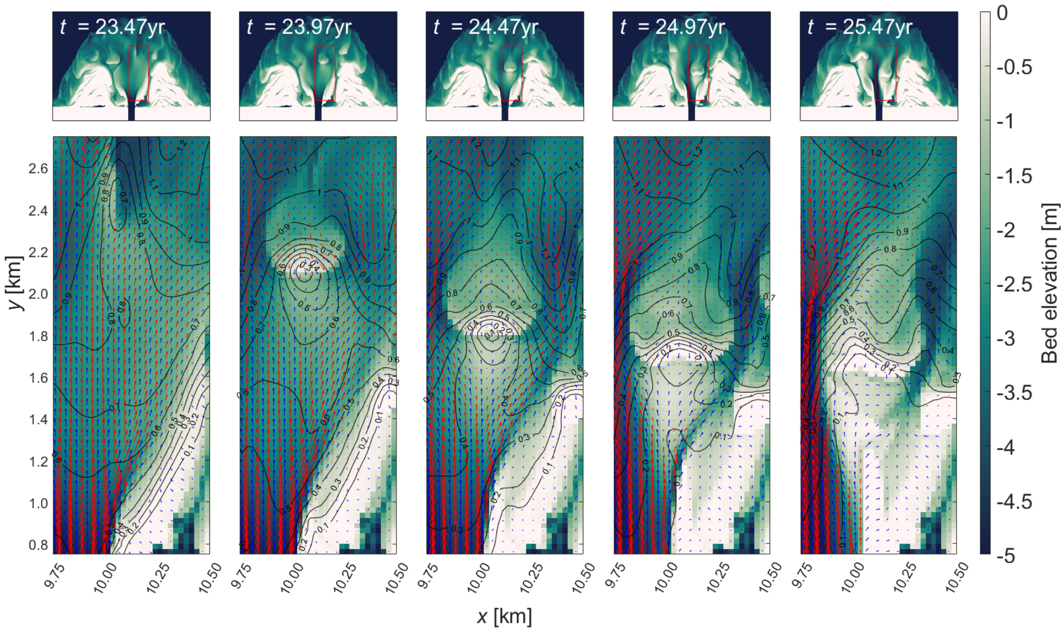

Figure 7.3: Time-series showing the process of bar transport into the estuary leading to estuarine infilling and transition to deltaic morphology for simulation W1.6T0.0. Bathymetry shown with: depth-averaged current vectors (blue arrows, shown at intersections of odd-numbered cells only); sediment transport vectors for total load (red arrows, shown at intersections of even-numbered cells only); and labelled contours of H_s. Vector lengths are indicative of relative magnitude of their respective quantities only.

7.4 Wave / tide-controlled delta formation

Wave / tide-controlled delta formation is marked by high values of $\langle \chi \rangle$, $\langle \chi_{inner} \rangle$, and $\langle c_{mob} \rangle$, but with lower $\langle c_{split} \rangle$ in comparison to river-controlled deltas (Figure 6.2a, b, c, and d). Most notably, the processes of mouth-bar induced bifurcation and, particularly, channel avulsion are less clearly observed in these cases. This is attributed to the high mobility of sediments throughout the delta, both inside and between channels. Mouth bars in these simulations shift their position over time alongside the highly mobile channels. This contrasts sharply with the relative immobility of such features when unaffected by either waves or tides; prior studies have demonstrated that, in such cases, mouth bars adopt an approximately fixed position once water depth at their crests reduces to a particular ratio (depending on local basin slope) relative to the surrounding local water depth (Edmonds and Slingerland, 2007; Jiménez-Robles et al., 2016). Avulsions, which were easily observable in lower marine-energy simulations, are still evident, but the combined processes controlling their development in these cases are difficult to disentangle.

7.5 Wave / tide-suppression of delta formation

Wave / tide-suppression of delta formation occurs when waves and tides in combination act to severely limit persistent deposits from accreting above the low tide water level. Simulations in which these conditions occurred are marked by alongshore bar transport oriented away from the discharging river mouth. While these bars are at times emergent, such emergence is typically short-lived, with bar crests returning to a fully submerged level as they travel alongshore. The movement of these bars is as described in §7.3, but marine conditions are such that accumulation of persistent emergent regions to either side of the discharging river no longer occurs. Critically, this observation suggests that—at least for the discharge conditions modelled—combined waves and tidal variation may indeed provide the conditions necessary for delta formation to be prevented.

7.6 Qualitative comparison of simulations with equivalent real world coasts for each formation regime

Here we provide comparison of five simulations—each representing one of the morphological regimes described in this chapter—with examples of rivers discharging to coasts featuring similar $\langle H_s \rangle$ and $\langle H_t \rangle$. Simulation bathymetries are presented alongside satellite imagery showing equivalent real river mouths in Figure 7.4. Key parameters for these five river mouths—as well as predicted delta likelihoods π_Δ (Eq. (5.1))—are summarised in Table 7.1. Comparisons for the wave / tide-controlled and wave / tide-suppressed categories were challenging to source, as the morphological areas of interest in such cases are generally within the intertidal range or fully submerged. As such, the characteristic markers of these regimes are typically not visible within satellite imagery. For the wave / tide-controlled case, we therefore selected a discharging river for which the submerged morphology was at least partially visible in satellite imagery (the Keum river in South Korea), and for which parameters matched as closely as possible those of the equivalent simulation.

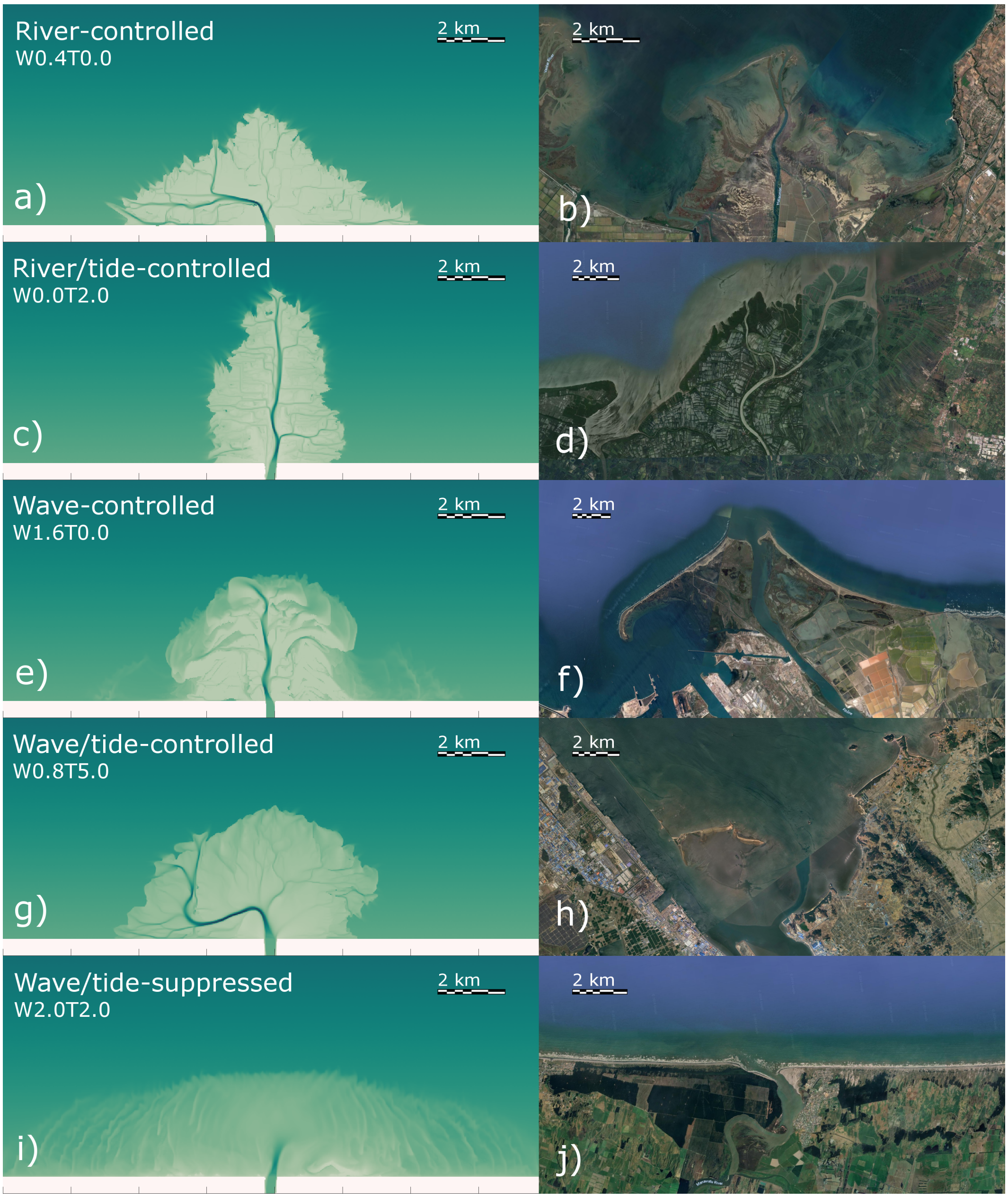

Figure 7.4: Selected simulation bathymetries at $t \approx 36$ yr and satellite images of coasts with similar $\langle H_s \rangle$ and $\langle H_t \rangle$. Shown are: a) W0.4T0.0; b) Haliacmon, Greece; c) W0.8T2.0; d) Porong, Indonesia; e) W1.6T0.0; f) Rhône, France; g) W0.8T5.0; h) Keum, South Korea; i) W2.0T2.0; and j) Manawatu, New Zealand. All satellite imagery taken from Google Earth 10.55.0.1 (2023a,d,e,b,c)

Table 7.1: Parameters and Delta Presence Probabilities for Rivers Shown in Figure 7.4.

River name	Equivalent simulation	$\langle H_s \rangle$ [m][a]	$\langle H_t \rangle$ [m][a]	$\langle Q_0 \rangle$ [m^3 s^{-1}][b]	$\langle Q_{sed} \rangle$ [m^3 s^{-1}][b]	π_Δ [-][c]
Haliacmon	W0.4T0.0	0.45	0.30	98.3	0.053	0.76
Porong	W0.0T2.0	0.18	2.32	380.5	0.074	0.78
Rhône	W1.6T0.0	1.62	0.26	1712.3	0.074	0.74
Keum	W0.8T5.0	0.81	4.74	133.2	0.026	0.48
Manawatu	W2.0T2.0	1.89	1.61	95.1	0.045	0.37

[a] Data from Caldwell et al. (2019).
[b] Data from Milliman and Farnsworth (2011).
[c] As calculated using Eq. (5.1) (Caldwell et al., 2019).
Note. Volumetric transports $\langle Q_{sed} \rangle$ are converted from mass transports (kg s^{-1}), assuming grain density $\rho_s = 2650$ kg m^{-3}.

7.6.1 Haliacmon – river-controlled

The Haliacmon delta (Figure 7.4b) shows evidence of frequent avulsions and low wave-driven transport by the presence of multiple long protrusions into the receiving basin. Numerous inactive (i.e. disconnected from the active channel network) narrow channels are visible throughout, evidencing the process of bank overtopping leading to shallow overland flow resolving to multiple channels, followed by abandonment. The rugose (i.e. rough or uneven) shoreline of the Haliacmon suggests the presence of a significant cohesive fraction (Orton and Reading, 1993; Caldwell and Edmonds, 2014), representing a "birds-foot" type morphology differing somewhat to that of the equivalent numerical simulation W0.4T0.0 (Figure 7.4a).

7.6.2 Porong – river / tide-controlled

The Porong (Figure 7.4d) exhibits a well-defined network of apparently active branching channels, as well as numerous channels which appear disconnected from the main network. Contrary to the Haliacmon, many of these channels do not appear to be abandoned, supporting the notion that tides act to maintain channel branches (Iwantoro et al., 2020). While the Porong delta has clearly been dominated by agri- and aquaculture, the natural meanders of the visible channels suggest that these were natural formations prior to their being (presumably) fixed in place by human development. These channelisation patterns appear broadly similar to the equivalent simulation W0.0T2.0 (Figure 7.4c). Also similar are the shape and scale of coastline features seen in each.

7.6.3 Rhône – wave-controlled

The most noticeable commonality between the Rhône delta (Figure 7.4f) and equivalent simulation W1.6T0.0 (Figure 7.4e) is the presence of long spits extending from the delta edges. A large bay is seen behind the left-side spit of the Rhône delta, and similar features are possibly developing to either side of the delta in simulation W1.6T0.0. It is not possible to infer the process of estuarine infilling from a single satellite image, but the similar shape and dominant central channel seen in both the Rhône and simulation W1.6T0.0 do not preclude this possibility.

7.6.4 Keum – wave / tide-controlled

The morphology surrounding the Keum river mouth (Figure 7.4h), comprises several square kilometres of tidal flats, into which channels are incised (while this cannot be inferred from inspection of Figure 7.4h, the presence of tidal flats separated by channels is observed and discussed by Kim et al., 2006). These broad tidal flats, and lack of high-tide-emergent sediment deposits, show some similarity with the equivalent simulation W0.8T5.0. Notably, Caldwell et al. (2019) do not classify the morphology surrounding the Keum river mouth as deltaic; however, the bathymetry here would likely meet our own criteria to be considered as such, due to the discussed presence of intertidal flats (low-tide-emergent regions of river-delivered sediment) into which channels are incised.

7.6.5 Manawatu – wave / tide-suppressed

The stretch of coast into which the Manawatu river (Figure 7.4j) discharges is remarkably smooth. In fact, several rivers discharge into this high wave energy coastline—the Õhau, the Rangitikei, the Whangaehu, and the Whanganui rivers—and all are marked by smooth, almost-straight shorelines. This suggests that sediments are bypassing the initial river mouth and being distributed evenly along the coast by the combination of waves and tides in this region, as in the equivalent simulation W2.0T2.0 (Figure 7.4i).

Chapter 8

Wave and tide driven sediment diffusion as a mechanism for inhibition of delta growth

While sediment transport is actually in part diffusive and in part advective, it is argued here that the overall pattern of spreading under combined tidal variation and larger shore-normal waves may be well approximated by a simple diffusive transport equation. It is assumed that sediment transport and bed elevation change can be described by an Exner (1925) equation of form:

$$\xi \frac{\partial z_b}{\partial t} = -\left\{ \frac{\partial q_x}{\partial x} + \frac{\partial q_y}{\partial y} \right\} + D - E \tag{8.1}$$

where z_b is bed elevation [m]; q_x, q_y are sediment fluxes per metre width in the x- and y-directions respectively [m^2 s^{-1}]; D (E) is deposition (erosion) rate per unit area [m s^{-1}]; and $\xi = 1 - n$ is a factor allowing for void-space in the bed [-]. For the large tidal ranges considered, sediment discharging from the river is generally deposited to the bed within the tidal cycle during which it enters. From that point onward, deposition and erosion of sediment remain in approximate equilibrium, as bed sediments are cyclically deposited and remobilized over successive tides. We hence simplify the analysis by stating that $D \equiv E$, thus eliminating those terms from Eq. (8.1). We also assume all subsequent sediment transport can be represented simply by the sediment flux terms q_x and q_y in Eq. (8.1), regardless of the actual mechanisms of transport—i.e. whether as bedload or suspended load. Integrating Eq. (8.1) in the cross-shore (y) direction:

$$\xi \int_0^{L_y} \frac{\partial z_b}{\partial t} dy = \frac{\partial V_s}{\partial t} \qquad \text{where } V_s\left(x,t\right) = \xi \int_0^{L_y} z_b\left(x,y,t\right) dy$$

is the total volume of river-delivered sediment per metre alongshore [m^2];

$$\int_0^{L_y} \frac{\partial q_x}{\partial x} dy = \frac{\partial Q_x}{\partial x} \qquad \text{where } Q_x\left(x,t\right) = \int_0^{L_y} q_x\left(x,y,t\right) dy \ [\mathrm{m^3\,s^{-1}}]\text{; and}$$

$$\int_0^{L_y} \frac{\partial q_y}{\partial y} dy = q_y\left(x,L_y,t\right) - q_y\left(x,0,t\right) = -q_y\left(x,0,t\right),$$

Eq. (8.1) becomes:

$$\frac{\partial V_s}{\partial t} = -\frac{\partial Q_x}{\partial x} + q_y\left(x,0,t\right). \tag{8.2}$$

Observing that the overall movement of bed sediments in such simulations is typically alongshore away from the river mouth, we assume that we can state $Q_x = -\kappa_d\left(x,t\right) \frac{\partial V_s}{\partial x}$, where κ_d is a coefficient of diffusion [m^2 s^{-1}]. This means that sediment will move down its own alongshore gradient, driven by gravity but also aided (or hindered) by additional agitation resulting from waves and currents. The coefficient κ_d can hence be viewed as quantifying the strength of this downslope sediment transport. It follows that Equation (8.2) may be written as:

$$\frac{\partial V_s}{\partial t} = \frac{\partial}{\partial x} \left\{ \kappa_d \left(x, t \right) \frac{\partial V_s}{\partial x} \right\} + q_y \left(x, 0, t \right) \tag{8.3}$$

where $q_y \left(x, 0, t \right) = Q_{sed}/W$ for $0.5 \left(L_x - W \right) \leq x \leq 0.5 \left(L_x + W \right)$ or $q_y \left(x, 0, t \right) = 0$ m^2 s^{-1} otherwise; W is the width over which incoming sediment flux Q_{sed} is distributed [m]; and L_x is the alongshore width of the domain [m]. Notionally κ_d represents a spatially and temporally varying alongshore bed diffusion coefficient, which is unknown. In contrast, W notionally represents the river width, which is fixed here and known. As a practical measure, we here set κ_d to be constant, which is to be fitted to the simulation data. To allow for the probable locally higher rates of diffusion in the vicinity of the river outflow, we also regard W as a fitting parameter. This is accordingly best viewed as representing the distributive capacity of the discharging jet of the river, which spreads sediments far beyond the vicinity of the river mouth independently of any additional diffusion resulting from wave / tide-induced transport represented by κ_d. It therefore seems reasonable to anticipate that the best-fit W would be substantially larger than the actual river width.

We derive an approximate solution of Eq. (8.3) (for constant κ_d) through the method of eigenfunction expansion (see e.g. Constanda, 2016): taking κ_d to be constant for all x and t, and defining initial conditions $V_s \left(x, 0 \right) = 0$ m^2 and

Neumann boundary conditions $\frac{\partial V_s(0,t)}{\partial x} = 0$ m^2 m^{-1} and $\frac{\partial V_s(L_x,t)}{\partial x} = 0$ m^2 m^{-1}, we define:

$$V_s\left(x,t\right) = \sum_{n=0}^{\infty} f_n\left(t\right) \cos\left(n\pi \frac{x}{L_x}\right); \text{ where} \tag{8.4}$$

$$f_n\left(t\right) = \begin{cases} t\frac{Q_{sed}}{L_x} & \text{for } n = 0 \\ \frac{\beta_n}{\alpha_n}\left[1 - \exp\left(-\alpha_n t\right)\right] & \text{for } n > 0; \end{cases} \tag{8.5}$$

and where $\alpha_n = \kappa_d \left(\frac{n\pi}{L_x}\right)^2$ and $\beta_n = \frac{2}{n\pi}\frac{Q_{sed}}{W}\left[\sin\left(\frac{n\pi}{2}\frac{L_x+W}{L_x}\right) - \sin\left(\frac{n\pi}{2}\frac{L_x-W}{L_x}\right)\right]$. This method is found to converge toward unique solutions at values of n of $\mathcal{O}\left(10\right)$, hence we apply it here in all cases with $n = 100$. Values of κ_d and W to be used in Eqs. (8.4) and (8.5) are determined—to the nearest 0.0005 m^2 s^{-1} and 250 m respectively—using a least-squares fit approach over both x and t. Predictions made using Eqs. (8.4) and (8.5) are compared to spatially and temporally smoothed bed level data (moving mean calculated over ± 2 km in x and $\pm T_t/2$ hr in t—i.e. over one tide at hydrodynamic timescale), iterating to determine the smallest root mean square error (RMSE) possible.

Best-fit values of κ_d and W, as well as related RMSEs, are shown in Table 8.1 for all wave-controlled, wave / tide-controlled, and wave / tide-suppressed simulations. Comparison between Delft3D data—for simulations W1.6T4.0, W1.6T6.0, W2.0T4.0, and W2.0T6.0—and predicted sediment distribution using Eq. (8.4) is shown in Figure 8.1. We do not apply Eq. (8.4) to either the river-controlled or river / tide-controlled cases; simulations for which the assumptions underpinning the validity of the formula do not hold. Sediment distribution in such cases is controlled primarily by intrinsic mouth-bar and avulsion channel splitting processes rather than extrinsic transport due to tidal variation and waves associated with greater H_s and H_t. Generally, the accuracy with which Eq. (8.4) matches the results of the Delft3D simulations increases with H_s, with the largest RMSEs in Table 8.1 occurring for simulations with $H_s = 0.8$ m and smallest RMSEs occurring for simulations with $H_s = 2.0$ m.

Broadly, values of W producing the closest fit for all non-delta forming simulations in Table 8.1 are ~ 5000–6000 m. Values of W reduce to around ~ 4000 m for simulations with $H_s = 0.8$ m, suggesting that waves also contribute somewhat to the initial spread of river-delivered sediments, independently of any background alongshore transport. This makes physical sense, as wave-stirring acts to reduce rates of deposition within the river jet(s), allowing sediments to initially spread further. As argued above, the magnitude of W is likely related primarily to the magnitude of river discharge; however, as river discharge parameters are not varied in the simulations presented here, no definitive statement to that effect is offered here.

Values of κ_d showed a dependence on H_s, with values as low as 0.002 m^2 s^{-1} for simulations with $H_s = 0.8$ m, increasing to as high as 0.0095 m^2 s^{-1} for simulations with $H_s = 2.0$ m. With the exception of simulations W2.0T0.0 and W2.0T1.0, all delta-forming simulations had best-fit $\kappa_d \leq 0.004$ m^2 s^{-1}, suggesting $\kappa_d = 0.004$ m^2 s^{-1} to be an appropriate first approximation as a lower boundary for the suppression of delta formation. Note that this limit is not considered to be generalisable to all discharging river / basin systems, as it may well also depend on discharge parameters and (initial) coastal morphology, which were not varied here. In general, best-fit κ_d-values showed a slight increase with increasing H_t.

Table 8.1: Values of κ_d, W, and Related RMSEs for all Wave-controlled, Wave / Tide-Controlled, and Wave / Tide-Suppressed Simulations.

H_s [m]	H_t [m]	Regime	κ_d [$\mathrm{m^2\,s^{-1}}$]	W [m]	RMSE [$\mathrm{m^3\,m^{-1}}$]	κ_{sde} [a] [$\mathrm{m^2\,s^{-1}}$]
0.8	0.0	-	-	-	-	0.0017
	3.0	RT/WT	0.0020	4250	7022	
	4.0	WT	0.0025	4000	7678	
	5.0	WT	0.0025	4000	6695	
	6.0	WT	0.0025	4250	7334	
1.2	0.0	-	-	-	-	0.0029
	3.0	WT	0.0025	4250	5123	
	4.0	WT	0.0025	4500	4949	
	5.0	WT	0.0025	4500	5054	
	6.0	WT	0.0030	4500	5035	
1.6	0.0	W	0.0025	4500	5525	0.0040
	1.0	W	0.0030	4250	5025	
	2.0	W/WT	0.0025	4750	7118	
	3.0	WT	0.0035	5000	4586	
	4.0	WT	0.0040	5000	5794	
	5.0	WT	0.0040	5000	5148	
	6.0	X	0.0040	5000	4623	
2.0	0.0	W	0.0075	5000	3139	0.0052
	1.0	W	0.0070	4500	4070	
	2.0	X	0.0095	5250	4810	
	3.0	X	0.0090	5750	4349	
	4.0	X	0.0070	5750	3930	
	5.0	X	0.0065	5500	4194	
	6.0	X	0.0060	5500	3745	

Note. W denotes wave-controlled; WT denotes wave / tide-controlled; X denotes wave / tide-suppressed; RT/WT denotes mixed river / tide and wave / tide-controlled; and W/WT denotes mixed wave and wave / tide-controlled.

[a] Diffusion coefficients determined for "shoreline diffusion" equation (see Appendix D)

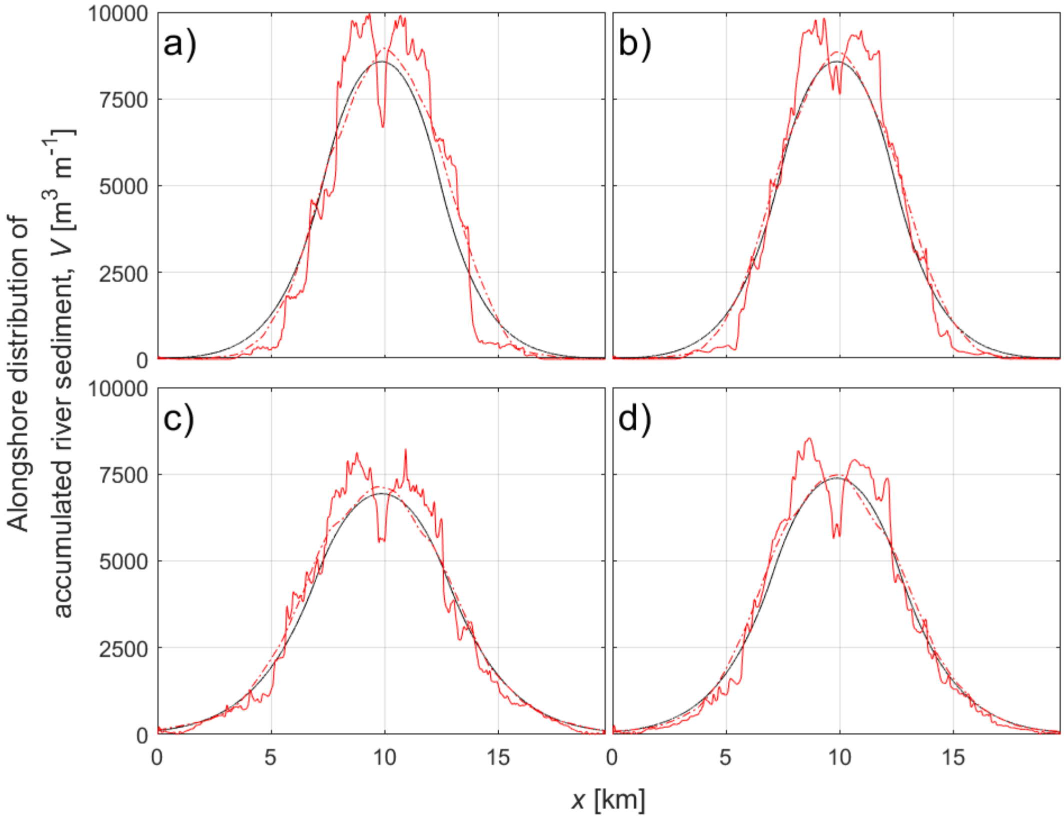

Figure 8.1: Plots of alongshore distribution of accumulated river sediment V_s (after ~ 36 yr, for (smoothed) Delft3D simulation data in comparison to approximate solutions (Eq. (8.4) with $n = 100$ and $L_x = 29750$ m). Black lines are approximate solutions, solid red lines are Delft3D simulation data, and dashed red lines are smoothed Delft3D data. Shown for: a) W1.6T4.0 ($\kappa_d = 0.004$ m^2 s^{-1}, $W = 5000$ m); b) W1.6T6.0 ($\kappa_d = 0.004$ m^2 s^{-1}, $W = 5000$ m); c) W2.0T4.0 ($\kappa_d = 0.007$ m^2 s^{-1}, $W = 5750$ m); and d) W2.0T6.0 ($\kappa_d = 0.006$ m^2 s^{-1}, $W = 5500$ m). (Note that x-coordinate shown relates to the convention of the Delft3D model; the x-coordinate of the analytical solution has been offset to match.)

However, this trend is not maintained for simulations with $H_s = 2.0$ m; here, κ_d reduces from a maximum 0.0095 m^2 s^{-1} for simulation W2.0T2.0, down to 0.006 m^2 s^{-1} for simulation W2.0T6.0. We attribute this effect to the tendency for larger H_t simulations to initially deposit sediments further offshore, as a result of faster ebb-tide currents (compare Figures 6.1ab to ad). Sediments deposited further offshore due to this effect are subject to reduced wave-driven remobilisation (as represented by excess mobility χ – Figure 6.2a), hence the observed reduction in κ_d. As a final note regarding κ_d, we also estimated diffusion coefficients for the analogous (wave-driven) "shoreline diffusion" equation (see e.g. Kamphuis, 2010, and Appendix D). The diffusions coefficients determined by this analysis are also shown in Table 8.1, and are broadly similar to those determined by the diffusion equation derived in this chapter.

Finally, it is noted that while Equation (8.4) was derived with delta non-formation cases in mind, it also performed well in replicating sediment distribution in the wave / tide-controlled and wave-controlled cases. Although RMSEs for the wave-controlled cases were amongst the lowest measured, we expect that Eq. (8.4) would prove less accurate if applied to those simulations over longer durations; following the onset of delta formation, sediment distribution would become increasingly determined by intrinsic (channel migration and avulsion-driven) rather than extrinsic (wave- and tide-driven) processes. The accuracy of Eq. (8.4) with respect to future development of wave / tide-controlled cases is less clear, as the projected balance of intrinsic and extrinsic drivers is harder to predict in such cases. This is in contrast to the expected development from primarily extrinsic to primarily intrinsic for the wave-controlled cases.

Chapter 9

Conclusions and recommendations

This thesis investigated whether delta formation could be suppressed by sufficiently large values of significant wave height H_s, and tidal range H_t. In doing so, larger combinations of these parameters were modelled than typically have been in previous studies. Four regimes of delta formation were identified: river-controlled; river / tide-controlled; wave-controlled; and wave / tide-controlled. A fifth regime, wave / tide-suppression of delta formation, occurred under combinations of the largest H_s and H_t of those tested (up to 2 m and 6 m respectively). The process-control classifications of this thesis were compared to the prevailing process-dominance framework of Nienhuis et al. (2015, 2018, 2020), and the suggestion made that their process-dominance framework might be improved by consideration of process interaction, especially as concerns tides. Higher wave and tidal energy regimes—i.e. wave-controlled and wave / tide-controlled formation regimes as well as wave / tide-suppression of delta formation—notably did not clearly exhibit the processes

Table 9.1: Magnitude of Morphodynamic Metrics Indicating Delta Regime.

	$\langle \chi \rangle$	$\langle \chi_{inner} \rangle$	$\langle c_{split} \rangle$	$\langle c_{mob} \rangle$	z-centroid[a]	σ_x
River-controlled	mid	high	high	high	high	-
River/tide-controlled	low	mid	mid	mid	-	-
Wave/tide-controlled[b]	high	high	-	high	-	-
Wave-controlled	high	low	-	-	low	high
Wave/tide-suppressed	high	low	-	-	low	high

[a] Here, 'low' and 'high' relate to the absolute elevation of the z-centroid.

[b] These values are not reflected in all such simulations in Figure 6.2, due to the late formation of deltas in these cases as compared to the 36 yr period over which metrics were evaluated.

of mouth-bar induced bifurcation and avulsion by which delta development under smaller waves and tidal ranges is often characterised (see e.g. Edmonds and Slingerland, 2010). Simulations designated here as wave-controlled do approximately match descriptions of strongly wave-affected 'cuspate' delta growth models described in some prior studies (e.g. Komar, 1973; Dominguez, 1996; Ashton and Giosan, 2011), but diverge from these studies in that they also exhibit an early formational phase wherein an initially wide estuarine region narrows to a single channel; a potentially novel formational process with repercussions for interpretation of the geological record. The approximate magnitudes of morphodynamic metrics associated with each regime are shown in Table 9.1 (dashes indicate that a particular morphodynamic metric is unimportant in identifying given regime).

Furthermore, mechanisms were identified by which waves and tides can potentially prevent delta formation altogether, and these aligned well with the predictions of Caldwell et al. (2019). In such cases, a diffusion equation with source term can be used to fairly accurately predict the alongshore spreading of sediment. We suggest that Eq. (8.3) is viable for predicting alongshore transport of discharging river sediment under approximately normally-incident, high-energy waves, at coasts which do not form deltas, and also those that form wave / tide-controlled deltas (by our proposed definitions). Such coastlines are often smooth and approximately straight (Anthony, 2015; Ratliff et al., 2018, – see also Figure 7.4j), and hence are reasonably well represented by the idealised simulations. While it is outside the scope of this thesis to do so, it seems plausible that κ_d and W in Eq. (8.4) might be explicitly defined as functions of H_s, wave spreading, mean wave direction, Q_0, and Q_{sed}. As a first approximation, a value of $\kappa_d = 0.004$ m^{2}s^{-1} is suggested as a boundary between delta formation and non-formation.

It is reasonable to wonder if delta formation would continue to be prevented over longer durations than modelled here, and for conditions other than those considered here. A more complete analysis would thoroughly consider the processes by which sediment is transported far from the river mouth, beyond the depositional region of the potential delta. This might occur under several conditions: where mean wave directions are not directly shore-normal, thus inducing ongoing littoral drift; where tidal asymmetry is significant; where tides and other oceanic processes induce alongshore currents sufficient to transport sediments away from the local depositional region; or even where sediments are transported as far as the continental shelf edge and are hence deposited into deep sea environments.

The description of lateral spreading of sediment embodied in Eq. (8.3) has a potential practical use in, for instance, the prediction of the possible effect of restricting sediment output due to upstream damming and other water management practices. If W and κ_d can be related to waves, tides and river discharge, then Eq. (8.3) can constitute the basis for an efficient method for determining the threshold for delta stagnation or destruction.

Bibliography

R. Allard, W. Rogers, S. Carroll, and K. Rushing. Validation test report for the simulating waves nearshore model (swan): Cycle iii, version 40.11. page 49, 09 2004.

B. Angamuthu, S. E. Darby, and R. J. Nicholls. Impacts of natural and human drivers on the multi-decadal morphological evolution of tidally-influenced deltas. *Proceedings of the Royal Society A: Mathematical, Physical and Engineering Sciences*, 474(2219):20180396, 2018. doi: 10.1098/rspa.2018.0396. URL `https://royalsocietypublishing.org/doi/abs/10.1098/rspa.2018.0396`.

E. J. Anthony. Wave influence in the construction, shaping and destruction of river deltas: A review. *Marine Geology*, 361:53–78, 2015. ISSN 0025-3227. doi: https://doi.org/10.1016/j.margeo.2014.12.004. URL `https://www.sciencedirect.com/science/article/pii/S0025322714003788`.

A. D. Ashton and L. Giosan. Wave-angle control of delta evolution. *Geophysical Research Letters*, 38(13), 2011. doi: https://doi.org/10.1029/2011GL047630. URL `https://agupubs.onlinelibrary.wiley.com/doi/`

abs/10.1029/2011GL047630.

P. Athanasiou, A. van Dongeren, A. Giardino, M. Vousdoukas, S. Gaytan-Aguilar, and R. Ranasinghe. Global distribution of nearshore slopes with implications for coastal retreat. *Earth System Science Data*, 11(4):1515–1529, 2019. doi: 10.5194/essd-11-1515-2019. URL https://essd.copernicus.org/articles/11/1515/2019/.

A. Baar, M. Boechat Albernaz, W. Van Dijk, and M. Kleinhans. Critical dependence of morphodynamic models of fluvial and tidal systems on empirical downslope sediment transport. *Nature Communications*, 10, 10 2019. doi: 10.1038/s41467-019-12753-x.

R. A. Bagnold. An approach to the sediment transport problem from general physics, 1966.

S. Bandyopadhyay. Evolution of the ganga–brahmaputra delta : A review. *Geographical review of India*, 69:235–268, 09 2007.

B. Bidorn. *Causes of shoreline recession in the Chao Phraya delta*. PhD thesis, Florida State University, 2016.

E. Bird. *Coastal Geomorphology: An Introduction*. Wiley, 2008. ISBN 9780470723968. URL https://books.google.co.uk/books?id=-YX0mWBpjGkC.

J. Bosboom, A. Reniers, and A. Luijendijk. On the perception of morphodynamic model skill. *Coastal Engineering*, 94:112–125, 2014. ISSN 0378-

3839. doi: https://doi.org/10.1016/j.coastaleng.2014.08.008. URL https://www.sciencedirect.com/science/article/pii/S0378383914001604.

C. M. Broaddus, L. M. Vulis, J. H. Nienhuis, A. Tejedor, J. Brown, E. Foufoula-Georgiou, and D. A. Edmonds. First-order river delta morphology is explained by the sediment flux balance from rivers, waves, and tides. *Geophysical Research Letters*, 49(22):e2022GL100355, 2022. doi: https://doi.org/10.1029/2022GL100355. URL https://agupubs.onlinelibrary.wiley.com/doi/abs/10.1029/2022GL100355. e2022GL100355 2022GL100355.

A. P. Burpee, R. L. Slingerland, D. A. Edmonds, D. Parsons, J. Best, J. Cederberg, A. McGuffin, R. Caldwell, A. Nijhuis, and J. Royce. Grain-Size Controls On the Morphology and Internal Geometry of River-Dominated Deltas. *Journal of Sedimentary Research*, 85(6):699–714, 06 2015. ISSN 1527-1404. doi: 10.2110/jsr.2015.39. URL https://doi.org/10.2110/jsr.2015.39.

R. L. Caldwell and D. A. Edmonds. The effects of sediment properties on deltaic processes and morphologies: A numerical modeling study. *Journal of Geophysical Research: Earth Surface*, 119(5):961–982, 2014. doi: https://doi.org/10.1002/2013JF002965. URL https://agupubs.onlinelibrary.wiley.com/doi/abs/10.1002/2013JF002965.

R. L. Caldwell, D. A. Edmonds, S. Baumgardner, C. Paola, S. Roy, and J. H. Nienhuis. A global delta dataset and the environmental variables that predict delta formation on marine coastlines. *Earth Surface Dynamics*, 7(3):773–787, 2019. doi: 10.5194/esurf-7-773-2019. URL https://esurf.copernicus.org/articles/7/773/2019/.

D. Calvete, N. Dodd, A. Falqués, and S. M. van Leeuwen. Morphological development of rip channel systems: Normal and near-normal wave incidence. *Journal of Geophysical Research: Oceans*, 110(C10), 2005. doi: https://doi.org/10.1029/2004JC002803. URL https://agupubs.onlinelibrary.wiley.com/doi/abs/10.1029/2004JC002803.

A. Canestrelli, W. Nardin, D. Edmonds, S. Fagherazzi, and R. Slingerland. Importance of frictional effects and jet instability on the morphodynamics of river mouth bars and levees. *Journal of Geophysical Research: Oceans*, 119, 01 2014. doi: 10.1002/2013JC009312.

A. Chadwick, J. Morfett, and M. Borthwick. *Hydraulics in Civil and Environmental Engineering*, volume 126. 01 2013. doi: 10.1061/(ASCE)0733-9429(2000)126:9(724).

T. J. Chung. *Computational Fluid Dynamics*. Cambridge University Press, 2002.

J. M. Coleman. *Deltas – Processes of Deposition and Models for Exploration*. Burgess Publishing Company, 1981.

Collins Dictionaries. Definition of the word ‘delta’, 2024. [Online] Available at: https://www.collinsdictionary.com/dictionary/english/delta, [Accessed 22 July 2024].

C. Constanda. Taylor & Francis Group, 3rd edition, 2016. ISBN 9781498704953. doi: 10.1201/9781315381442.

R. Courant, K. Friedrichs, and H. Lewy. Über die partiellen differenzengleichungen der mathematischen physik. *Mathematische Annalen (in German)*, 100(1):32–74, 1928. doi: 10.1007/BF01448839.

Deltares. *Delft3D Hydro-Morphodynamics User Manual*. Deltares, 2021a.

Deltares. *Delft3D WAVE User Manual*. Deltares, 2021b.

J. Dominguez. The são francisco strandplain: A paradigm for wave-dominated deltas? *Geological Society, London, Special Publications*, 117:217–231, 10 1996. doi: 10.1144/GSL.SP.1996.117.01.13.

V. Duy Vinh, S. Ouillon, N. Thao, and N. Tien. Numerical simulations of suspended sediment dynamics due to seasonal forcing in the mekong coastal area. *Water*, 8:255, 06 2016. doi: 10.3390/w8060255.

D. Edmonds, A. J. Chadwick, M. P. Lamb, J. Lorenzo-Trueba, B. Murray, W. Nardin, G. Salter, and J. B. Shaw. Morphodynamic modeling of river-dominated deltas: A review and future perspectives. *Earth and Space Science Open Archive*, page 32, 2021. doi: 10.1002/essoar.10507512.1. URL `https://doi.org/10.1002/essoar.10507512.1`.

D. A. Edmonds and R. L. Slingerland. Mechanics of river mouth bar formation: Implications for the morphodynamics of delta distributary networks. *Journal of Geophysical Research: Earth Surface*, 112(F2), 2007. doi: https://doi.org/10.1029/2006JF000574. URL `https://agupubs.onlinelibrary.wiley.com/doi/abs/10.1029/2006JF000574`.

D. A. Edmonds and R. L. Slingerland. Significant effect of sediment cohesion on delta morphology. *Nature Geoscience*, pages 105–109, 2010.

D. A. Edmonds, D. C. Hoyal, B. A. Sheets, and R. L. Slingerland. Predicting delta avulsions: Implications for coastal wetland restoration. *Geology*, 37(8): 759–762, 08 2009. ISSN 0091-7613. doi: 10.1130/G25743A.1. URL https://doi.org/10.1130/G25743A.1.

D. A. Edmonds, R. Caldwell, E. Brondízio, and S. Siani. Coastal flooding will disproportionately impact people on river deltas. *Nature Communications*, 11: 1234567890, 09 2020. doi: 10.1038/s41467-020-18531-4.

F. M. Exner. *Über die Wechselwirkung zwischen Wasser und Geschiebe in Flüssen: Gedr. mit Unterstützg aus d. Jerome u. Margaret Stonborough-Fonds*. Hölder-Pichler-Tempsky, A.-G., 1925.

B. Fox-Kemper, H. Hewitt, C. Xiao, G. Adalgeirsdóttir, S. Drijfhout, T. Edwards, N. Golledge, M. Hemer, R. Kopp, G. Krinner, A. Mix, D. Notz, S. Nowicki, I. Nurhati, L. Ruiz, J.-B. Sallée, A. Slangen, and Y. Yu. *Ocean, Cryosphere and Sea Level Change*, page 1211–1362. Cambridge University Press, Cambridge, United Kingdom and New York, NY, USA, 2021. doi: 10.1017/9781009157896.011.

R. P. d. M. Frasson, T. M. Pavelsky, M. A. Fonstad, M. T. Durand, G. H. Allen, G. Schumann, C. Lion, R. E. Beighley, and X. Yang. Global relationships between river width, slope, catchment area, meander wavelength, sinuosity, and discharge. *Geophysical Research Letters*, 46(6):3252–3262, 2019. doi: https://doi.org/10.1029/2019GL082027. URL https://agupubs.

onlinelibrary.wiley.com/doi/abs/10.1029/2019GL082027.

W. E. Galloway. Process framework for describing the morphologic and stratigraphic evolution of deltaic depositional system. *Society of Economic Paleontologists and Mineralogist (SEPM), Special Publication No. 31*, pages 127–156, 1975.

W. Gao, D. Shao, Z. B. Wang, W. Nardin, W. Yang, T. Sun, and B. Cui. Combined effects of unsteady river discharges and wave conditions on river mouth bar morphodynamics. *Geophysical Research Letters*, 45, 11 2018. doi: 10.1029/2018GL080447.

W. Gao, D. Shao, Z. B. Wang, W. Nardin, P. Rajput, W. Yang, T. Sun, and B. Cui. Long-term cumulative effects of intra-annual variability of unsteady river discharge on the progradation of delta lobes: A modeling perspective. *Journal of Geophysical Research: Earth Surface*, 124(4):960–973, 2019. doi: https://doi.org/10.1029/2017JF004584. URL https://agupubs.onlinelibrary.wiley.com/doi/abs/10.1029/2017JF004584.

W. Gao, J. Nienhuis, W. Nardin, Z. B. Wang, D. Shao, T. Sun, and B. Cui. Wave controls on deltaic shoreline-channel morphodynamics: Insights from a coupled model. *Water Resources Research*, 56(9):e2020WR027298, 2020. doi: https://doi.org/10.1029/2020WR027298. URL https://agupubs.onlinelibrary.wiley.com/doi/abs/10.1029/2020WR027298. e2020WR027298 2020WR027298.

N. Geleynse, J. E. A. Storms, M. J. F. Stive, H. R. A. Jagers, and D. J. R. Walstra.

Modeling of a mixed-load fluvio-deltaic system. *Geophysical Research Letters*, 37(5), 2010. doi: https://doi.org/10.1029/2009GL042000. URL https://agupubs.onlinelibrary.wiley.com/doi/abs/10.1029/2009GL042000.

N. Geleynse, J. E. Storms, D.-J. R. Walstra, H. A. Jagers, Z. B. Wang, and M. J. Stive. Controls on river delta formation; insights from numerical modelling. *Earth and Planetary Science Letters*, 302(1):217–226, 2011. ISSN 0012-821X. doi: https://doi.org/10.1016/j.epsl.2010.12.013. URL https://www.sciencedirect.com/science/article/pii/S0012821X1000765X.

N. Geleynse, V. Voller, C. Paola, and V. Ganti. Characterization of river delta shorelines. *Geophysical Research Letters*, 39:17402–, 09 2012. doi: 10.1029/2012GL052845.

Google Earth 10.55.0.1. Danube – st. george distributary river mouth 44°53'50"n 29°34'55"e, 2019. [Online] Available at: https://earth.google.com/web/, [Accessed 07 August 2024].

Google Earth 10.55.0.1. Haliacmon river mouth 40°29'21"n 22°37'48"e, 2023a. [Online] Available at: https://earth.google.com/web/, [Accessed 24 May 2024].

Google Earth 10.55.0.1. Keum river mouth 36°00'12"n 126°38'22"e, 2023b. [Online] Available at: https://earth.google.com/web/, [Accessed 24 May 2024].

Google Earth 10.55.0.1. Manawatu river mouth 40°18'07"s 175°13'37"e, 2023c.

[Online] Available at: https://earth.google.com/web/, [Accessed 24 May 2024].

Google Earth 10.55.0.1. Porong river mouth 7°31'37"s 112°51'00"e, 2023d. [Online] Available at: https://earth.google.com/web/, [Accessed 24 May 2024].

Google Earth 10.55.0.1. Rhône river mouth 43°20'46"n 4°49'52"e, 2023e. [Online] Available at: https://earth.google.com/web/, [Accessed 24 May 2024].

C. Gualtieri, A. Angeloudis, F. Bombardelli, S. Jha, and T. Stoesser. On the values for the turbulent schmidt number in environmental flows. *Fluids*, 2(2), 2017. ISSN 2311-5521. doi: 10.3390/fluids2020017. URL https://www.mdpi.com/2311-5521/2/2/17.

L. Guo, M. Wegen, D. J. Roelvink, Z. B. Wang, and Q. He. Long-term, process-based morphodynamic modeling of a fluvio-deltaic system, part i: The role of river discharge. *Continental Shelf Research*, 109:95–111, 10 2015. doi: 10.1016/j.csr.2015.09.002.

M. Hillen. *Wave reworking of a delta: process-based modelling of sediment reworking under wave conditions in the deltaic environment*. PhD thesis, 03 2009.

A. J. F. Hoitink, Z. B. Wang, B. F. Vermeulen, Y. Huismans, and K. Kästner. Tidal controls on river delta morphology. *Nature Geoscience*, 10:637–645, 2017. URL https://api.semanticscholar.org/CorpusID:134946071.

J. R. Houston. Beach-fill volume required to produce specified dry beach width.

Coastal Engineering Technical Note 11-32, 1995. URL http://hdl.handle.net/11681/2135.

D. Hoyal and B. Sheets. Morphodynamic evolution of experimental cohesive deltas. *Journal of Geophysical Research*, 114, 04 2009. doi: 10.1029/2007JF000882.

S. Ikeda. Incipient motion of sand particles on side slopes. *Journal of Hydraulic Engineering*, 108:95–114, 1982.

A. Iwantoro, M. van der Vegt, and M. Kleinhans. Morphological evolution of bifurcations in tide-influenced deltas. *Earth Surface Dynamics*, 8:413–429, 06 2020. doi: 10.5194/esurf-8-413-2020.

D. J. Jerolmack and J. B. Swenson. Scaling relationships and evolution of distributary networks on wave-influenced deltas. *Geophysical Research Letters*, 34(23), 2007. doi: https://doi.org/10.1029/2007GL031823. URL https://agupubs.onlinelibrary.wiley.com/doi/abs/10.1029/2007GL031823.

A. Jiménez-Robles, M. Ortega-Sánchez, and M. Losada. Effects of basin bottom slope on jet hydrodynamics and river mouth bar formation. *Journal of Geophysical Research: Earth Surface*, 121, 06 2016. doi: 10.1002/2016JF003871.

J. W. Kamphuis. Alongshore sediment transport rate. *Journal of Waterway, Port, Coastal, and Ocean Engineering*, 117(6):624–640, 1991. doi: 10.1061/(ASCE)0733-950X(1991)117:6(624).

J. W. Kamphuis. *Introduction to Coastal Engineering and Management*. WORLD

SCIENTIFIC, 2nd edition, 2010. doi: 10.1142/7021. URL https://www.worldscientific.com/doi/abs/10.1142/7021.

H. Kernkamp and R. Uittenbogaard. *2D-LES of a free-surface mixing layer*, pages 409–418. Springer Netherlands, Dordrecht, 2001. ISBN 978-94-017-1263-7. doi: 10.1007/978-94-017-1263-7_49. URL https://doi.org/10.1007/978-94-017-1263-7_49.

T. Kim, B. Choi, and S. Lee. Hydrodynamics and sedimentation induced by large-scale coastal developments in the keum river estuary, korea. *Estuarine, Coastal and Shelf Science*, 68(3):515–528, 2006. ISSN 0272-7714. doi: https://doi.org/10.1016/j.ecss.2006.03.003. URL https://www.sciencedirect.com/science/article/pii/S027277140600093X. Ecological and Management Implications on Seagrass Landscapes.

A. N. Kolmogorov. The local structure of turbulence in incompressible viscous fluid for very large reynolds numbers. *Proceedings: Mathematical and Physical Sciences*, 434(1890):9–13, 1991. ISSN 09628444. URL http://www.jstor.org/stable/51980.

P. Komar. Computer models of delta growth due to sediment input from rivers and longshore transport. *Geological Society of America Bulletin*, 84:2217–, 07 1973. doi: 10.1130/0016-7606(1973)84⟨2217:CMODGD⟩2.0.CO;2.

W. Lageweg and A. Slangen. Predicting dynamic coastal delta change in response to sea-level rise. *Journal of Marine Science and Engineering*, 5:24, 06 2017. doi: 10.3390/jmse5020024.

N. Leonardi, A. Canestrelli, T. Sun, and S. Fagherazzi. Effect of tides on mouth bar morphology and hydrodynamics. *Journal of Geophysical Research: Oceans*, 118, 09 2013. doi: 10.1002/jgrc.20302.

S. Lera, W. Nardin, L. Sanford, C. Palinkas, and R. Guercio. The impact of submersed aquatic vegetation on the development of river mouth bars. *Earth Surface Processes and Landforms*, 44, 01 2019. doi: 10.1002/esp.4585.

G. Lesser. *An approach to medium-term coastal morphological modelling*. PhD thesis, TU Delft, 2009.

M. Liang, C. Van Dyk, and P. Passalacqua. Quantifying the patterns and dynamics of river deltas under conditions of steady forcing and relative sea level rise. *Journal of Geophysical Research: Earth Surface*, 121(2):465–496, 2016. doi: https://doi.org/10.1002/2015JF003653. URL `https://agupubs.onlinelibrary.wiley.com/doi/abs/10.1002/2015JF003653`.

P. Liu, Q. Li, Z. Li, T. Hoey, Y. Liu, and C. Wang. Land subsidence over oilfields in the yellow river delta. *Remote Sensing*, 7:1540–1564, 02 2015. doi: 10.3390/rs70201540.

Y. Liu, H. Chen, J. Wang, S. Yang, and A. Chen. Numerical simulation for the effects of waves and grain size on deltaic processes and morphologies. *Open Geosciences*, 12(1):1286–1301, 2020. doi: doi:10.1515/geo-2020-0196. URL `https://doi.org/10.1515/geo-2020-0196`.

K. Mangor, N. K. Drønen, K. H. Kærgaard, and S. E. Kristensen. *Shoreline Management Guidelines*. DHI, 2017.

G. Mariotti, F. Falcini, N. Geleynse, M. Guala, T. Sun, and S. Fagherazzi. Sediment eddy diffusivity in meandering turbulent jets: Implications for levee formation at river mouths. *Journal of Geophysical Research: Earth Surface*, 118:1908–1920, 09 2013. doi: 10.1002/jgrf.20134.

J. D. Milliman and K. L. Farnsworth. *River Discharge to the Coastal Ocean: A Global Synthesis*. Cambridge University Press, 2011.

W. Nardin and D. Edmonds. Optimum vegetation height and density for inorganic sedimentation in deltaic marshes. *Nature Geoscience*, 7, 08 2014. doi: 10.1038/ngeo2233.

W. Nardin and S. Fagherazzi. The effect of wind waves on the development of river mouth bars. *Geophysical Research Letters*, 39(12), 2012. doi: https://doi.org/10.1029/2012GL051788. URL https://agupubs.onlinelibrary.wiley.com/doi/abs/10.1029/2012GL051788.

W. Nardin, G. Mariotti, D. Edmonds, R. Guercio, and S. Fagherazzi. Growth of river mouth bars in sheltered bays in the presence of frontal waves. *Journal of Geophysical Research: Earth Surface*, 118(2):872–886, 2013.

W. Nardin, D. Edmonds, and S. Fagherazzi. Influence of vegetation on spatial patterns of sediment deposition in deltaic islands during flood. *Advances in Water Resources*, 93, 01 2016. doi: 10.1016/j.advwatres.2016.01.001.

NASA Earth Observatory. Caravelas strandplain, bahia province, brazil, 2006. URL https://eoimages.gsfc.nasa.gov/images/imagerecords/7000/7505/ISS014-E-10499_lrg.jpg. [Online; accessed August 7, 2024].

J. H. Nienhuis, A. D. Ashton, P. C. Roos, S. J. M. H. Hulscher, and L. Giosan. Wave reworking of abandoned deltas. *Geophysical Research Letters*, 40(22): 5899–5903, 2013. doi: https://doi.org/10.1002/2013GL058231. URL https://agupubs.onlinelibrary.wiley.com/doi/abs/10.1002/2013GL058231.

J. H. Nienhuis, A. D. Ashton, and L. Giosan. What makes a delta wave-dominated? *Geology*, 43(6):511–514, 06 2015. ISSN 0091-7613. doi: 10.1130/G36518.1. URL https://doi.org/10.1130/G36518.1.

J. H. Nienhuis, A. J. F. T. Hoitink, and T. E. Törnqvist. Future change to tide-influenced deltas. *Geophysical Research Letters*, 45(8):3499–3507, 2018. doi: https://doi.org/10.1029/2018GL077638. URL https://agupubs.onlinelibrary.wiley.com/doi/abs/10.1029/2018GL077638.

J. H. Nienhuis, A. D. Ashton, D. A. Edmonds, A. Hoitink, A. J. Kettner, J. C. Rowland, and T. E. Törnqvist. Global-scale human impact on delta morphology has led to net land area gain. *Nature*, 577(7791):514–518, 2020.

G. J. Orton and H. G. Reading. Variability of deltaic processes in terms of sediment supply, with particular emphasis on grain size. *Sedimentology*, 1993.

I. Overeem, J. Syvitski, and E. Hutton. *Three-Dimensional Numerical Modeling of Deltas*, volume 83, pages 13–30. 01 2005. ISBN 1-56576-113-8. doi: 10.2110/pec.05.83.0011.

E. Park, H. Loc, J. Lim, and D. Chiwatkulsiri. Source-to-sink sediment fluxes and budget in the chao phraya river, thailand: A multi-scale analysis based on the national dataset. *Journal of Hydrology*, 01 2021. doi: 10.1016/j.jhydrol.2020.125643.

N. Phien-wej, P. Giao, and P. Nutalaya. Land subsidence in bangkok, thailand. *Engineering Geology*, 82:187–201, 02 2006. doi: 10.1016/j.enggeo.2005.10.004.

S. B. Pope. *Turbulent Flows*. Cambridge University Press, 2000.

R. Ranasinghe, C. Swinkels, A. Luijendijk, D. Roelvink, J. Bosboom, M. Stive, and D. Walstra. Morphodynamic upscaling with the morfac approach: Dependencies and sensitivities. *Coastal Engineering*, 58(8):806–811, 2011. ISSN 0378-3839. doi: https://doi.org/10.1016/j.coastaleng.2011.03.010. URL https://www.sciencedirect.com/science/article/pii/S0378383911000457.

K. M. Ratliff, E. H. W. Hutton, and A. B. Murray. Exploring wave and sea-level rise effects on delta morphodynamics with a coupled river-ocean model. *Journal of Geophysical Research: Earth Surface*, 123(11):2887–2900, 2018. doi: https://doi.org/10.1029/2018JF004757. URL https://agupubs.onlinelibrary.wiley.com/doi/abs/10.1029/2018JF004757.

D. Reeve, Y. Chen, S. Pan, V. Magar, D. Simmonds, and A. Zacharioudaki. An investigation of the impacts of climate change on wave energy generation: The wave hub, cornwall, uk. *Renewable Energy*, 36(9):2404–2413, 2011. ISSN 0960-1481. doi: https://doi.org/10.1016/j.renene.2011.02.020. URL https://www.sciencedirect.com/science/article/pii/S096014811100111X.

L. F. Richardson. *Weather Prediction by Numerical Process*. Cambridge Mathematical Library. Cambridge University Press, 2 edition, 2007.

Rik. Triangleplot, 2024. Available online at https://www.mathworks.com/matlabcentral/fileexchange/64996-triangleplot [Retrieved May 1, 2024].

H. H. Roberts. Dynamic changes of the holocene mississippi river delta plain: The delta cycle. *Journal of Coastal Research*, 13(3):605–627, 1997. ISSN 07490208, 15515036. URL http://www.jstor.org/stable/4298659.

D. Roelvink and A. Reniers. *A Guide to Modeling Coastal Morphology*. WORLD SCIENTIFIC, 2011. doi: 10.1142/7712. URL https://www.worldscientific.com/doi/abs/10.1142/7712.

V. Rossi, W. Kim, J. Leva Lopez, D. Edmonds, N. Geleynse, C. Olariu, R. Steel, M. Hiatt, and P. Passalacqua. Impact of tidal currents on delta-channel deepening, stratigraphic architecture and sediment bypass beyond the shoreline. *Geology*, 44, 08 2016. doi: 10.1130/G38334.1.

Y. Saito, N. Chaimanee, J. Thanawat, and J. Syvitski. Shrinking megadeltas in asia: Sea-level rise and sediment reduction impacts from case study of the chao phraya delta. *LOICZ Inprint*, 2007:3–9, 06 2007.

S. Seneviratne, X. Zhang, M. Adnan, W. Badi, C. Dereczynski, A. Di Luca, S. Ghosh, I. Iskandar, J. Kossin, S. Lewis, F. Otto, I. Pinto, M. Satoh, S. Vicente-Serrano, M. Wehner, and B. Zhou. *Weather and Climate Extreme Events in a Changing Climate*, page 1513–1766. Cambridge University Press, Cambridge, United Kingdom and New York, NY, USA, 2021. doi: 10.1017/9781009157896.013.

J. B. Shaw, M. A. Wolinsky, C. Paola, and V. R. Voller. An image-based method for shoreline mapping on complex coasts. *Geophysical Research Letters*, 35(12), 2008. doi: https://doi.org/10.1029/2008GL033963. URL https://agupubs.onlinelibrary.wiley.com/doi/abs/10.1029/2008GL033963.

E. Sloan. manybears/delta-development-thresholds: Effects of tidal range and significant wave height on delta development - matlab files v1.0.0, 2024.

E. Sloan, N. Dodd, and R. Briganti. Idealised outputs on effects of tides and waves on delta development using the model delft3d on a 36 and 72 year scale, 2024.

R. Soulsby. *Dynamics of marine sands*. T. Telford London, 1997.

J. Syvitski and Y. Saito. Morphodynamics of deltas under the influence of humans. *Global and Planetary Change*, 57(3):261–282, 2007. ISSN 0921-8181. doi: https://doi.org/10.1016/j.gloplacha.2006.12.001. URL https://www.sciencedirect.com/science/article/pii/S0921818106003146.

J. Syvitski, C. J. Vörösmarty, A. J. Kettner, and P. Green. Impact of humans on the flux of terrestrial sediment to the global coastal ocean. *Science (New York, N.Y.)*, 308(5720):376—380, April 2005. ISSN 0036-8075. doi: 10.1126/science.1109454. URL https://doi.org/10.1126/science.1109454.

J. Syvitski, E. Anthony, Y. Saito, F. Zăinescu, J. Day, J. P. Bhattacharya, and L. Giosan. Large deltas, small deltas: Toward a more rigorous understanding of coastal marine deltas. *Global and Planetary Change*, 218:103958, 2022a. ISSN 0921-8181. doi: https://doi.org/10.1016/j.gloplacha.2022.

103958. URL https://www.sciencedirect.com/science/article/pii/S0921818122002259.

J. Syvitski, J. Restrepo-Angel, Y. Saito, I. Overeem, C. Vörösmarty, H. Wang, and D. Olago. Earth's sediment cycle during the anthropocene. *Nature Reviews Earth & Environment*, 3:1–18, 02 2022b. doi: 10.1038/s43017-021-00253-w.

T. K. O. Ta, V. L. Nguyen, M. Tateishi, I. Kobayashi, S. Tanabe, and Y. Saito. Holocene delta evolution and sediment discharge of the mekong river, southern vietnam. *Quaternary Science Reviews*, 21(16):1807–1819, 2002. ISSN 0277-3791. doi: https://doi.org/10.1016/S0277-3791(02)00007-0. URL https://www.sciencedirect.com/science/article/pii/S0277379102000070.

S. Tanabe, Y. Saito, Y. Sato, Y. Suzuki, S. Sinsakul, S. Tiyapairach, and N. Chaimanee. Stratigraphy and holocene evolution of the mud-dominated chao phraya delta, thailand. *Quaternary Science Reviews*, 22:789–807, 04 2003. doi: 10.1016/S0277-3791(02)00242-1.

A. Tejedor, A. Longjas, R. Caldwell, D. A. Edmonds, I. Zaliapin, and E. Foufoula-Georgiou. Quantifying the signature of sediment composition on the topologic and dynamic complexity of river delta channel networks and inferences toward delta classification. *Geophysical Research Letters*, 43(7):3280–3287, 2016. doi: https://doi.org/10.1002/2016GL068210. URL https://agupubs.onlinelibrary.wiley.com/doi/abs/10.1002/2016GL068210.

H. Tennekes and J. Lumley. *A First Course in Turbulence*. MIT Press, 1972.

V. Q. Thanh, J. Reyns, C. Wackerman, E. F. Eidam, and D. Roelvink. Modelling suspended sediment dynamics on the subaqueous delta of the mekong river. *Continental Shelf Research*, 147:213–230, 2017. ISSN 0278-4343. doi: https://doi.org/10.1016/j.csr.2017.07.013. URL https://www.sciencedirect.com/science/article/pii/S0278434316306586. Sediment- and hydro-dynamics of the Mekong Delta: from tidal river to continental shelf.

K. Uehara, P. Sojisuporn, Y. Saito, and T. Jarupongsakul. Erosion and accretion processes in a muddy dissipative coast, the chao phraya river delta, thailand. *Earth Surface Processes and Landforms*, 35(14):1701–1711, 2010. doi: https://doi.org/10.1002/esp.2012. URL https://onlinelibrary.wiley.com/doi/abs/10.1002/esp.2012.

R. Uittenbogaard and B. Vossen. *Subgrid-scale model for quasi-2D turbulence in shallow water*, pages 575–582. 09 2004. ISBN 978-90-5809-700-2. doi: 10.1201/9780203027325.ch72.

H. van der Vegt, J. Storms, D.-J. Walstra, and N. Howes. Can bed load transport drive varying depositional behaviour in river delta environments? *Sedimentary Geology*, 345:19–23, 11 2016. doi: 10.1016/j.sedgeo.2016.08.009.

L. C. van Rijn. *Principles of sediment transport in rivers, estuaries and coastal seas*. 1993.

A. Vespremeanu-Stroe, F. Zăinescu, L. Preoteasa, F. Tătui, S. Rotaru, C. Morhange, M. Stoica, J. Hanganu, A. Timar-Gabor, I. Cârdan, and N. Piotrowska. Holocene evolution of the danube delta: An integral reconstruction and a revised chronology. *Marine Geology*, 388:38–61, 2017. ISSN

0025-3227. doi: https://doi.org/10.1016/j.margeo.2017.04.002. URL https://www.sciencedirect.com/science/article/pii/S0025322717301445.

R. J. Vlijm. Process-based modelling of morphological response to submerged breakwaters. Master's thesis, TU Delft, 2011.

M. Wolinsky, D. Edmonds, J. Martin, and C. Paola. Delta allometry: Growth laws for river deltas. *Geophysical Research Letters - GEOPHYS RES LETT*, 37, 11 2010. doi: 10.1029/2010GL044592.

L. D. Wright. *River Deltas*, pages 1–76. Springer New York, New York, NY, 1985. ISBN 978-1-4612-5078-4. doi: 10.1007/978-1-4612-5078-4_1. URL https://doi.org/10.1007/978-1-4612-5078-4_1.

Z.-H. Xu, S.-H. Wu, M.-C. Liu, J.-S. Zhao, Z.-H. Chen, K. Zhang, J.-J. Zhang, and Z. Liu. Effects of water discharge on river-dominated delta growth. *Petroleum Science*, 18(6):1630–1649, 2021. ISSN 1995-8226. doi: https://doi.org/10.1016/j.petsci.2021.09.027. URL https://www.sciencedirect.com/science/article/pii/S1995822621000753.

Z. Zhou, L. Chen, J. Tao, Z. Gong, L. Guo, M. Wegen, I. Townend, and C. Zhang. The role of salinity in fluvio-deltaic morphodynamics: A long-term modelling study. *Earth Surface Processes and Landforms*, 01 2020. doi: 10.1002/esp.4757.

F. Zăinescu, E. Anthony, A. Vespremeanu-Stroe, M. Besset, and F. Tatui. Concerns about data linking delta land gain to human action. *Nature*, 614:E20–E25, 02 2023. doi: 10.1038/s41586-022-05624-x.

Appendix A

Simple verification tests

A.1 FLOW – reproducing selected simulations of Edmonds and Slingerland (2010)

Here we present the results of early verification tests in which the aim was to reproduce the results of Edmonds and Slingerland (2010). This involved rerunning two of their simulations using the original setup files (RunIDs N and W – see Edmonds and Slingerland, 2010). As such, the model setup here is precisely as described in Edmonds and Slingerland (2010). Comparison of the original and repeated simulations are shown in Figures A.1a to d.

While the original simulations and reruns do produce different bathymetries at the time shown, both pairs of original simulations vs. reruns do exhibit qualitatively similar morphologies in terms of channel configuration and overall distribution of

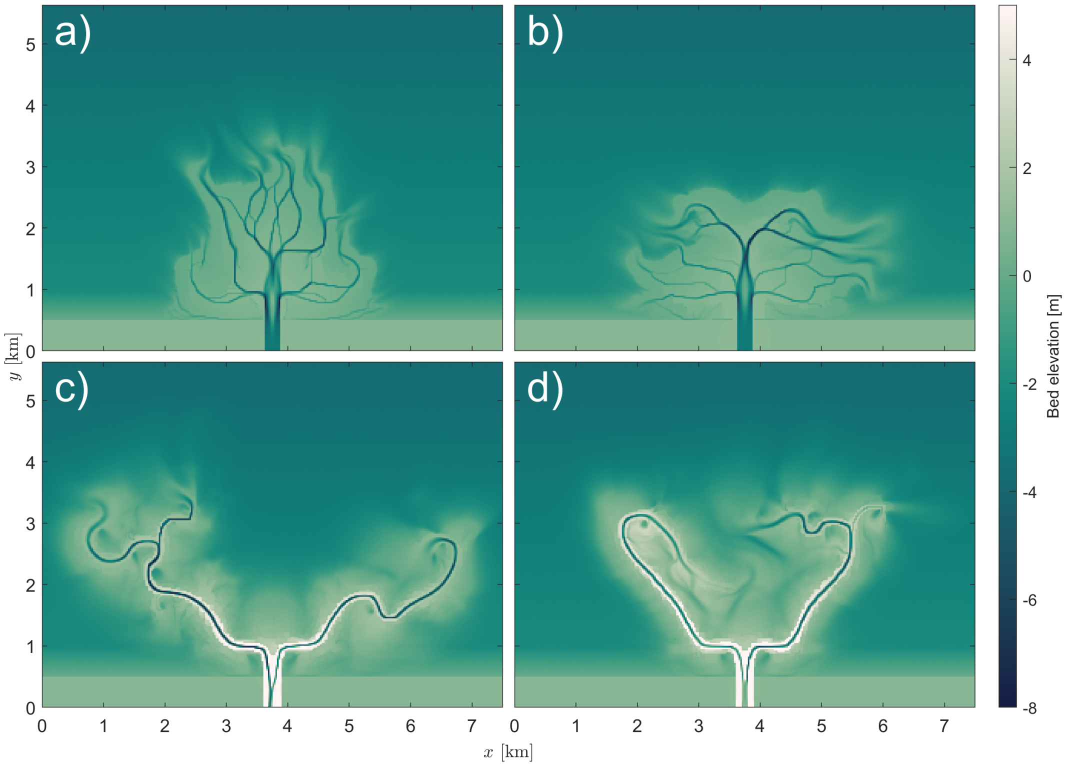

Figure A.1: Bathymetries at $t \approx 2.7$ yr for simulations: a) N, original; b) N, repeat; c) W, original; and d) W, repeat.

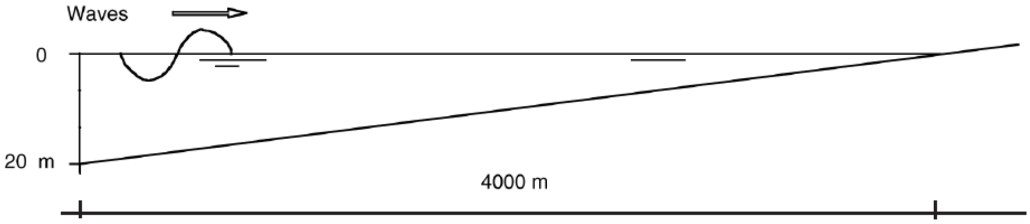

Figure A.2: Profile of sloping beach used in refraction test. Incident wave are oriented with direction 30° to shore-normal at the offshore boundary. (Figure adapted from Allard et al., 2004).

sediment. Notably, the originals and reruns produce almost identical morphologies close to the initial river mouth, but diverge as channels grow in differing directions as they develop; this well illustrates the observation that small upstream differences may lead to greatly differing morphologies in delta models (see §4.2.3). Given that the exact same setup files were used to produce the originals and reruns, the variability in outcomes almost certainly a result of differences between versions of the software used. Despite these observations, the results of this test suggest that the FLOW module is operating correctly.

A.2 WAVE – wave refraction over a sloped beach

Verification testing of WAVE was conducted by reproducing a simple wave refraction test case on a linearly sloping beach (Test 8 in Allard et al., 2004). The model setup is as defined in Allard et al. (2004), with domain and bathymetry as illustrated in Figure A.2. Note that while Allard et al. (2004) describe a beach of infinite alongshore dimension, our own model employs a domain with alongshore dimension $L_y = 10$ km, with measurements of H_s and wave angle recorded at $y = 4.875$ km.

In addition to comparison between our own numerical results and those of Allard et al. (2004), analytical predictions are made of H_s and mean wave approach angle θ. Mean wave directions $\theta(x)$ are determined analytically using Snell's Law:

$$\frac{\sin(\theta(0))}{c(0)} = \frac{\sin(\theta(x))}{c(x)} \tag{A.1}$$

where

$$c(x) = \frac{\omega}{k} \tag{A.2}$$

is wave celerity [m s^{-1}], with $\omega = 2\pi/T$ the wave radial frequency [rad s^{-1}], assuming $T = T_p = 10$ s; and $k = k(x)$ the wave number [m^{-1}]. Wave number k is calculated iteratively using the dispersion relation:

$$\omega^2 = gk\tanh(kh). \tag{A.3}$$

Significant wave heights $H_s(x)$ are determined analytically using the relationship (see e.g. Chadwick et al., 2013):

$$H_s(x) = H_s(0)\sqrt{\frac{c_g(0)}{c_g(x)}\frac{\cos(\theta(0))}{\cos(\theta(x))}} \tag{A.4}$$

where $c_g(x)$ is wave group celerity [m s^{-1}], given by:

$$\frac{c}{2}\left(1 + \frac{2kh}{\sinh(2kh)}\right). \tag{A.5}$$

Wave angles and significant wave heights throughout the cross-shore direction are shown in Figure A.3. Shown are numerical results of our own tests and those of

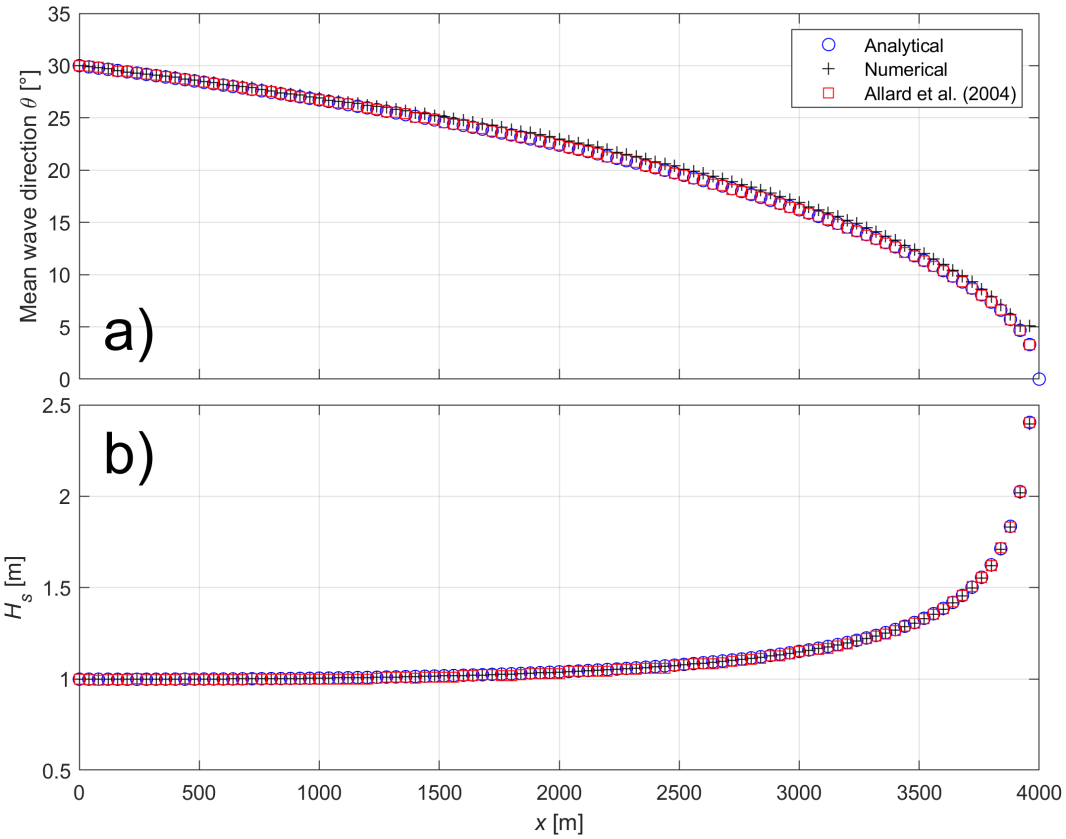

Figure A.3: Results of WAVE verification testing, alongside values determined by Allard et al. (2004). Sub-figures show: a) wave approach angle θ (0 indicates shore-normal); and b) H_s. Note that wave energy dissipation due to bed friction is disabled in these simulations, hence the monotonically increasing wave heights under reducing depth.

Allard et al. (2004), alongside the analytical solutions. Analytical and numerical results for H_s (Figure A.3b) are almost identical. Small differences between the present numerical results and those of Allard et al. (2004) are evident in Figure A.3b, up to around $\Delta\theta \approx 0.6°$. The reasons for this discrepancy aren't clear, but are likely a result of either slight differences in our and their model setups, or differences in the software versions used. Overall, the results presented here suggest that the WAVE module is operating correctly.

A.3 Coupled WAVE and FLOW - submerged breakwater

While the previous sections of this appendix demonstrated that the installed versions of both FLOW and WAVE function correctly when run independently, presented here are the results of testing intended to verify that the modules also work when run in a coupled setup. To this end, the objective is to reproduce a submerged breakwater simulation as presented by Vlijm (2011). These simulations were designed to match the model setup as described by Vlijm (2011). However, it should be noted that the implementation of their setup as presented here produced a slightly different morphology than that seen in the original paper; specifically the cross-shore beach profile (and hence also cross-shore position of the shoreline) are somewhat different. Note that the breaker is therefore at a slightly different cross-shore position in the reproduced simulations in comparison to Vlijm (2011), as the position is set relative to the shoreline, which itself differs between the original and reproduced simulations. However, as the objective is only to determine that coupled FLOW and WAVE are producing qualitatively similar results to those of Vlijm (2011), these differences are not considered significant.

Significant wave heights, free surface elevations, fluid velocities, and final bed elevations for the chosen test simulation are shown in Figures A.4 (for Vlijm, 2011) and A.5 (for the present, reproduced simulations).

Overall, the reproduced simulations give very similar results to the original simulations. The greatest differences can be seen close to the ends of the submerged breakers, where the velocity field produces slightly different patterns of scour and deposition, leading to some variation in final bathymetry. These differences are

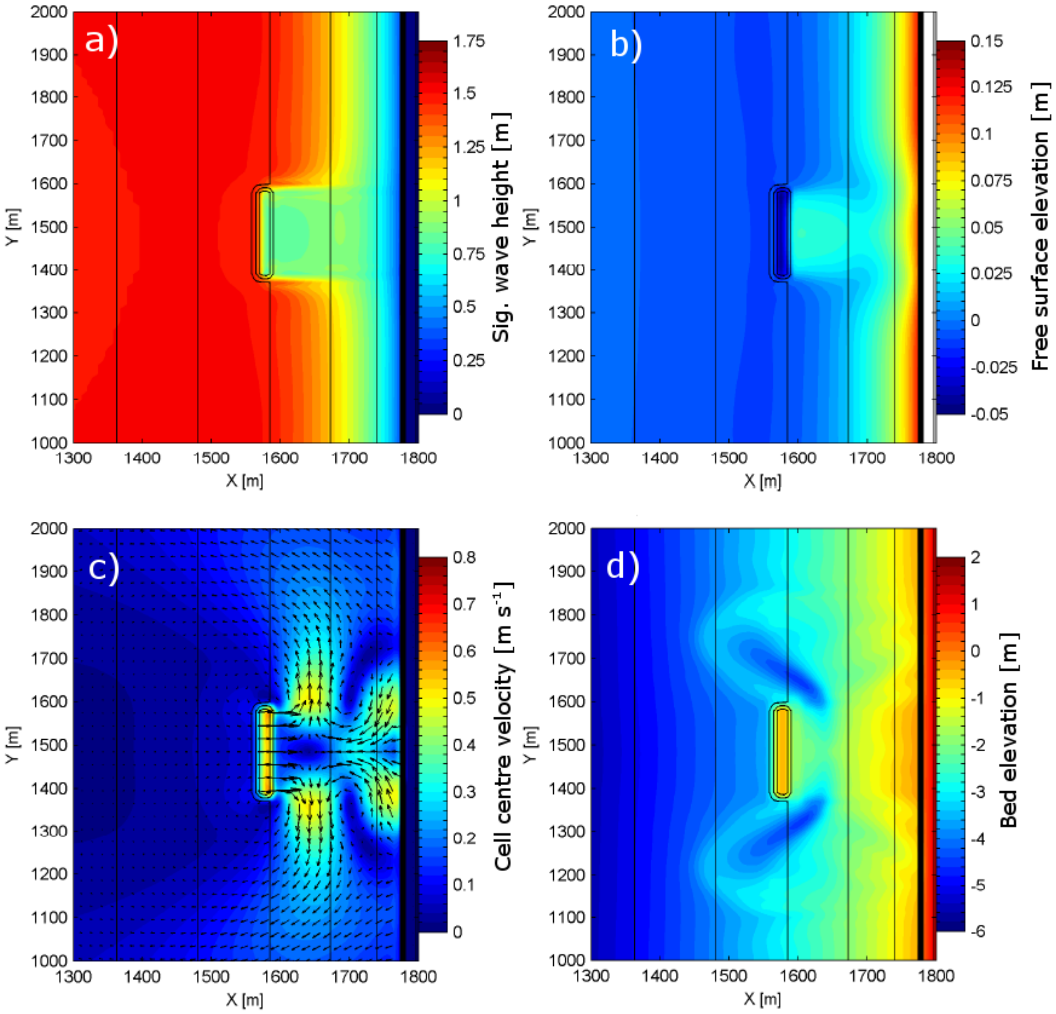

Figure A.4: Results of simulation of Vlijm (2011) with breaker width $x_b = 200$ m and breaker distance from shoreline $L_b = 200$ m. Subfigures show: a) Significant wave height at simulation start; b) free surface elevation at simulation start; c) cell-centre fluid velocity magnitudes and vectors (vector lengths proportional to magnitudes) at simulation start; and d) bathymetry at $t = 90$ day. Black contour lines (at 1 m intervals) indicate initial bathymetry in all subfigures. (Figure adapted from Vlijm, 2011).

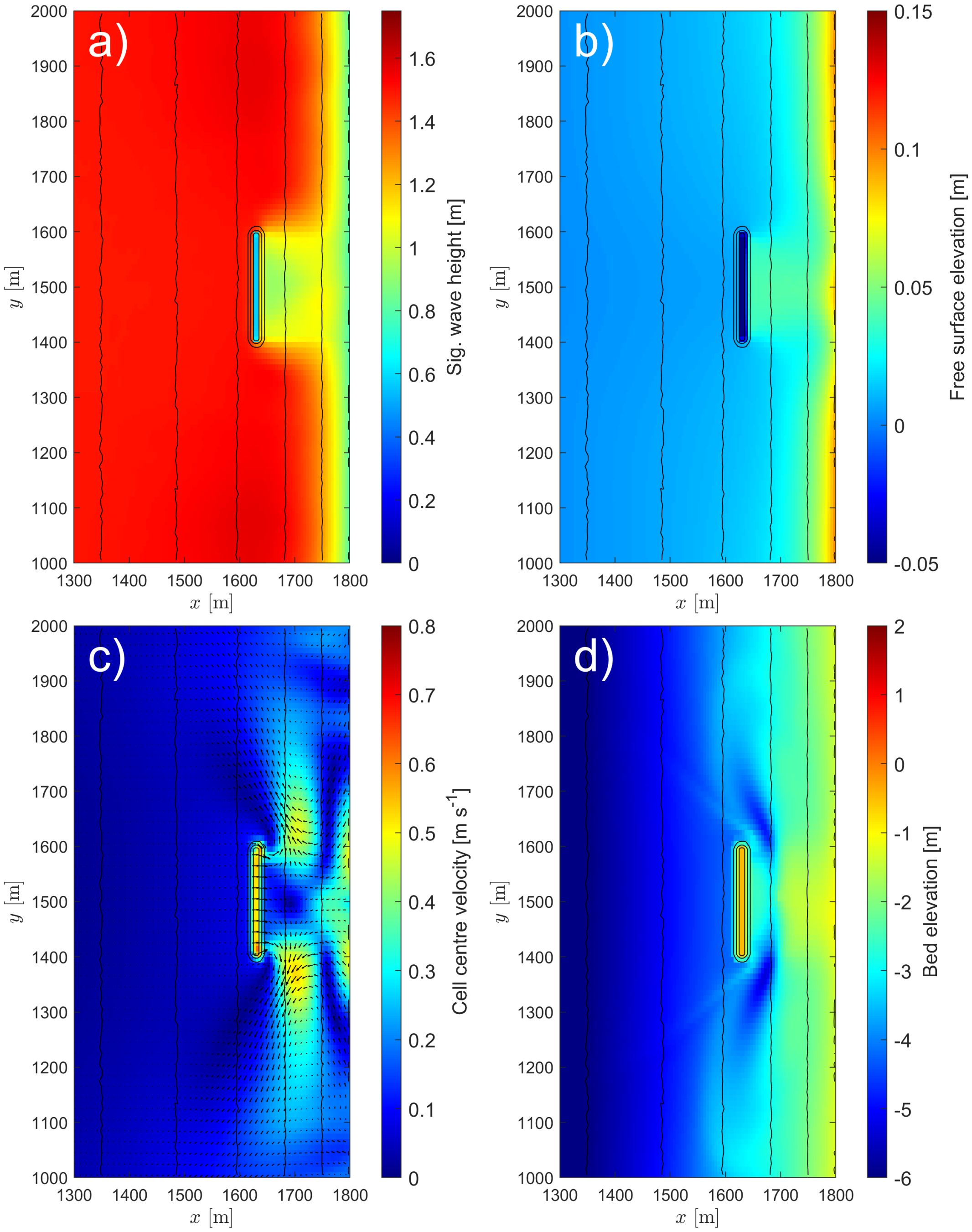

Figure A.5: Results of coupled FLOW-WAVE verification tests. Subfigures show: a) Significant wave height at simulation start; b) free surface elevation at simulation start; c) cell-centre fluid velocity magnitudes and vectors (vector lengths proportional to magnitudes) at simulation start; and d) bathymetry at $t = 90$ day. Black contour lines (at 1 m intervals) indicate initial bathymetry in all subfigures.

likely attributable to minor differences in model setups. Overall, these tests suggest that coupled WAVE-FLOW simulations are operating correctly.

Appendix B

Estimation of largest eddy timescale τ_e by consideration of initial river jet stability

Stability of the river jet is analysed following the methodology of Canestrelli et al. (2014), wherein a stability number, S_0 [-], is defined in relation to two critical stability numbers, $S_{c,l}$ [-] and $S_{c,u}$ [-]. The critical stability numbers denote the thresholds between stable (i.e. non-vortex-shedding), transitional (wherein jets may be either stable or unstable), and unstable (i.e. vortex-shedding) jets. The stability number S_0 is defined as:

$$S_0 = \frac{gB}{C^2 h} \tag{B.1}$$

where B is river width [m]. The critical stability numbers $S_{c,l}$ (lower) and $S_{c,u}$ (upper) are defined as:

$$S_{c,l} = \left(0.9 \cdot 10^{-3}\right) Re_B^{0.235} \tag{B.2}$$

$$S_{c,u} = \left(1.9 \cdot 10^{-3}\right) Re_B^{0.235} \tag{B.3}$$

where $Re_B = u_0 B/\nu$ is the "river mouth" Reynolds number [-]; u_0 is the cross-section-averaged velocity at the river mouth [$\mathrm{m\,s^{-1}}$]; and ν is the kinematic viscosity of water [$\mathrm{m^2\,s^{-1}}$].

To determine whether the river jet falls into the stable, unstable or transitional regimes, a single tide with range $H_t = 6$ m and period $T_t = 12.5$ hr (approximately semi-diurnal) tide is simulated. This simulation is identical to simulation W0T6, but has all sediment transport disabled. Eqs. (B.1) to (B.2) are solved over the duration of the simulated tide, with: $C = 45$ $\mathrm{m^{1/2}\,s^{-1}}$; $\nu = 1.0 \times 10^{-6}$ $\mathrm{m^2\,s^{-1}}$ (freshwater at $20°$C); h taken as the instantaneous mid channel-mouth depth; and u_0 taken as equal to the instantaneous channel-centre velocity. Calculated values of S_0, $S_{c,l}$, and $S_{c,u}$ over time are as shown in Figure B.1. Generally, the discharging river mouth jet remains in the stable regime over a full tide, but briefly enters the transitional regime between approximately $10 < t < 12$ hr. As our objective is to identify the greatest potential eddy timescale that might occur in our simulations, we assume unstable vortex shedding will occur when jet flow lies in the transitional regime.

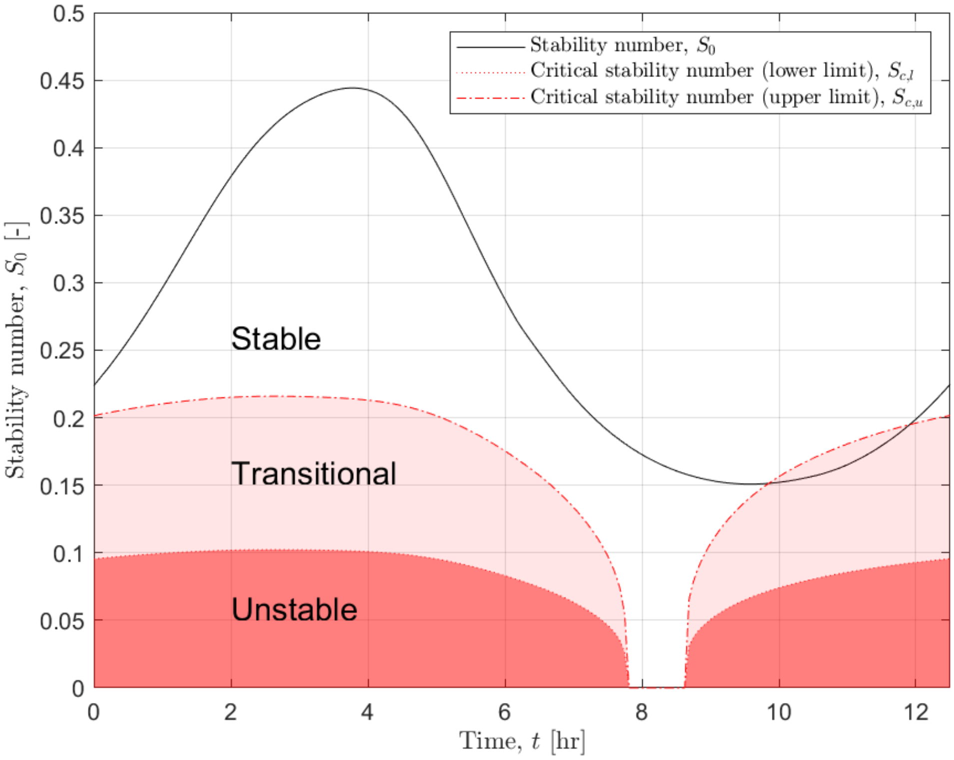

Figure B.1: Values of S_0, $S_{c,l}$, and $S_{c,u}$ over a single tide with period 12.5 hr and range 6 m. Red area denotes unstable regions, light pink area denotes transitional regions, and blank area denotes stable regions. The brief period where $S_{c,l} = S_{c,u} = 0$ occurring at approximately $7.75 < t < 8.75$ hr represents a brief period of flow reversal at the river mouth. (Note that Eqs. (B.2) and (B.3) actually give complex results in this period, but only the real parts are plotted.)

B.1 Estimation of eddy timescale

Determination of τ_e follows the stated assumption that unstable vortex shedding will potentially occur in our simulations. Mariotti et al. (2013) offer a method of estimating the time taken for one half revolution of an eddy, T_E [s] under vortex shedding conditions:

$$T_E = \frac{1}{S_{t,0}}\frac{B}{u_o} \tag{B.4}$$

where $S_{t,0}$ is the Strouhal number of the vortex-shedding jet [-], here set to a value of 0.07 associated with plane turbulent jets (Mariotti et al., 2013). (Note that while our simulations investigate river discharge into basins with (initial) slopes of 1 in 1000 rather than flat basins, jet stability does not significantly differ at this slope (Jiménez-Robles et al., 2016), hence we assume this value of the Strouhal number to also be appropriate here.) As T_E represents the notional time it takes for the largest eddies to perform one half rotation, it follows that:

$$T_E = \frac{(\pi/2)\,\ell_e}{u_e} = \frac{\pi}{2}\tau_e,$$

and hence:

$$\tau_e = \frac{2}{\pi}T_E = \frac{2}{0.07\pi}\frac{B}{u_0}. \tag{B.5}$$

During the period in which the river mouth is in the transitional regime, the mean river mouth velocity $u_0 = 0.98$ m s^{-1}. Thus, for $B = 250$ m and $u_0 = 0.98$ m s^{-1}, Eq. (B.5) gives: $\tau_e = 2320$ s (38 min 40 s).

Appendix C

Establishment of delta quasi-equilibrium

Delta quasi-equilibrium is analysed with respect to the wet-area growth law outlined by Wolinsky et al. (2010). Figure C.1 shows the time-evolution of A_{wet}/A (ratio of wet area, A_{wet}, to total area, A, within region enclosed by low tide line and initial coastline) for all simulations in which deltas form. In general, simulations tend towards quasi-equilibrium values of $0.2 \leq (A_{wet}/A) \leq 0.4$ at $t = 36$ yr, particularly for $H_s \leq 0.8$ m (Figures C.1a to c). All non-tidal simulations (blue triangles in Figure C.1) show occasional spikes in A_{wet}/A, which is related to the flatter delta plain and related avulsion mechanics occurring in these cases (Wolinsky et al., 2010, – see §7.1). Simulations with $H_s = 1.2$ m (Figure C.1d) show the greatest variability in A_{wet}/A over time, which we attribute to both large $\langle \chi \rangle$ values and a (related) highly changeable low tide shoreline position in these cases.

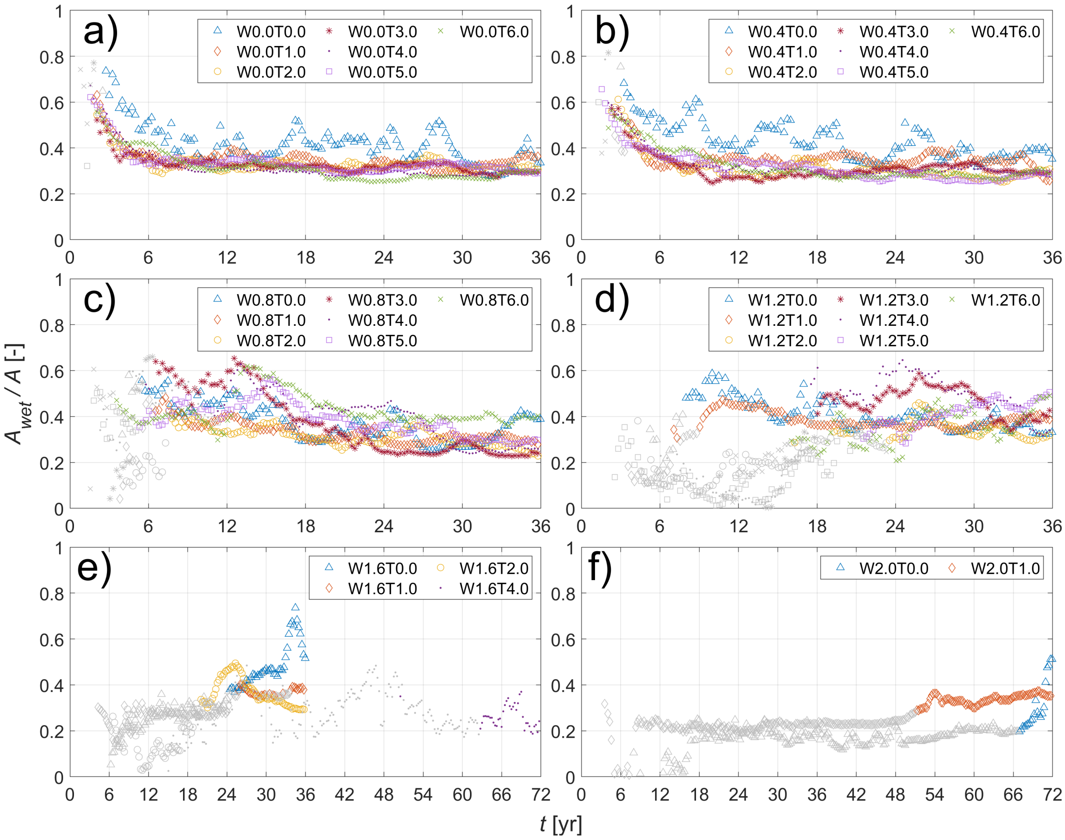

Figure C.1: Development of A_{wet}/A over time for all simulations that produced deltas. Instances in which a given morphology is not (yet) considered to be a delta are shown in grey.

Simulations W1.6T1.0 and W2.0T1.0 (Figures C.1e and f) both exhibit a stable quasi-equilibrium in wet fraction prior to delta formation. Following delta formation in both cases, A_{wet}/A increases slightly, but quasi-equilibrium is maintained. Simulations W1.6T0.0, W1.6T2.0, and W2.0T0.0 (Figures C.1e and f) form deltas only towards the end of their simulated durations, such that there is a lack of data with which to make definitive statements on their quasi-equilibrium state. We do note however, that both W1.6T0.0 and W2.0T0.0 show large increases in A_{wet}/A close to the end of their respective simulated durations. This is a result of growth of A to encompass predominantly wet regions during the estuarine infilling process.

In summary, the stability of A_{wet}/A is more clearly observed at lower wave heights. When tidal variation of water level is absent, spikes in A_{wet}/A occur as a result of frequent avulsions and overland flow. The ratio A_{wet}/A is evidently a better predictor of projected delta growth at relatively low values of $\langle H_s \rangle$. Overall, the wet fraction quasi-equilibrium criterion of Wolinsky et al. (2010) becomes less valid as marine energy increases; as such, quasi-equilibrium states cannot easily be inferred in such cases.

Appendix D

Calculation of diffusion coefficients for the shoreline diffusion equation

The shoreline diffusion equation, without sediment source term, is:

$$\frac{\partial y}{\partial t} - \kappa_{sde} \frac{\partial^2 y}{\partial x^2} = 0 \tag{D.1}$$

where x is alongshore coordinate [m]; y is shoreline displacement [m]; t is time [s]; and κ_{sde} is a diffusion coefficient [m^2 s^{-1}] (Kamphuis, 2010). Here, κ_{sde} is interpreted to be equivalent to κ_d in Eq. (8.3).

κ_{sde} may be calculated as:

$$\kappa_{sde} = \frac{Q_k}{\alpha_b d_p} \tag{D.2}$$

where Q_k is alongshore sediment flux [m^3 s^{-1}]; α_b is the angle of wave breaking, measured from shore-normal [rad]; $d_p = d_d + d_c$ is the profile depth [m]; with d_d

Table D.1: Parameters Used to Calculate Diffusion Coefficients κ_{sde} of Eq. (D.1).

Parameter	Symbol	Value	Unit	Source
Dune height,	d_d	3.0	m	Assumption
Closure depth,	d_c	$8.9 \cdot \langle H_s \rangle$	m	Houston (1995)
Wave break angle,	α_b	$\frac{\pi}{36}$	rad	Assumption
Wave-break slope,	m_b	0.01	-	Assumption
Sediment diameter,	D	0.125	mm	Model parameter
Peak period,	T_p	5.0	s	Model parameter
Sig. wave height,	H_s	0.8, 1.2, 1.6, and 2.0	m	Model parameters

the beach dune height [m]; and d_c the depth of closure [m] (Kamphuis, 2010).

Q_k [m^3 s^{-1}] may be calculated as:

$$Q_k = 2.028 \cdot 10^{-3} H_{sb}^2 T_p^{1.5} m_b^{0.75} D^{-0.25} \sin^{0.6}(2\alpha_b) \tag{D.3}$$

where H_{sb} is significant breaking wave height [m] (here it assumed that $H_{sb} = H_s$); T_p is peak wave period [s]; m_b is slope in wave breaking region [-]; and D is sediment diameter [m] (Kamphuis, 1991).

Values for the variables used in Eqs. (D.2) and (D.3) are given in Table D.1. Diffusion coefficients κ_{sde} are calculated for significant wave heights $H_s = 0.8$, 1.2, 1.6, and 2.0 m, in line with the significant wave heights modelled in this thesis.

Below are example calculations using $H_s = 1.2$ m. Alongshore sediment flux (Eq. (D.3)):

$$Q_k = 2.028 \cdot 10^{-3} \times 1.2^2 \times 5^{1.5} \times 0.01^{0.75} \times \left(1.25 \cdot 10^{-4}\right)^{-0.25} \times \sin^{0.6}\left(2\frac{\pi}{36}\right)$$
$$= 0.0034 \text{ m}^3\,\text{s}^{-1};$$

depth of closure (Houston, 1995):

$$d_c = 8.9 \times 1.2 = 10.68 \text{ m};$$

and finally diffusion coefficient (Eq. (D.2)):

$$\kappa_{sde} = \frac{0.0034}{\frac{\pi}{36}\,(10.68 + 3)} = 0.0029 \text{ m}^2\,\text{s}^{-1}.$$

This calculation, performed for $H_s =$ 0.8, 1.2, 1.6, and 2.0 m, gives diffusion coefficients κ_{sde} for the shoreline diffusion equation of 0.0017, 0.0029, 0.0040, and 0.0052 m^2 s^{-1} respectively.

Note that this analysis includes no provision for tidal variation.